Titre: Title:	Production of LiPO3 From LiH2PO4 in a Ball-Mill Rotary-Kiln (BaMRoK) Reactor
Auteur: Author:	Bahman Yari
Date:	2019
Type:	Mémoire ou thèse / Dissertation or Thesis
Référence: Citation:	Yari, B. (2019). Production of LiPO3 From LiH2PO4 in a Ball-Mill Rotary-Kiln (BaMRoK) Reactor [Thèse de doctorat, Polytechnique Montréal]. PolyPublie. https://publications.polymtl.ca/4081/

URL de PolyPublie: PolyPublie URL:	https://publications.polymtl.ca/4081/
Directeurs de recherche: Advisors:	Jamal Chaouki, & François Bertrand
Programme: Program:	Génie chimique

POLYTECHNIQUE MONTRÉAL

affiliée à l'Université de Montréal

Production of $LiPO_3$ from LiH_2PO_4 in a ball-mill rotary-kiln (BaMRoK) reactor

BAHMAN YARI

Département de génie chimique

Thèse présentée en vue de l'obtention du diplôme de *Philosophiæ Doctor*

Génie chimique

Octobre 2019

POLYTECHNIQUE MONTRÉAL

affiliée à l'Université de Montréal

Cette thèse intitulée :

Production of $LiPO_3$ from LiH_2PO_4 in a ball-mill rotary-kiln (BaMRoK) reactor

présentée par **Bahman YARI**

en vue de l'obtention du diplôme de *Philosophiæ Doctor*

a été dûment acceptée par le jury d'examen constitué de :

Robert LEGROS, président
Jamal CHAOUKI, membre et directeur de recherche
François BERTRAND, membre et codirecteur de recherche
Jason Robert TAVARES, membre
Marzouk BENALI, membre externe

DEDICATION

To the cause of the being, whatever you call it

To its most creative known being

To my reasons of being: My loving parents, my beloved Somayeh and my lovely Ryan and Liam

ACKNOWLEDGEMENTS

Now that I am approaching the end of my Ph.D. career, when I look back, I see many faces who have directly or indirectly supported me through this wonderful, mysterious journey. I would never reach the finish line of this challenging marathon, shouldn't be their collaborations, inspirations, motivations, and encouragements. I would like to take this opportunity to express my sincerest endless gratitude to all these fantastic people and organizations:

Jamal Chaouki; my supervisor: He is the mentor who in the first place inspired me by his way of thinking not to be confined by any cliché and then gave me all the support and freedom I needed to try, to invent and to experience. I am proud of being his 55th Ph.D. student to be graduated.

Fraçois Bertrand; my co-supervisor: His positive attitude motivated me from the first meeting. I benefited his valuable insights and am grateful for all his time and support despite his responsibilities in the department.

Pierre Sauriol. He never hesitated any help from insightful discussions to technical and academic contributions. I also owe him my French, although I still should work on my accent.

David Vidale, Christine Beaulieu. They trained me and helped in what I had never touched before. They always took time to sit with me in person or on Skype to troubleshoot my DEM modelling.

Sylvain Simard Fleury, Robert Delisle, Yanik Landry-Ducharme and Maxime Beaudoin; the ingenious technicians of the department of chemical engineering: These people are simply marvellous. They do not recognize "impossible." They did anything for me from drilling the hardest AISI 5200 stainless steel balls to designing and building the vague ideas of setup in my mind. I was always astonished by their know-how and brilliant ideas.

Hélène Chatillon, Valérie Baudart, Mariia Kopach, Brigitte Langevin, Carmen Elena Membreno Aguilar, Évelyne Rousseau, Kalonji Mbelu, Brigitte Gagnon, Mehdi Bentounes, Sébastien Chénard, Daniel Pilon, Jean Huard, Anic Desforges, Carole Savoie, Jérôme Leroy, Manon Leduc, Gino Robin and Martine Lamarche and all other present and previous technical and administrative staff of the department of Chemical engineering and Polytechnique Montreal: I never forget their friendly attitude and their energy giving smiles, whenever I passed their offices.

PEARL group, my wonderful colleagues in "Process Engineering Advanced Research Laboratory." I had all those unforgettable memories with these professional scientists. Many brilliant ideas came to my mind after fruitful discussions with them. Particularly I should appreciate Majid Rasouli, Mohammad Latifi, Jaber Shabanian and Rouzbeh Jafari who always cared and showed interest in my work.

URPEI group, my amazing colleagues in "Unité de recherche en procédés d' écoulements industriels / Research Center in Industrial Flow Processes." I always learned from them and had a great time with them in the outings.

Johnson Matthey Inc. and NSERC. This research was financially supported by these two organizations.

My friends. I would like to appreciate all my friends in Polytechnique Montreal and elsewhere for all their moral and physical support and the pleasurable moments that we had together during my Ph.D.

My family. I would also like to express my most profound gratitude to all my family members that backed me in ups and downs of my life. For sure, my parents are the champions of my life. They taught me to believe in hard work and follow the truth. I hope my mother and the soul of my father are proud to see me at this point.

Finally, I would like to offer my most unique and deepest gratefulness to someone whom I owe this thesis from the beginning to the end, someone who encouraged me to take the first step, someone who patiently carried the burden of life for me to finish this mission. She is my beloved wife Somayeh, to whom I dedicate this thesis.

Bahman Yari

Polytechnique Montreal,

Summer 2019

RÉSUMÉ

La demande mondiale pour les batteries lithium-ion (LIB) continue de croître à un rythme exponentiel qui ne semble pas s'estomper. La concurrence des géants de la production de LIBs dans les trois principaux secteurs de l'industrie, notamment les appareils électroniques, les véhicules électriques, et le stockage sur réseau électrique pour équilibrer les énergies renouvelables, a été le moteur de cette augmentation fulgurante au cours des deux dernières décennies. De nombreux facteurs affectent cette concurrence, notamment la densité d'énergie et de puissance, l'énergie spécifique, la capacité, la tension, le cycle de vie, le coût et la sécurité, et différents composants de la batterie tels que la cathode, l'anode et l'électrolyte déterminent ces facteurs.

Le phosphate de fer lithié (également connu sous le nom de ferrophosphate de lithium, $LiFePO_4$ ou LFP) est l'un des matériaux cathodiques pour LIB les plus sûrs et potentiellement l'un des moins couteux à fabriquer. En raison de la stabilité intrinsèque de la liaison oxygène-phosphore dans le phosphate, le LFP est le matériau de cathode le plus résistant dans les LIB contre l'emballement thermique à des températures élevées, en particulier dans le cas des batteries de grande capacité. En outre, il s'agit d'un des matériaux cathodiques économiques potentiels pour les LIBs en raison de la présence de fer et phosphore dans sa composition par rapport à ses homologues qui eux contiennent : cobalt, manganèse, aluminium ou nickel.

La production en phase fondue de LFP présente les avantages d'une cinétique plus rapide, qui permet d'opter pour des réactifs de plus grosses taille généralement moins couteux, d'un coût en capital moindre et de la possibilité d'utiliser des réactifs de commodité, par rapport aux deux autres modes de production de LFP (e.g., phase solide ou aqueuse). Cependant, la plupart des réactifs couramment utilisés comme sources de lithium, de fer et de phosphate réagissent vigoureusement à la température de fusion du LFP et libèrent un grand volume de sous-produits gazeux, ce qui pourrait présenter problème pour la production à grande échelle, en particulier en mode continu.

Le métaphosphate de lithium ($LiPO_3$ ou LPO) est un réactif idéal pour la synthèse par fusion, car il peut être ajouté en toute sécurité à la phase fondue sans engendrer de produits gazeux. Il a également une application en tant que composant d'électrolyte solide pour les LIBs. Cependant, actuellement l'offre et la demande très faible pour le LPO fait en sorte que son prix n'est pas aussi

compétitif qu'il ne pourrait l'être sur la base de ses constituants et ainsi, le développement d'une synthèse de LFP basée sur le LPO doit inclure la production de celui-ci afin de bénéficier de prix favorables.

Le LPO peut être produit par déshydratation thermique du dihydrogénophosphate de lithium (LiH_2PO_4 ou LHP) disponible à l'échelle industrielle. Bien que cette réaction ait une cinétique rapide menant à une conversion complète à 400 ° C, le produit est un solide dur qui adhère à la surface du récipient de réaction, ce qui le rend difficile sa manutention. Pour produire, détacher et broyer le produit en une seule étape de traitement, nous avons eu l'idée originale de développer un nouveau réacteur pour la déshydratation simultanée de LHP et le broyage de la LPO produite.

Dans la présente thèse, la production de LPO à partir de LHP dans la nouvelle configuration de réacteur (four rotatif à billes, FRAB) a été étudiée. La cinétique de la réaction, l'hydrodynamique du matériau dans le tambour rotatif ainsi que le transfert de chaleur et la réaction dans le réacteur semi-industriel ont été étudiés en tant que trois objectifs de l'étude.

Dans le premier objectif, nous avons étudié la décomposition thermique de LHP en LPO. Il s'est avéré que la réaction pouvait généralement être complète à moins de 400 °C ce qui est devenu la limite supérieure de l'étude. La décomposition a été analysée par des expériences thermogravimétriques différentielles (DTG) isothermes et à vitesse constante. Les profils d'énergie d'activation ont été estimés par une approche sans modèle isoconversion et un ajustement du modèle cinétique. Il a été déterminé que $Li_5H_4P_5O_{17}$ (équivalent à $Li_{2.5}H_2P_{2.5}O_{8.5}$, L2.5) était l'intermédiaire de réaction le plus stable et pouvait être isolé à des températures comprises entre 200 et 240 ° C. La réaction globale de décomposition a pu être décrite par un mécanisme réactionnel comportant 4 étapes que l'on a pu décrire au moyen de 6 réactions dans lesquelles la LHP est progressivement polymérisée par des réactions de condensation conduisant successivement à L2.5, $Li_3H_2P_3O_{10}$ (L3), $Li_4H_2P_4O_{13}$ (L4) et LPO. La première étape réactionnelle (LHP → L2.5) a été modélisée par 3 réactions série / parallèle décrivant la réaction de surface solide, la réaction de surface visqueuse / liquide et la réaction en masse. La limitation de la température de réaction à 400 ° C donne un produit solide qui peut être avantageux si la LPO doit être préparée à l'avance et dosée pour la synthèse de LFP. L'étude a permis de mettre en évidence l'influence de la taille de départ des particules de LHP, du temps passé dans la plage de température comprise entre 180 et

210 °C (frittage et fusion du LHP) dans la cinétique observée, signifiant l'importance du transfert de matière et de chaleur dans l'évolution de la réaction.

Le mélange et la séparation de la charge dans un broyeur à billes peuvent jouer un rôle crucial dans l'efficacité du processus de broyage. Cela devient plus important, en présence de réaction et de transfert de chaleur et de masse, comme dans le cas d'un réacteur à broyeur à billes. Dans le deuxième objectif, la méthode des éléments discrets (DEM) et la méthode expérimentale d'échantillonnage sur lit solidifié ont été utilisées pour étudier l'effet de différents rapports de taille sur le mélange et la ségrégation de particules sphériques de taille binaire dans un tambour rotatif. Dans la partie expérimentale, nous avons utilisé la « fixation sur lit d'agar» avec une nouvelle technique d'échantillonnage que nous appelons ici «échantillonnage matriciel». Les billes de verre sphériques de 10 mm représentaient le milieu de broyage et les billes de verre sphériques plus petites (de taille allant de 1 mm à 6 mm) représentaient le mélange réactionnel. Les résultats de DEM et des essais ont menés à des résultats semblables confirmant la validité du modèle DEM. Pour une taille constante de 10 mm pour le composant le plus grand, lorsque le rapport de taille entre les deux composants était supérieur à une valeur de transition (0.26), le composant le plus petit avait tendance à s'accumuler dans la région centrale située près de la couche active, alors que dans le cas contraire, ils se sont accumulés près de la paroi du tambour dans la couche passive. La distribution la plus uniforme des petites particules a été atteinte autour du ratio de transition. Ces rapports de taille ont été analysés géométriquement (Annexe A) et justifiés par la sphère inscrite théorique dans un arrangement hexagonal (hcp). De ces observations, on en conclu que dans le contexte d'un FRAB chauffé en paroi, un chauffage du LHP plus intense devrait être obtenu en employant des billes suffisamment grosses pour que les particules de LHP se retrouvent préférentiellement aux parois.

Dans le troisième objectif, la déshydratation de LHP à une température inférieure à celle du procédé de trempe classique à l'état fondu a été réalisée dans un four rotatif à broyeur à billes. L'effet des billes sur le transfert de chaleur et de masse dans un four rotatif à calandre électrique a été étudié en mesurant les températures de la calandre, des billes et du gaz porteur ainsi que la teneur en eau du gaz porteur (humidité relative + température). La comparaison de ces températures et de l'humidité en tant qu'indication du taux de réaction a montré que, sur la base du modèle cinétique obtenu à partir du premier objectif, le matériau est à la température de la paroi du réacteur plutôt

qu'à la température des billes. Cela concordait également avec les conclusions du deuxième objectif, selon lesquelles les particules devraient être séparées sur le mur en raison de leur rapport de taille inférieur à 0.26. L'effet du taux de rotation et du débit du gaz porteur, sur la température du gaz porteur au point de sortie a également été étudié et présenté à l'annexe B.

ABSTRACT

The growth in the global demand for the lithium-ion batteries (LIBs) is still on its exponential track and does not seem to settle soon. The competition of the giants of the lithium-ion battery production in the three main sectors of industry including electric vehicles, electric grid storage for balancing renewable energy, and electronic appliances has been the driving force for this overwhelming increase during last 2 decades. Many different factors affect this competition including but not limited to energy and power density, specific energy, capacity, voltage, life cycle, cost and safety. Different components of the battery like cathode, anode, and electrolyte determine these factors.

Lithium iron phosphate (also known as lithium ferrophosphate, $LiFePO_4$, and LFP) is one of the safest and economical cathode materials to produce lithium-ion batteries. Due to the stability of the oxygen-phosphorus bond in phosphate, LFP is the most resistant cathode material in large scale LIBs against thermal runout in elevated temperatures, especially in the case of large-capacity batteries. Furthermore, it is one of the potential economic cathode materials for LIBs because of the presence of iron in its composition as compared to its counterparts; cobalt, manganese, aluminum and nickel.

Molten phase production (melt casting) of LFP has the advantages of faster kinetics, lower capital cost and the possibility of using lower-cost commodity-grade reactants over the two other categories of LFP production; solution-based and solid-state. However, most common reactants used as the sources of lithium, iron, and phosphate react vigorously at melt casting temperature and release a large volume of gaseous by-products which can make a problem for the large-scale production especially in continuous mode.

Lithium metaphosphate ($LiPO_3$ or LPO) is an ideal reactant for the melt casting, as it can safely be added to the molten phase without the vigorous gas release problem. It also has applied as a component of solid electrolyte for LIBs. However, currently, the very low supply and demand for the LPO makes its price not as competitive as it could be on the basis of its constituents and so the development of a synthesis of LFP based on the LPO must include the production of it in order to benefit from favourable prices.

LPO can be produced by thermal dehydration of lithium dihydrogenphosphate (LiH_2PO_4 or LHP) which is commercially available in industrial scale. Although this reaction has fast kinetics leading

to a complete conversion at 400 ℃, the product is a hard solid that sticks to the surface of the reaction vessel, making it difficult to collect. To produce, detach and grind the product in a single processing step, we came up with the novel idea of developing a new reactor for simultaneous dehydration of LHP and grinding the produced LPO.

In this dissertation, the production of LPO from LHP in the novel reactor setup (ball-mill rotary-kiln reactor or BaMRoK reactor) was studied. Kinetics of the reaction, hydrodynamics of the material in the rotating drum and the heat transfer and reaction in the semi industrial-scale reactor were studied as three objectives of the study.

In the first objective, we investigated the thermal decomposition of LHP to LPO. It turned out that the reaction could usually be completed at less than 400 ° C, which became the upper limit of the study. The decomposition was analyzed by isothermal and constant rate differential thermogravimetric (DTG) experiments. Activation energy profiles were estimated by an isoconversional model-free approach and kinetic model fitting. $Li_5H_4P_5O_{17}$ (equivalent to $Li_{2.5}H_2P_{2.5}O_{8.5}$, L2.5) was determined to be the most stable reaction intermediate and was isolated at temperatures between 200 and 240 °C. The overall decomposition reaction could be described by a reaction mechanism comprising 4 steps that could be explained by means of 6 reactions, where the LHP is progressively polymerized by condensation reactions leading successively to L2.5, $Li_3H_2P_3O_{10}$ (L3), $Li_4H_2P_4O_{13}$ (L4), and LPO. The first reaction step (LHP → L2.5) was fitted with 3 reactions series/parallel describing the solid surface reaction, the viscous/liquid surface reaction, and the bulk reaction. Limiting the reaction temperature to 400 °C results in a solid product that can be advantageous if LPO is to be prepared in advance and dosed for LFP synthesis. The study revealed the influence of the starting size of the LHP particles, the time spent in the temperature range between 180 and 210 ° C (Sintering and LHP fusion) in the observed kinetics, showing the importance of the mass and heat transfer in the evolution of the reaction.

Mixing and segregation of media in a ball mill can play a critical role in the efficiency of the milling process. This becomes more important, in the presence of reaction and heat and mass transfer, as in the case of a BaMRoK reactor. In the second objective, discrete element method (DEM) and experimental solidified bed sampling method were used to study the effect of different size ratios in mixing and segregation of binary sized spherical particles in a rotating drum. In the experimental

part, we used “agar bed fixing” together with a new sampling technique we call it here “matrix sampling.” 10 mm spherical glass beads represented the grinding media, and smaller spherical glass beads (ranging in size from 1 mm to 9 mm) represented the reaction mixture. The results of DEM and the experiments led to similar results confirming the validity of the DEM model. For a constant size of 10 mm for the bigger component, when the size ratio between the two components was bigger than a transition amount (0.26), smaller component tended to accumulate in the core region near the active layer, whereas at the opposite case, they accumulated near the drum wall in the passive layer. At ratios around the transition ratio, the most uniform distribution of smaller component was attained. These size ratios were geometrically analyzed and justified by the theoretical inscribed sphere in a hexagonal-close-packing (hcp) arrangement. From these observations, it is concluded that in the context of a wall-heated BaMRoK, more intense LHP heating should be obtained by using beads large enough for the LHP particles to preferentially place on the wall.

In the third objective, the dehydration of LHP in a reduced temperature than the common melt quenching method was carried out in the ball mill-rotary kiln. The effect of the balls on the heat transfer in an electrical shell heated rotary kiln was studied by measuring the temperatures of the shell, balls and the carrying gas along with the water content of the carrier gas (relative humidity + temperature). Comparison of these temperatures and the RH as an indication of the reaction rate showed that based on the kinetic model obtained from the first objective the material is at the temperature of the reactor wall rather than the temperature of the surface of the balls. This was also in accordance with the findings of the second objective that the particles should be segregated on the wall because of their size ratio, which is less than 0.26. The effect of the rotation rate and the flow of the carrying gas, on the temperature of the carrying gas at the exit point, has also been investigated and presented in Appendix B.

TABLE OF CONTENTS

DEDICATION iii

ACKNOWLEDGEMENTS iv

RÉSUMÉ vi

ABSTRACT x

TABLE OF CONTENTS xiii

LIST OF TABLES xvii

LIST OF FIGURES xviii

LIST OF SYMBOLS AND ABBREVIATIONS xxii

LIST OF APPENDICES xxvi

CHAPTER 1 INTRODUCTION 1

CHAPTER 2 LITERATURE REVIEW 6

2.1 Production of lithium metaphosphate ($LiPO_3$) 6

2.1.1 Neutralization of metaphosphoric acid 6

2.1.2 Ion replacement 7

2.1.3 Syntheses based on P_2O_5 7

2.1.4 Dehydration of LiH_2PO_4 8

2.1.5 Other miscellaneous methods for the synthesis of $LiPO_3$ 9

2.2 Rotary kiln 11

2.2.1 Horizontal rotary kilns versus other contactors 12

2.2.2 Different types of rotary kilns 13

2.2.3 Indirect flame and electric rotary kilns 15

2.2.4 Effect of lifters on the efficiency of the rotary kiln 16

2.2.5 Transport phenomena in the rotary kiln bed 17

2.3 Ball mill 20
2.3.1 Effect of different parameters on the efficiency of ball milling 21
2.4 Mixing and segregation of solid particles and grinding media in rotary-kiln ball-mill 24
2.4.1 Solid mixing mechanisms in rotary drums 24
2.4.2 Solid particles segregation in a rotary drum 25
2.4.3 Methods for characterization of the mixing and segregation in a rotary drum 27
2.4.4 Discrete element method 30
CHAPTER 3 COHERENCE OF THE ARTICLES 34
CHAPTER 4 ARTICLE 1: KINETICS OF THE DEHYDRATION OF LITHIUM DIHYDROGENPHOSPHATE 36
4.1 Abstract 36
4.2 Introduction 37
4.2.1 Gas release from potential chemistries to produce LFP 37
4.2.2 Decomposition of alkali metal dihydrogenphosphates 39
4.2.3 Present study 40
4.3 Materials and methods 40
4.4 Results and discussion 42
4.4.1 Part 1: Identifying the main reaction steps 42
4.4.2 Part 2: Determination of kinetic parameters 55
4.5 Conclusion 70
4.6 References 73
CHAPTER 5 ARTICLE 2: SIZE SEGREGATION IN A BALL-MILL ROTARY-KILN REACTOR 77
5.1 Abstract 77

5.2 Introduction 78
5.3 Materials and methods 90
5.3.1 Solidified bed sampling 90
5.3.2 DEM simulation 94
5.4 Results and discussion 97
5.4.1 Solidified bed sampling method results 97
5.4.2 DEM results 105
5.5 Conclusion 108
5.6 References 110
CHAPTER 6 ARTICLE 3: DEHYDRATION OF LITHIUM DIHYDROGENPHOSPHATE IN A BALL-MILL ROTARY-KILN REACTOR 117
6.1 Abstract 117
6.2 Introduction 118
6.2.1 Dehydration mechanism 119
6.2.2 High-temperature ball milling 122
6.3 Materials and methods 126
6.4 Results and discussion 129
6.4.1 Temperature profile at steady state 129
6.4.2 Direct measuring and modelling of the temperature profile at the unsteady state 131
6.4.3 The reaction rate of the dehydration of LiH_2PO_4 in the BaMRoK 135
6.4.4 Recovery and characterization of the product 138
6.5 Conclusion 141
6.6 References 143
CHAPTER 7 GENERAL DISCUSSION 146

CHAPTER 8 CONCLUSION AND RECOMMENDATIONS 149

REFERENCES 151

APPENDICES 170

LIST OF TABLES

Table 2.1 Some examples of performed synthesis of LiPO3 (Angaiah E. A., 2003) 10

Table 2.2 Typical specifications of direct and indirect contactors (A. A. Boateng, 2011).....13

Table 2.3 Improvements after lifter installation in two lightweight aggregate units (A. A. Boateng, 2011).....16

Table 2.4 Froud numbers corresponding to each of the transverse motion regimes (Henein, 1980) 20

Table 4.1 Description of deceleratory reaction models considered 63

Table 4.2 Summary of the optimum parameters as fitted 64

Table 5.1 Comparison of the methods of the investigation of the mixing and segregation in granular mixers (cont'd) 81

Table 5.2. Conditions of the experiments performed in this study 91

Table 5.3 Physical and mechanical particle properties used for DEM simulations (cont'd).....95

Table 5.4 Characteristics of the DEM simulations (cont'd).....97

Table 6.1 summary of the optimum parameters as fitted (cont'd).....120

Table 6.2 Applications of ball milling in chemical processes and their advantages over corresponding traditional processes (cont'd) 123

Table 6.3 Results of the direct measurements of the temperatures of the internal surface of the cylinder and the surface of the stainless-steel balls based on procedures 1 and 2 131

Table 6.4 Optimized modelling parameters for heat transfer in the BaMRoK (cont'd) 133

Table 6.5 Convective heat transfer coefficient between the wall and the solids in the rotary kiln for different applications.....134

LIST OF FIGURES

Figure 1.1 Annual LIBs sold (2000-2018) or estimated for sale (2019-2025) for each application on the global market (tonnes).....2

Figure 2.1 Schematic diagram of wet rotary kiln (http://www.understanding-cement.com/kiln.html) 14

Figure 2.2. Schematic diagram of a modern dry short cement rotary kiln(http://www.understanding-cement.com/kiln.html).....15

Figure 2.3. Schematic diagram of certain type lifter (L lifter) in the rotary kiln (Dennis R. Van Puyvelde).....17

Figure 2.4. Different heat transfer phenomena in a rotary kiln bed: 1.particle internal conduction, 2. conduction between two particles, 3. radiation between two particles, 4. convection in the gas between particles.....18

Figure 2.5 Different transverse motion regimes at different rotation rates (A. A. Boateng, 2011)19

Figure 2.6 Commercial grinding media in ball milling, Cylpebs versus balls.....22

Figure 2.7 Simple schematic of spring and dashpot modelling the elastic and dissipation forces (www.wikiversity.com, 29/2/2016) 31

Figure 4.1 TGA and DTG of LiH2PO4 with constant heating rates, locations where mass loss coincides with specific intermediates are identified for reference. (a): 25-75 µm particle size, 1℃/min heating rate (b): 25-75 µm particle size, 1-30 ℃/min different heating.....44

Figure 4.2 TGA and DTG of LiH2PO4 with constant heating rates, locations where mass loss coincides with specific intermediates are identified for reference. (c): 250-350 µm particle size, 1℃/min heating rate (d): 250-350 µm particle size, 1-30 ℃/min different heating rates. 45

Figure 4.3 Combined constant heating rate/isothermal TGA curves of LHP and intermediate #1 at different final temperatures. (a): LHP (180-280 °C), (b): LHP (280-400 °C), 25-75µm and ramp rate 10 °C/min 48

Figure 4.4 Combined constant heating rate/isothermal TGA curves of LHP and intermediate #1 at different final temperatures. (c): 1st Intermediate (320-400 °C), (d): effect of starting mass for 220°C isotherm (5 mg vs 15 mg). In (c) re-ground after synthesis 25-75 μm and ramp 20 °C/min, in (d) 25-75μm and ramp rate 10 °C/min; 49

Figure 4.5 DSC and DTG of LHP (250-350 μm particle size) along with DSC of 1st and 2nd intermediates (220 and 350 °C), at 1 °C/min constant heating rate 52

Figure 4.6 X-ray diffractograms of LHP, 1st intermediate (220 °C, L2.5-rich), 2nd intermediate (350 °C, LPO-rich with oligomers), and LPO (crystalline and amorphous) 53

Figure 4.7 Raman spectrogram of LHP, 1st intermediate (220 °C, L2.5-rich), 2nd intermediate (350 °C, LPO-rich with oligomers), and LPO (crystalline). 54

Figure 4.8 Activation energy estimation from model-free iso-conversional integral methods for LHP 25-75 μm as starting material. (a) For ramp rates < 10 °C/min; (b) ramp rates ≥ 5 °C/min 58

Figure 4.9 Comparison between the experimental and fitted model prediction starting with LHP 25-75 μm with ramp rates between 1 and 30 °C/min. (a) conversion extent vs. temperature (Solid lines: model prediction; dotted lines: experimental data); (b) difference between the model predicted and experimental conversion extent. Only the data for ramp rates ≥ 5 °C/min was used for model fitting.....67

Figure 4.10 Model performance under isothermal conditions. (a) 25-75 μm LHP at 180-280 °C isotherms, (b) 25-75 μm LHP at 280-400 °C; (c) 25-75 μm reground 1st intermediate (220°C) at 320-400 °C. Solid lines: model prediction; dotted lines: experimental data.....69

Figure 5.1 Isometric plan of the rotating drum (with removable lifters) used for the experiments 91

Figure 5.2 Inverse turning of the bed to make the bed surface parallel to the horizon.....92

Figure 5.3 Special tool designed and fabricated for the sampling of the solidified bed of the rotating drum in this study.....94

Figure 5.4 Final RSD of binary mixtures versus size ratio after 110 revolutions (continuous line) compared to RSD of corresponding random mixtures (dashed line), (a) Experiments A1 to A6, (b) Experiments B1 to B3 100

Figure 5.5 Planar sections of adjacent spheres in binary spherical mixtures. (a) non-compact $ra \cong 0.41R$, (b) compact configurations $rb \cong 0.15R$ (ra and rb are the radii of inscribed spheres and R is the radius of circumscribed spheres) 100

Figure 5.6 Final segregation intensity of binary mixtures versus size ratio after 110 revolutions 102

Figure 5.7 Final occupancy plots of binary mixtures in experiments A1 to A6 (Table 5.2) after 110 revolutions. Green is the lowest and red is the highest x (concentration of smaller beads) 103

Figure 5.8 The temporal evolution of the RSD of the binary spherical mixtures from completely segregated situation (top-bottom), simulated by DEM, (a) size ratios 0.5, 0.6, 0.7, 0.8, 0.9 and (b) size ratios 0.1, 0.2, 0.3, 0.4 107

Figure 5.9 Comparison of the RSD data obtained from DEM simulations and solidified-bed sampling method and the model obtained therefrom for different size ratios 108

Figure 5.10 DEM simulation of final occupancy plots of binary mixtures with different size ratios: (a) 6 mm/10 mm, (b) 5 mm/10 mm, (c) 4 mm/10 mm, (d) 3 mm/10 mm, (e) 2 mm/10 mm, (f) 1 mm/10 mm, after 110 revolutions 109

Figure 6.1 Pictorial and graphic views of the BaMRoK used in the experiments. (a) Side view, (b) Internal view of the cylindrical kiln, showing stainless steel balls with 2.5 cm diameter and the white powder product (dehydrated LHP), and (c) Graphic axial cross section 127

Figure 6.2 Schematic diagram of the experimental setup 128

Figure 6.3 (a) Tin and zinc filings and (b) drilled ball used for temperature verification with procedure 2 130

Figure 6.4 Set and measured temperature profiles of external and internal surfaces of the rotary-kiln wall and surface of the balls, and the optimized COMSOL models 133

Figure 6.5 Comparison of the measured reaction rate with the predicted reaction rates based on the kinetic model with the modelled temperature profiles (T_{wall} and T_{balls}) 136

Figure 6.6 Differential thermogravimetric analysis (DTG) of LHP at 5 °C/min with two ranges of particle size (Yari et al., 2019) 137

Figure 6.7 Comparison of the measured conversion versus time with the predicted conversions based on measured and modelled temperature profiles 138

Figure 6.8 Particle size distribution (PSD) analysis results for the LPO produced in the BaMRoK reactor after 1 h grinding with 13 rpm at 500 °C 139

Figure 6.9 Measured and calculated X-ray diffractograms of the product of the dehydration of LHP (LPO) in the BaMRoK 140

Figure 10 (a) Raman spectra of LHP and its dehydration product (LPO) (b) Raman spectrum of LPO at 293 K from (Kartini et al., 2010) 142

LIST OF SYMBOLS AND ABBREVIATIONS

A Reaction frequency factor, pre-exponential term in Arrhenius formulation (min^{-1})

BaMRoK Ball-mill rotary-kiln

CCD Charge-coupled device

d/D size ratio in bidisperse granular mixture

DEM Discrete elements method

DSC Differential scanning calorimetry

DTG Derivative thermogravimetry

Ea activation energy (J/mol)

Err model prediction error (-)

f(α) reaction model function (-)

g(α) integral form of the reaction model function (-)

h_{eff} effective bulk convection heat transfer coefficient (W/m^2K)

ICTAC International Confederation for Thermal Analysis and Calorimetry

I_s segregation intensity (-)

$k_{n,ij}$ normal stiffness coefficient (-)

$k_{t,ij}$ tangential stiffness coefficient (-)

LEI Low secondary electron image

LFP Lithium iron phosphate, $LiFePO_4$

LHP Lithium dihydrogen phosphate, LiH_2PO_4

LPO Lithium metaphosphate, $LiPO_3$

L2 Lithium pyrophosphate, $Li_2H_2P_2O_7$

L2.5 $Li_{2.5}H_2P_{2.5}O_{8.5}$ (equivalent to ½ $Li_5H_4P_5O_{17}$)

L3 $Li_3H_2P_3O_{10}$

L4 $Li_4H_2P_4O_{13}$

M generic alkali metal cation (and ammonia) defined for some chemical formulations (M can be: Li, Na, K, Rb, Cs, and NH_4)

MAP monoammonium phosphate, $NH_4H_2PO_4$

n moles of various species (mol)

n_k number of ramp rate trials considered in the analysis

P_{O_2} partial pressure of Oxygen

P2/m Primitive monoclinic Bravais-lattice space group

r reaction rate (mol/min)

R gas constant (J/mol·K)

RSD Relative standard deviation (-)

RSD_r Relative standard deviation of the random mixture (-)

SEM Scanning electron microscopy

SR Size ratio

t time (min)

T temperature (°C or K as indicated)

TGA Thermogravimetric analysis

x_{surf} fraction of the starting LHP that is considered to belong to the surface, the balance belonging to the bulk (-)

T_kiln set point temperature of the kiln

Tb_exp experimentally measured temperature of the balls (°C)

Tw_exp experimentally measured temperature of the internal surface of the BaMRoK wall (°C)

Tb_mod modelled temperature of the balls (°C)

Tw_mod modelled temperature of the internal surface of the wall (°C)

w weighing function that varies between 0 and 1 and activates a specific reaction step based on the completion status of the previous reaction, this ensures that the reactions are sequential without having to introduce reversibility

XRD X-ray diffraction

y number of PO3 repeat units in the oligomer (in article 1)

yH_2O H_2O molar fraction from measured RH (in article 3)

Z number of chemical formula units per unit cell

Greek letters

α global conversion extent for the reaction LHP to LPO based on the mass loss (-)

β ramp rate (°C/min)

$\gamma_{n,ij}$ normal damping coefficient (-)

$\gamma_{t,ij}$ tangential damping coefficient (-)

σ Variance (-)

σ_r The variance of the random mixture (-)

$\delta_{n,ij}$ normal overlap length (m)

$\delta_{t,ij}$ tangential overlap length (m)

$\dot{\delta}_{n,ij}$ the time derivative of the normal overlap length (m/s)

$\dot{\delta}_{t,ij}$ time derivative of the tangential overlap length (m/s)

ν molar reaction coefficients of species (reactant < 0; product > 0; non involved = 0)

ε emissivity (-)

indices

0	initial
exp	experimental
i	reaction steps
j	chemical species (LHP, L2.5, L3, L4, LPO, H_2O)
k	ramp rates
mod	model
new	new condition (as opposed to reference condition)
ref	reference condition
surf	surface

LIST OF APPENDICES

Appendix A The effect of the rotation rate and the flow of the carrier gas, on the temperature of the carrier gas at the exit point of the BaMRoK 170

CHAPTER 1 INTRODUCTION

Lithium-ion batteries (LIBs) exceptionally have the double advantage of high energy and power density because of the unique chemical properties of lithium, i.e., the lowest ionic radius (76 pm) and lowest atomic mass (6.941 u) amongst the metallic elements (Lide, 1995; Tarascon & Armand, 2001). Introduction of the first rechargeable LIB in 1980 triggered a huge revolution in portable electronic devices, transportation industry and electrical grid energy storage (K. Mizushima, P. C. Jones, P. J. Wiseman, & J. B. Goodenough, 1980). If the electric vehicles (EVs) dominate traditional fossil fuel vehicles by the development of the LIBs, the greenhouse emission problem and its consequent global warming will significantly be reduced (Pacala & Socolow, 2004).

The global LIB market has skyrocketed from 3 billion dollars in 2000 to over 20 billion dollars in 2018 (Pillot, 2012; Workman, 2019). This is partly because of the introduction of plug-in hybrid and electric vehicles like Toyota Prius, Nissan Leaf, Tesla Model S, and Chevrolet Volt that used such batteries (Pillot, 2012). Only since 2010, the annual installed capacity of LIBs has augmented by 500 percent globally as reported by Avicenne Energy. According to Bloomberg New Energy Finance (BNEF), the total number of EVs in the world passed 4 million in 2018, and many market studies have estimated that 20 percent of the global vehicles will be electric by 2025 (Melin & Ledung, 2019). LIBs are more and more finding new applications aside from EVs and electronic gadgets. These applications include electric buses, electric bikes and scooters, power tools, electric lift trucks, electric lawnmowers, backup power for telecom base stations and data centers, storage systems for renewable energy power stations and so on (Figure 1.1)(Melin & Ledung, 2019).

On the other hand, the demand for safer LIBs with higher specific energy, longer life-span, and the lower price has increased. Since the development of the first rechargeable lithium-ion battery with lithium cobalt oxide cathode by Mizushima et al. (K. Mizushima, P. Jones, P. Wiseman, & J. Goodenough, 1980) and its first commercialization by Sony Inc. in 1991, different cathode materials like $LiCoO_2$ (LCO), $Li(Ni_{0,33}Mn_{0,33}Co_{0,33})O_2$ (NMC), $LiMn_2O_4$ (LMO), $LiFePO_4$ (LFP) and $Li(Ni_{0,8}Co_{0,15}Al_{0,05})O_2$ (NCA), have been used as cathode of these LIBs.

Lithium iron phosphate ($LiFePO_4$; LFP), in comparison to other materials has the advantages of better thermal and chemical stability, acceptable life cycle, lower toxicity, friendliness to the environment, acceptable practical specific capacity (160 mAh/g compared to 140 mAh/g for

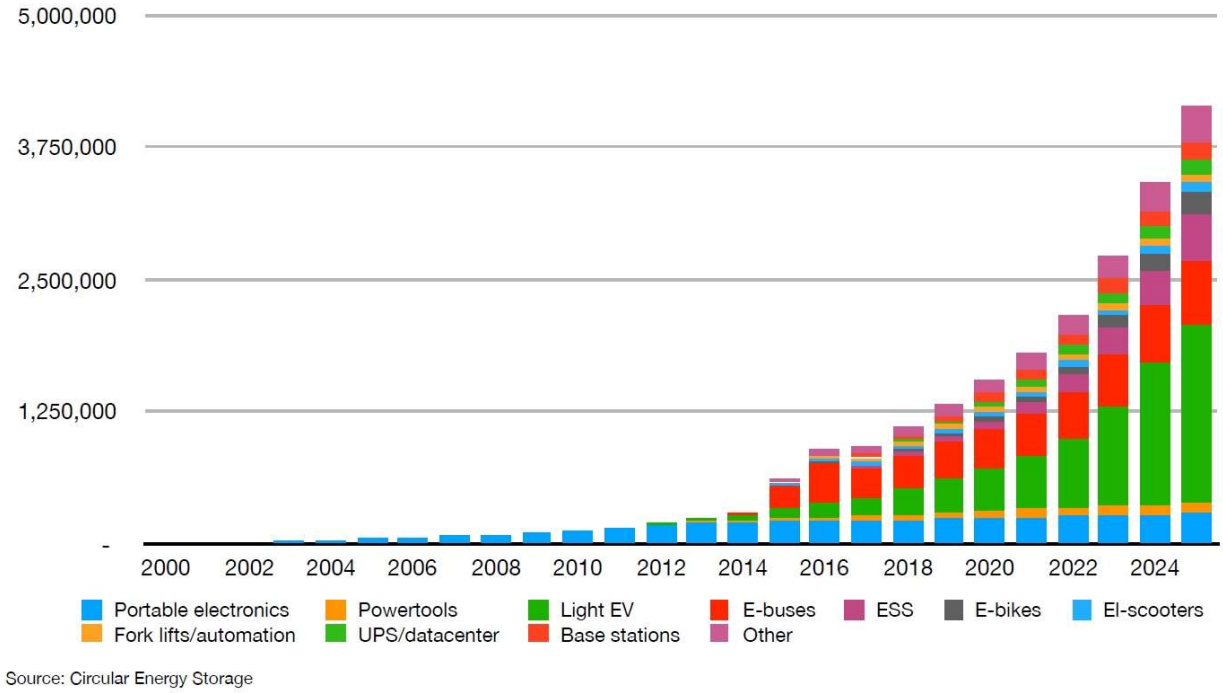

Figure 1.1 Annual LIBs sold (2000-2018) or estimated for sale (2019-2025) for each application on the global market (tonnes)

lithium cobalt oxide), and its potential for cost reduction which makes it a good choice for larger applications, notably automotive industry and grid applications (e.g., renewable energy power systems). This cathode material is most widely used in the LIBs for the automotive industry in Asia. Many famous rechargeable battery manufacturers like BYD, CATL, and Lishen use LFP as the cathode material for the batteries manufactured for electric vehicles (EVs) and plug-in EVs (PHEVs) like BYD E6 and Geely LC (Pelegov & Pontes, 2018). Studies show that LFP has a much smaller (<0.1%) self-heating rate and consequently more resistance to thermal runaway compared to other common oxide type cathode material (Kvasha et al., 2018; Xuan Liu et al., 2016) which results in safer LIBs.

There are several methods for preparation of lithium iron phosphate in the literature, namely: solid-state methods including solid-state synthesis, mechano-chemical activation (high energy ball milling), carbothermal reduction and microwave heating, solution-based methods including

hydrothermal method, spray pyrolysis, sol-gel synthesis, co-precipitation, micro-emulsion drying (M. Gauthier et al., 2010; MacNeil et al., 2010; Satyavani, Kumar, & Rao, 2015; Swietoslawski, 2014). Melt synthesis of LFP was first patented by researchers in Université de Montréal (L. Gauthier, Gauthier, Lavoie, Michot, & Ravet, 2009a, 2011) and has the advantage of lower capital cost in industrial production, the possibility of using commodity-grade primary material with different particle sizes and higher purity of the product. Melt synthesis consists of the near-stoichiometric reaction of the reactants (sources of lithium, iron, and phosphate) to form LFP. One of the initially considered reactions to produce LFP by melt casting is:

$$NH_4H_2PO_4 + Li_2CO_3 + Fe_2O_3 + \text{reducing agent} \Rightarrow LiFePO_4 + \text{gases} \quad (1.1)$$

With graphite powder as a reducing agent, this reaction typically releases over 0.5 standard cubic meter of gases (NH_3, H_2O, CO, CO_2) per kg of synthesized LFP. Most of the gas may violently release, as equilibrium is rapidly displaced by rapid exposure to elevated temperature and cause material waste and safety issues, especially when the reactants are being added to the melt in continuous operation. Furthermore, the toxicity of some of the released gases such as NH_3 requires extra gas treatment to mitigate the emissions. In order to facilitate the process design and increase the safety of the industrial-scale production, it is necessary to degas the gas releasing reactants before adding them to the main melt synthesis reactor and where gas treatment can be more easily targeted to the species requiring it.

Lithium metaphosphate (LPO, $LiPO_3$) as the degassed form of lithium dihydrogenphosphate with a 1:1 ratio between lithium and phosphorus is a perfect replacement for gas releasing lithium/phosphate sources to be used in the melt casting process of LFP. Also, it is a more condensed source of lithium and phosphorus, i.e., the ration of lithium and phosphorus to the total mass of the reactants is higher as compared to other alternatives. Therefore, the total mass required for the synthesis with LPO as reactant decreases, meaning more LFP can be produced for a given batch volume (Equations 1.2 and 1.3). LPO has successfully been used for the synthesis of LFP through melt casting (M Talebi-Esfandarani et al., 2016).

$$2\ LiH_2PO_4 + Fe_2O_3 + C \longrightarrow 2\ LiFePO_4 + 2\ H_2O + CO \quad (1.2)$$

$$2\ LiPO_3 + Fe_2O_3 + C \longrightarrow 2\ LiFePO_4 + CO \quad (1.3)$$

LPO based solid electrolytes have also been studied for their revolutionary advantages in the next generation of LIBs (M. Chen, Yan, & Liu, 2015; Hockicko, Kúdelčík, Muñoz, & Muñoz-Senovilla, 2014; Kartini et al., 2010; Muñoz et al., 2008). Phosphate glasses like LPO and other types of glasses, namely oxides, doped oxides, sulphides, fluorides, and quenched glasses have been known as potential solid electrolytes for high energy density batteries since the emergence of LIBs (Ravaine, 1980). Their features including lack of grain boundaries, weak electronic contribution to the conductivity, plasticity, and possibility of manufacturing them in thin-film configuration, makes them a perfect alternative for conventional organic liquid electrolytes by adding the extra advantages of nonflammability and miniaturization. Although, there are still many challenges and doubts on the effective application of such electrolytes, Braga et al. in the research team headed by John Goodenough reported the first successful lab-scale implementation of glass electrolytes in LIBs last year (M. H. Braga, Grundish, Murchison, & Goodenough, 2017; Maria Helena Braga, M Subramaniyam, Murchison, & Goodenough, 2018). They have claimed to test the first LIB, charging in a few minutes with a life span of more than 20000 cycles of charge and discharge and high energy density and capacity using glass electrolytes that even gives them the possibility of replacing lithium by its cheaper and more abundant counterpart sodium.

LPO is also a member of phosphate glass family and has applications in the optics industry. (Bitar & Knowles, 2005; Karabulut, 2001; Sathiya S., 1998). Other applications of LPO includes low-temperature glass to metal seals (Chambers, Gerstle Jr, & Monroe, 1989; Peng & Day, 1991; Wei, Hu, & Hwa, 2001).

LPO is not yet commercially available in industrial production scale with an economical price. Degassing (dehydration) of commercially available lithium dihydrogenphosphate (LiH_2PO_4 or LHP) seems a straightforward reaction for its production in large scale at first glance. However, this reaction, like the dehydration of other alkali metal dihydrogenphosphates passes through a molten phase that gradually solidifies to a hard solid that severely sticks to the reaction vessel upon completion (Gallagher, 1976). Conventionally, like in the case of sodium hexametaphosphate, the collection of the product is done by subsequent melting and quenching.(Money & Hariharan, 2007)

This method is an energy-intensive process that requires an extra step of crushing and milling of the product in separate unit operation.

To solve this problem, the main objective of this research was defined to develop a ball-mill rotary-kiln (BaMRoK) reactor for the dehydration of LHP, and simultaneous milling of the produced LPO at temperatures less than its melting point. This method consists of a regular rotary kiln with or without lifters that is filled to a certain level with proper-size grinding media (stainless-steel balls). The role of the balls is to break the sticky solid product from the internal surface of the kiln.

To further develop this idea, three main objectives were defined as follows:

Objective 1: Kinetic modelling and mechanism study of thermal dehydration of LiH_2PO_4

Objective 2: Characterization of mixing and size segregation in a ball-mill rotary-kiln (BaMRoK) reactor with different particle to ball size ratios

Objective 3: Validation of the proposed kinetic and hydrodynamic models during the dehydration of LiH_2PO_4 in a pilot ball-mill rotary-kiln (BaMRoK) reactor

CHAPTER 2 LITERATURE REVIEW

This chapter is a general overview of the literature concerning the process for industrial production of $LiPO_3$. Reported chemistries leading to the synthesis of $LiPO_3$ with any yield have been reviewed. Based on this review, the most appropriate method for scale-up has been chosen. Rotary kiln and its application in conventional calcination have been explained along with the principles of ball milling to find the important aspects of these process units to be studied for their combination as ball-mill rotary-kiln (BaMRoK). Segregation as one of the important phenomena happening in both ball mill and rotary kiln and the methods for its characterization in rotating drums are also covered subsequently. Considering this literature review, the research question and the specific objectives of the thesis are formulated. More specific literature reviews of these objectives will be presented in Chapters 4 to 6.

2.1 Production of lithium metaphosphate ($LiPO_3$)

The chemistry used in the processes of production of $LiPO_3$ which are similar to the production of other alkali metal metaphosphates can be classified to the following categories:

2.1.1 Neutralization of metaphosphoric acid

Metaphosphoric acid can be prepared by heating pyrophosphoric acid or orthophosphoric acid. The resulting metaphosphoric acid is not stable in the single-molecule form so tends to polymerize to trimers or hexamers. The reactions included in these processes are as follows (Sathiya S., 1998).

$$HPO_3 + LiOH \rightarrow LiPO_3 + H_2O \quad (1.1)$$

The methods based on this group of reactions suffer from the following drawbacks (Angaiah E. A., 2003):

1. They need controlled conditions to produce $LiPO_3$.
2. More than one stage is required for the process.
3. The product is produced in aqueous solution. Therefore, it needs to be crystallized from the solution.
4. It produces much wastewater.

2.1.2 Ion replacement

Ion replacement between mono ammonium phosphate and lithium carbonate in molten phase, followed by decomposition of resulting carbonic acid and LiH_2PO_4. Mono ammonium phosphate melts at 190 °C, and lithium carbonate melts at 723 °C. The reaction between these two reactants doesn't complete unless both reactants are in the molten phase, i.e., more than 723 °C (Raskovalov A. A., 2011), (Appendix: preliminary tests). The reactions are as follows:

$$2NH_4H_2PO_4 + Li_2CO_3 \rightarrow 2LiH_2PO_4 + (NH_4)_2CO_3 \quad (2.2)$$

$$2LiH_2PO_4 \rightarrow 2\ LiPO_3 + 2\ H_2O \quad (2.3)$$

$$(NH_4)_2CO_3 \rightarrow 2NH_3 + H_2O + CO_2 \quad (2.4)$$

The processes based on this group of chemical reactions benefit from using abundant and cheap primary materials ($NH_4H_2PO_4$ and Li_2CO_3); however, it suffers from the following two disadvantages:

1. Production of toxic and corrosive gases of ammonia and carbon dioxide
2. Completion of the reaction at temperatures as high as 723 °C

2.1.3 Syntheses based on P_2O_5

The third group of $LiPO_3$ syntheses is based on reacting phosphorus pentoxide (P_2O_5) with tribasic orthophosphates, dibasic pyrophosphates, dibasic carbonates, oxides, chlorides, etc. of the alkali or alkali earth metal. The following is an example of this type:

$$Li_2CO_3\ (s) + P_2O_5\ (g) \xrightarrow{656\ °C<T\ll 723\ °C} 2\ LiPO_3\ (l) + CO_2\ (g) \quad (2.5)$$

1. Reactions of type three have been practically used in the industry at elevated temperatures. Performing these types of reactions at a high temperature can be justified as:
2. Phosphorus pentoxide (H form) sublimes at moderate temperature and vaporizes rapidly after melting (m.p.=340 °C, b.p.=360 °C).

3. Phosphorus pentoxide is produced in place by burning phosphorus, and this reaction is highly exothermic.
4. The reaction temperature is usually adjusted higher than the melting point of the product (metaphosphate) and less than the melting point of the considered alkali metal salt. This is to drain the product from the surface of the solid salt and expose the internal molecular layers of the salt to P_2O_5. There are some exceptions like potassium which its chloride melts before its metaphosphate.

For the third type of reactions, metaphosphoric acid is not stable at moderate temperatures. So, it is produced by adding water vapour to the phosphorus combustion chamber.

2.1.4 Dehydration of LiH_2PO_4

The dehydration of LiH_2PO_4 takes place in a stepwise reaction passing through different oligomer intermediates. The overall reaction is as follows.

$$LiH_2PO_4 \rightarrow LiPO_3 + H_2O \quad (2.6)$$

This reaction path was chosen and studied for our process to produce $LiPO_3$ because of the following advantages:

1. Availability of its primary material and its
2. Ease of manipulation (in contrast with other primary materials like P_2O_5 that are hygroscopic and can be dangerous upon absorbing water)
3. Near-complete yield at a moderate temperature of 400 °C
4. Emission of completely safe gas (water vapour)

The data on the dehydration of LHP is very limited in the literature. However, the dehydration of some other dihydrogenphosphates of the metals in the first group of the periodic table (MH_2PO_4 where M =Na, K, Rb, Cs) has previously been investigated (M. Brown, Dollimore, & Galwey, 1980; Osterheld & Markowitz, 1956). These reactions similarly proceed with stepwise dimerization and oligomerization. They start with the condensation of two anions by the elimination of one water molecule. These consecutive steps and their overlap with physical transitions like melting and crystallization add to the intricacy of the study of these processes.

However, the literature about these reactions is limited to the qualitative studies, and little or no detailed kinetic information has been provided.

2.1.5 Other miscellaneous methods for the synthesis of $LiPO_3$

There are also other chemical methods that have been mentioned in the literature using different sources of lithium and phosphorus(Angaiah E. A., 2003; Chung Y. S., 1962; Shyu, 1989; Stewart, 1965).

$$(NH_4)_4P_2O_7 + 2\ LiOH \rightarrow 2LiPO_3 + 4NH_3 + 3H_2O \quad (2.7)$$

$$(NH_4)_3PO_4 + LiOH \rightarrow LiPO_3 + 3NH_3 + 2H_2O \quad (2.8)$$

$$(NH_4)_2HPO_4 + LiOH \rightarrow LiPO_3 + 2NH_3 + 2H_2O \quad (2.9)$$

$$(NH_4)H_2PO_4 + LiOH \rightarrow LiPO_3 + NH_3 + 2H_2O \quad (2.10)$$

Lithium sources can vary from lithium hydroxide to other sources like lithium oxide, lithium carbonate, and lithium nitrate. In Table 2.1, some of these variations have been shown.

Other chemistries have been practiced for the production of potassium metaphosphate and sodium metaphosphate which are used in agriculture and food industry respectively. Leroy et al. patented a method utilizing orthophosphoric acid and potassium chloride to produce potassium metaphosphate between 120 °C and 850 °C (Alphonse L., 1968).

$$H_3PO_4 + KCl \rightarrow KPO_3 + HCl + H_2O \quad (2.11)$$

Most of the processes have used porcelain or alumina crucibles for small scale productions and regular rotary tube furnaces and/or tank reactors for larger scales. The overall yield in this process has been reported to be between 92-98%.

In the patent of Leroy et al. it is claimed that potassium metaphosphate has been produced by the successive two-stage process of:

1. Partially reacting of phosphoric acid and potassium chloride at 120 °C -300 °C
2. Rapidly increasing the temperature of the resulting mixture to 560 °C -850 °C

Table 2.1 Some examples of performed synthesis of LiPO3 (Angaiah E. A., 2003)

Source of Li	**Source of P**	**Molar ratio Li/P**	**T_0**	**T_f**	**Remarks**
Li_2CO_3	$(NH_4)_4P_2O_7$	52%	100 °C	600°C	Giving a yield of ~90% after 12 h
Li_2CO_3	$(NH_4)_3PO_4$	179%	-	600°C	
Li_2CO_3	$(NH_4)_2HPO_4$	230%	100 °C	600°C	
LiOH	$(NH_4)_4P_2O_7$	81%	100 °C	600°C	
LiOH	$(NH_4)_2HPO_4$	355%	-	350 °C	
LiOH	$(NH_4)_2HPO_4$	100%	100 °C	600°C	
LiOH	$(NH_4)_4P_2O_7$	25%	100 °C	600°C	
$LiNO_3$	$(NH_4)_4P_2O_7$	25%	100 °C	600°C	
$LiNO_3$	$(NH_4)_2HPO_4$	100%	100 °C	600°C	
Li_2O	$(NH_4)_4P_2O_7$	25%	100 °C	600°C	
Li_2O	$(NH_4)_2HPO_4$	25%	100 °C	600°C	
Li_2O	$NH_4H_2PO_4$	87%	100 °C	600°C	

The rapid temperature increase has been defined as 30 to 120 °C /min, and the reason for that has been mentioned as to avoid the pasty sticky phase which is produced in slow heating rates(Alphonse L., 1968). In another process patented by Rait J. S.(Rait J. S., 1960), the reaction is carried out at the surface of potassium metaphosphate to avoid the sticky phase.

2.2 Rotary kiln

The very first application of rotary kiln type reactors returns to the nineteenth century in the United States to produce cement and lime for construction purposes. In the beginning, these kilns were stationary but very soon in the 1870s and 1880s the first rotary kilns and tilted rotary kilns were established by Thomas Millen in the U.S. and by F. Ransome in England respectively (Peray & Waddell, 1986). This small tilt helped the solid materials to move gradually through the kiln and make continuous production which gave a tremendous rise to the Portland cement production in the 1880s from 42,000 to 335,000 barrels per year (Blezard R. G., 1998). At the very beginning of the twentieth century, the first long rotary kiln was introduced by the famous Thomas A. Edison in the Edison Portland Cement Works in New Jersey. Edison's rotary kilns were about 45 meters long compared to traditional rotary kilns which were around 18 to 24 meters which were exclusively used for cement and lime production.

Today the application of the rotary kilns has been increased to many fields in the industry with kilns measuring in excess of 150 meters. These applications range from lightweight aggregate for the purpose of lightweight concrete production to the still wide application in cement and lime production. Other industries that nowadays use this popular reactor heat exchanger (rotary kiln) are reduction of oxide ores, reclamation of hydrated lime, calcining of petroleum coke, hazardous waste incineration, different metal carbonates calcination, like production of lithium oxide from lithium carbonate ore, and many other solid or melt phase reactions that need high temperature with slow solid mixing (A. A. Boateng, 2015). It also has the possibility of both batch and continuous production. Other advantages of this reactor that makes it a competitive choice for many applications, over other reactor types are, its ability to be fed by various feedstocks from granular solids with different particle sizes to slurries with different solid and liquid parts, the unique possibility of maintaining distinguished phases and environments such as reducing in the solid phase and oxidizing in the gas phase and its ability to provide bed temperatures as high as 2000 K by having a flame residence time of 2 to 5 seconds.

Against all its advantages, the rotary kiln reactor also has its own difficulties such as dust generation, low thermal efficiency (in the case of flame heating), non-uniform product quality, and ringing. These difficulties can be coped with by some modification that can be customized from

case to case. Evidently, these modifications need more studying and a better understanding of the different aspects of this reactor.

Although in most of the classic applications of the rotary kiln the material inside the kiln is directly contacted with flame and hot gas, there are certain special cases like the case of our research, in which the heating is indirect through hot surfaces. In the case of the direct flame contact, the directions of the flows of the hot gas and the bed material can be co-current like rotary dryers or counter-current like calcination units. In a typical long countercurrent rotary kiln, like cement units, the stages could be divided into drying, heating, different reactions (in a vast range of temperatures) and cooling.

2.2.1 Horizontal rotary kilns versus other contactors

kiln type reactors used in the mineral processing industry may be categorized into vertical, horizontal and different combinations of these two types (Table 2.2) (A. A. Boateng, 2011).

Vertical kilns are fed from the top, and the solid material is moving downward in a plug flow while hot gases from an indirect heating source may flow upward against the down-coming packed bed or downward in the co-current cases. The particle size, in this case, should be big enough (in the order of 5 cm and corresponds to a 45 percent void fraction of the packed bed material), in order to ensure enough voidage for hot gas flow. This helps the better circulation of hot gasses through the packed bed. Annular shaft kiln is an example of this type, which is depicted in Figure 2.2.

All of these contactors have more or less the same typical temperature zones shown in Figure 2.1. The heating zone plays a very important role in the final product quality. If there is any non-uniform heating containing hot or cold spots, the final product will be of low quality. From different types of the kilns mentioned above the horizontal rotary kiln has the best control on the temperature of this zone, so it is selected as a part of the reactor for the purpose of our research, that means it should be modified to be applicable for our purpose.

Table 2.2 Typical specifications of direct and indirect contactors (A. A. Boateng, 2011)

Vertical kilns	**Horizontal kilns**	**Combination of Horizontal, Vertical and other types**
Traditional shaft-type kilns	Conventional long wet, dry rotary kilns	Fluidized-bed type kilns
Indirect gas-fired	Direct or indirect fired	Gas suspension type kilns or flash calciners
Large capacity, mixed feed, center burners	Non-contact externally heated small capacity kilns used for niche applications	Rotary hearth with the travelling grate or calcimatic kilns
Parallel flow regenerative type	Modern with recuperators such as cooler type, preheater kilns, and internals	Horizontal ring type, grate kilns, etc.
Annular or ring type	Cylindrical	Cylindrical, rectangular, etc.

2.2.2 Different types of rotary kilns

Rotary kilns are basically classified upon the form of their feed, which also determines the length of the rotary kiln. With this criterion, horizontal rotary kilns can be classified as the following types.

2.2.2.1 Wet rotary kilns

As the name shows, the feedstock of this type of rotary kiln contains water slurries. In order to evaporate the water to be able to heat the solid particles to the reaction temperature, there should be enough residence time. Therefore, the length of this type of rotary kilns is around 150-180 m, which is the longest comparing other types (Figure 2.2). This type of rotary kilns is no more used in the cement industry and have been replaced with dry kilns, which are more efficient. Nonetheless, there are specific cases like lime mud kilns in the pulp and paper industry and some applications in the food industry, where utilization of wet kilns is inevitable. According to our investigations, there has not been serious clogging or sticking issues reported for the wet kilns. The

main issue in this type of the kilns has been reported to be energy efficiency and heat transfer due to the length of the rotary kiln. For this reason, heat exchangers are usually needed specifically in the preheater sections. These heat exchangers are usually in the form of the lifters. However, in cases that these lifters produce too much dusting (also a usually encountered issue), long metallic chains are used to make the most of the hot gases passing through the kiln(Adams; HEKO, 2016).

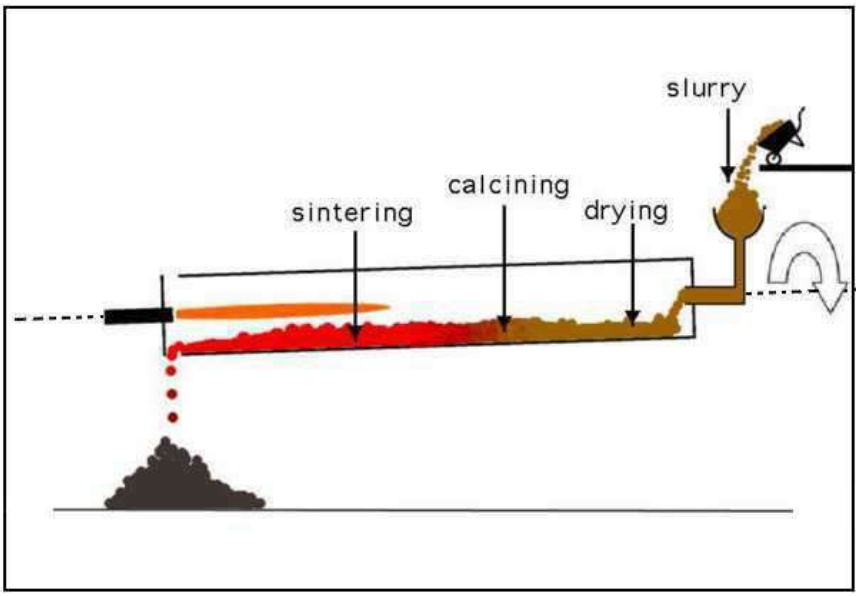

Figure 2.1 Schematic diagram of wet rotary kiln (http://www.understanding-cement.com/kiln.html)

2.2.2.2 Long dry rotary kilns

In this type of rotary kilns, the feed is in the solid form, and water exists only in the form of humidity. For the same reason as in the wet kiln, the length of this type of the kilns is shorter than wet kilns. This length is in the order of 90-120 m. However, this is still longer than the third type, because all the stages of drying, preheating and calcining occur in one single vessel. Examples of using this type of rotary kilns are lime kilns and lightweight aggregate kilns. In the latter case, the feed which is mine stones is decreased in size by crushing them to around 13 to 50 mm before being fed to the rotary kiln (A. A. Boateng, 2011).

2.2.2.3 Short dry rotary kilns

This group of rotary kilns also are fed dry materials. However, the drying, preheating, and pre-calcining steps occur in an external vessel or stage. So, the feed is already preheated, the reaction has already started, and it needs to be completed in the short rotary kiln which requires a short residence time and consequently a short length of around 15-75 m.

Some cement and lime kilns use this type of rotary kiln. In modern lime kilns, the exhaust gas is used in an external pre-heater, which is a packed bed of large limestones, instead of cyclonic pre-heaters (Figure 2.3).

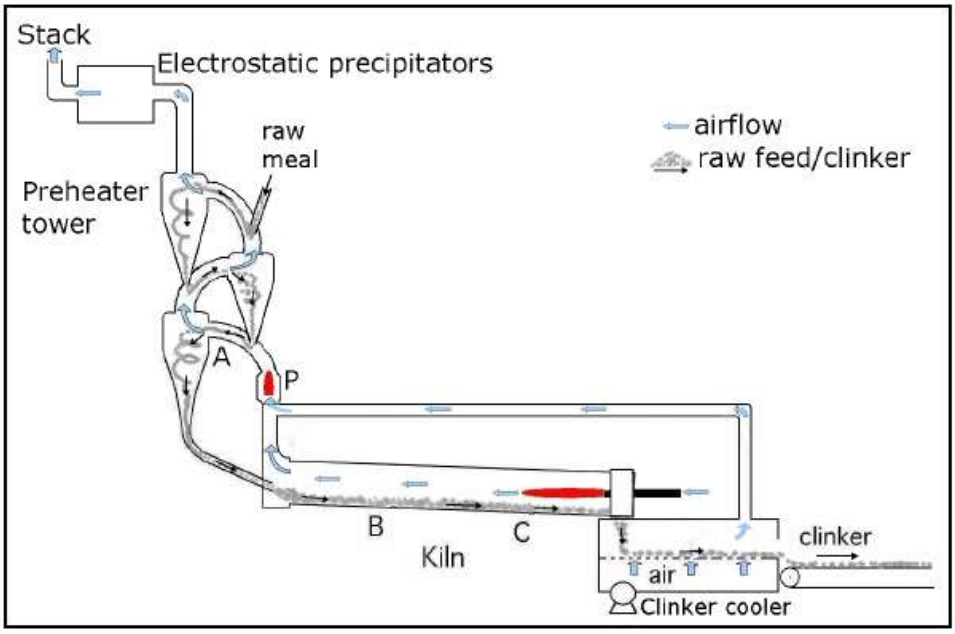

Figure 2.2. Schematic diagram of a modern dry short cement rotary kiln(http://www.understanding-cement.com/kiln.html)

2.2.3 Indirect flame and electric rotary kilns

This kind of rotary kilns is less popular than the others, especially in large scale lime or cement applications. They are mostly specific to the cases where the material to be calcined or heated should not be in direct contact with fire, so the heat source whether it is flame or electric elements

is external to the kiln. This type of rotary kilns is usually small-sized at up to 1.3 m diameter and used for very specific applications. They also have a unique advantage that is better controllability of each individual zone. Another advantage of the indirect rotary kilns is its controlled atmosphere. They also can achieve very high temperatures up to 2400 °C at each individual zone. Applications of this type include calcination, reduction, controlled oxidation, carburization, solid-state reactions like processing materials like zinc oxide, quartz ferrite, lithium carbonate and so on (A. A. Boateng, 2015; Peray & Waddell, 1986).

2.2.4 Effect of lifters on the efficiency of the rotary kiln

Mainly for the reason of heat loss prevention and also protection of the external structure from heat damages, direct flame contact rotary kilns are isolated with refractory materials. In some applications, internal lifters of different shapes and sizes are designed to increase the contact between hot gas and the solid material and increase the rotary kiln efficiency (Figure 2.4).

Table 2.3 Improvements after lifter installation in two lightweight aggregate units (A. A. Boateng, 2011)

	System 1	System 2
Change	3 rows of lifters and 3 dams installed	3 rows of lifters and 1 dam installed
Production rate	+47%	+14%
Specific heat consumption (energy HHV or LHV/ton of product)	-35%	-12%
Exit temperature (vs 25°C)	-42%	-21%
Kiln rotation speed	+70%	+31%

Although the effect of these lifters on the efficiency of the rotary kiln is considerable, application of them is not limited to this reason. In the case of our research, these lifters also have the role of grinding aid. By lifting and dropping of the heavy balls, the energy of collision increases and as a consequence the grinding becomes more efficient (S. D. Gupta, Khakhar, & Bhatia, 1991b; Tyler, 1984; Dennis R Van Puyvelde, 2009)

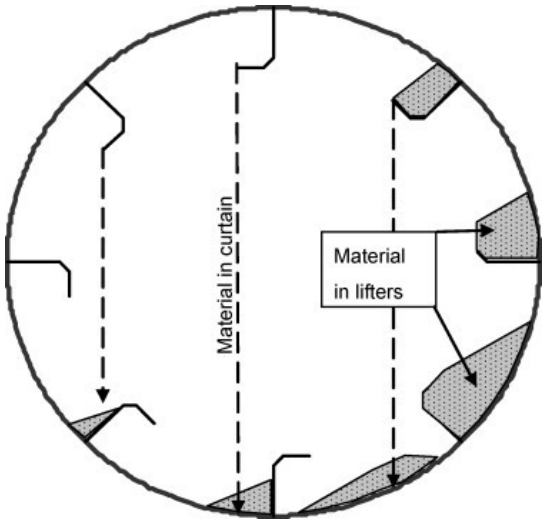

Figure 2.3. Schematic diagram of certain type lifter (L lifter) in the rotary kiln (Dennis R. Van Puyvelde)

2.2.5 Transport phenomena in the rotary kiln bed

2.2.5.1 Heat transfer

Heat transfer in a rotary kiln can be analyzed as many packed bed reactors, like shaft kiln (vertical fixed kilns discussed in previous sections). Different heat transfer phenomena occurring inside the bed are as follows: particle to particle conduction, particle to particle radiation, and convection of the gas in between the particles (Figure 2.5). However, the dominant heat transfer phenomenon results from the motion in the transverse plane which is a function of the rotation rate, degree of fill (volume percent of the kiln filled with the solid material) and the geometrical and rheological

characteristics of the particles. This motion in the transverse plane also drives the material in the axial direction (A. A. Boateng, 2011).

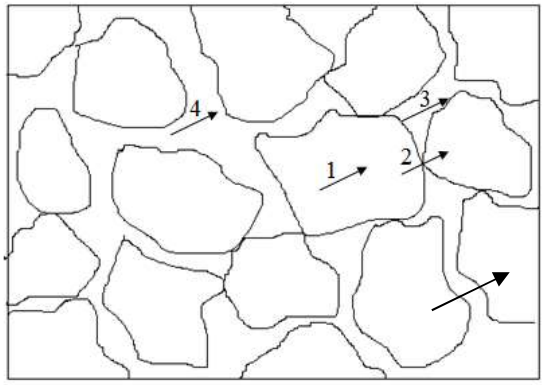

Figure 2.4. Different heat transfer phenomena in a rotary kiln bed: 1.particle internal conduction, 2. conduction between two particles, 3. radiation between two particles, 4. convection in the gas between particles

2.2.5.2 Bed motions

There are transverse and axial motions in a typical rotary kiln bed. These motions are linked together, nonetheless, for many years, they were dealt with as independent motions in the literature until recent advances in granular flow study techniques such as LDA, PIV, PEPT, and RPT happened (A. Boateng, 1998). By increasing the rotation rate, both axial and transverse mixing coefficients increase. At low rotation rates, it is expected that the residence time distribution spreads because of the velocity profile (G. Wes, A. A. Drinkenburg, & S. Stemerding, 1976).

These motions determine many parameters such as residence time which can be calculated by an empirical relation developed by the US Geological Survey in the 1950s (Perry & Green):

$$\bar{\tau} = \frac{0.23L}{sN^{0.9}D} \pm 0.6\frac{BLG}{F} \qquad (2.12)$$

In which, s is the slope of the kiln, N is the rotation rate of the kiln in rpm, L and D are respectively the length and the diameter of the kiln in ft, G is the hot gas (freeboard gas) flow in lb/hr/ft^2, and F

is the feed rate in lb/hr/ft^2 of dry material. Also, B is a constant depending on the material and is approximately calculated as

$$B = sd_p^{-0.5} \tag{2.13}$$

where d_p is the particle size.

Different transverse motion regimes depending on rotation rate and other design parameters are shown in Figure 2.6.

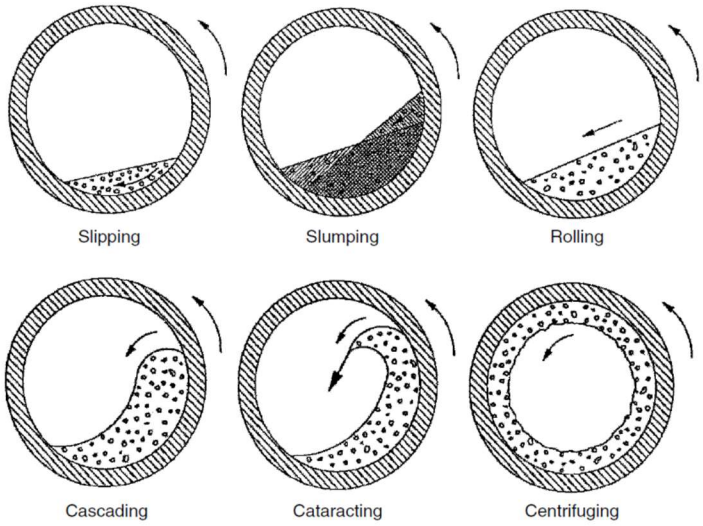

Figure 2.5 Different transverse motion regimes at different rotation rates (A. A. Boateng, 2011)

Froud number ($Fr = \omega^2 R/g$, with ω being the angular velocity of the drum, R as the radius of the drum and g gravitational acceleration) is an important dimensionless number indicating the transverse motion regimes in rotating drums. Table 2.4 shows an example of the determination of the transverse motion mode by Froud number in a rotary kiln for lime calcination.

The size of the kiln, particle rheology, and hydrodynamics, and kiln-internal features are principle design parameters to be accounted for (A. A. Boateng, 2011).

Table 2.4 Froud numbers corresponding to each of the transverse motion regimes (Henein, 1980)

Mode	$\boldsymbol{Fr = \omega^2 R/g}$
Slipping	Fr <1.0× 10^{-5}
Slumping	1.0× 10^{-5}< Fr <0.3× 10^{-3}
Rolling	0.5× 10^{-3} < Fr <0.2× 10^{-1}
Cascading	0.4× 10^{-1} < Fr <0.8× 10^{-1}
Cataracting	0.9× 10^{-1} < Fr <1.0
Centrifuging	FR > 1

2.3 Ball mill

A ball mill consists of a rotating drum (the overlapping with a rotary kiln that led to the idea of rotary-kiln ball-mill) and solid beads with different sizes, shapes, and materials called balls used for the purpose of grinding in many different applications. This method, which is one of the unit operations in the process of comminution in the industry, works based on the three forces of impact, compression, and shear or attrition.

Ball milling as a sort of comminution method is very important and omnipresent in different industries, from mining and metallurgical applications to the more miniature scale of food, pharmaceutical, and cosmetic industry. Ball mills are not only efficient at particle size reduction but also provide improved mixing, blending, dispersing and alloying (Ajaal, Smith, & Yen, 2002; Wills, 2011; Zoz, Reichardt, & Kim, 2002). There are also specific applications of mechanical synthesis for solid-state reactions in which the solid particles come in close contact to carry out the reaction. Solid-state organic syntheses like the Suzuki reaction and the Aldol condensation have been successfully performed with product yields up to 96% and >99% respectively (Nielsen, Peters, & Axelsson, 2000; Rodríguez, Rantanen, & Bolm, 2006; Schneider, Stolle, Ondruschka, &

Hopf, 2008; G.-W. Wang, Dong, Wu, Yuan, & Shen, 2008) in ball mills. The advantage of carrying these syntheses in ball mill is that they can be performed in an environment-friendly manner without the use of solvent and the ensuing product separation and drying.

There are many different ball-mills designs in the industry that have only the main concept of drum and grinding media in common. These different types may vary depending on the system of load and unload, size, material, shape, and type of movement. The ratio between length and diameter may generally vary from 0.5 to 3.5. However, in our setup, this ratio will be slightly more than this norm (75 cm/20 cm=3.75), which may be considered normal as it is going to be used as a hybrid of ball mill and a rotary kiln. The material used for the drum part is usually steel that is internally lined with a protecting coat, and the grinding media may be made from stainless steel or other metals or from many different types of ceramic materials like porcelain and alumina. The shape of the grinding media is usually spherical. However, there are special cases in which cylindrical-shaped media called Cylpebs has been used for more efficient grinding. The size of the media used in the industry may vary from 1 to 15 centimetres in diameter (Monov, Sokolov, & Stoenchev, 2012). There are different types of ball mills, drum ball mills, bead mills, horizontal rotary ball mills, vibrational ball mills, planetary ball mills, to name a few.

2.3.1 Effect of different parameters on the efficiency of ball milling

The major parameters that play role in ball milling efficiency are the load of material and balls and their ratio, drum rotation speed, size, shape, number and nature of the balls and temperature (Deniz, 2003; Erdem & Ergun, 2009; Fuerstenau, Lutch, & De, 1999; N Kotake, Daibo, Yamamoto, & Kanda, 2004). A comparison between two grinding media, spherical and tapered cylindrical beads with length to diameter ratio of unity (Cylpeb) (Figure 2.7), has been made by Shi, stating that the latter has less oversized particles due to its higher surface area and linear contact instead of pointed contact. However, the fine particles mesh has been almost the same (Shi, 2004).

Figure 2.6 Commercial grinding media in ball milling, Cylpebs versus balls

Similar to a rotary kiln, there are also different flow regimes depending on the rotation speed. These flow regimes include cascading, cataracting, and centrifuging, which correspond to slow, fast, and very fast rotations. In each case, the grinding media have a specific trajectory and impact on the ground particles.

Application of wetting agents where applicable is also a determining parameter. The particle size distribution has been narrower when smaller grinding balls have been used in wet milling, while the same effect has occurred when bigger grinding balls have been used in dry milling (Naoya Kotake, Kuboki, Kiya, & Kanda, 2011).

Other factors affecting particle size reduction in ball milling are as follows:

- Physical characteristics of the particles like mass, volume, hardness, density, and size distribution.
- Physical characteristics of the grinding media like shape, mass, density, ball size distribution
- The rotation speed of the ball mill
- Slurry density in case of wet grinding

A complete discussion of the effect of the above factors on the final particle size and particle size distribution and the estimation of these factors can be consulted elsewhere (C., 961, 1961; A. Gupta & Yan, 2006).

The capacity of the ball mill is another important operation parameter which is determined based on size and the type of the ball mill, rotation speed, particles and grinder loading, the final required particle size, work index of the particles, mill shaft power and the specific gravity of the particles.

The work index W is defined as the specific energy (kWh/ton) required to reduce a particulate material from infinite grain size to 100 microns. This index was defined by F. Bond and is used in energy equation with his name (Bond energy). This equation for the ball mills is as follows:

$$E = 10W\left(\frac{1}{\sqrt{P_{80}}} - \frac{1}{\sqrt{F_{80}}}\right) \tag{2.14}$$

where W is the work index, E is energy consumption of the mill (both in kWh/ton) and P_{80} and F_{80} are 80% passing size of the product and feed in micrometre.

There are also other studies on different operating parameters and their effect on the milling efficiency, using factorial experiment design. In one of these studies, Gao and Forssberg studied the effect of four parameters, i.e., bead density, slurry density, dispersant concentration, and the rotation speed, on the milling efficiency through 27 factorial design experiments. According to their experiments (M.-W. Gao & Forssberg, 1993; M. Gao & Forssberg, 1992; Mankosa, Adel, & Yoon, 1989):

- The bead density has an optimum value of 3.7 g/ml for the Drais ball mill that they used in their experiments. The more is the positive or negative difference from this value, the lower becomes the efficiency.
- The slurry density has a reverse relation with the energy utilization in high densities while having a negligible impact in low densities.
- In low rotation speeds, the energy efficiency is higher while the milling capacity is reduced as a cost. In higher rotation speeds the capacity increases significantly to the cost of a reasonable decrease in energy efficiency.
- Although the addition of dispersant aids in ultrafine milling, its concentration should be maintained at its minimum amount.

2.4 Mixing and segregation of solid particles and grinding media in rotary-kiln ball-mill

It is very important to know the relative situation of the solid particles and the grinding media at different steps of the process of the $LiPO_3$ production in rotary kiln ball mill. In the beginning, when fine (sub-millimetre) particles of LiH_2PO_4 are being mixed with denser and bigger (sub-decimeter) steel balls, knowing the mixing and segregation situation of our solid materials is important to find the temperature profile. At the final stage, when the reaction is complete, and the product $LiPO_3$ is being ground, this knowledge is important to assess the efficacy of the grinding.

2.4.1 Solid mixing mechanisms in rotary drums

The mechanisms of mixing in solid particles generally can be classified as the following categories (Lacey, 1954):

- Convective mixing mechanism: This mechanism can be compared to convective transport phenomena in fluids, except here, there is no such continuity as in fluids. In this mechanism, groups of particles fall, in bulk form due to the gravity and become distributed very fast.
- Diffusive mixing mechanism: Again here, we can draw an analogy between the diffusive transport phenomena. This mechanism is slow and based on small dispersion of single particles.
- Shear mixing: This type of mixing happens when a layer of solid particles moves on another layer, and the exchange of the particles happen between two layers.

In rotary drums, the mixing mechanism in the axial direction is solely diffusive while in the radial direction is mostly convection. However, the other two mechanisms also are present in this direction. Having that said, it can be expected that the mixing in the axial direction is weak (Arratia, Duong, Muzzio, Godbole, & Reynolds, 2006; Brone et al., 1997; Lemieux, Bertrand, Chaouki, & Gosselin, 2007; Moakher, Shinbrot, & Muzzio, 2000).

2.4.2 Solid particles segregation in a rotary drum

Segregation may generally occur in particulate flows due to the difference in physical and mechanical properties, such as size, density, shape, and roughness of the particles (Alizadeh, 2013). In rotating drums, this phenomenon happens in axial and radial directions. The mechanisms of these segregations are as follows:

- **Trajectory:** This segregation mechanism is based on the difference of the amount of the drag force on particles with different size and/or densities. Assuming spherical particles and the Stoke's law as governing law of the drag force, the distance X that a spherical particle with an initial velocity of u, the density of ρ_p and diameter of d will horizontally travel before stopping, in a fluid (e.g. air) with viscosity μ, is given by the following equation (Rhodes, 2008):

$$X = \frac{u\rho_p d^2}{18\mu} \tag{2.15}$$

  Therefore, bigger and denser particles move further when gravitationally fall from an inclined surface and become segregated. This is called the trajectory segregation mechanism.
- **Sifting:** As it can be realized from its name, this segregation mechanism is based on the size of the particles. When different sized particles are sliding down on the inclined surface of other particles, small particles fall into the holes and cavities of the surface, and bigger ones continue to slide to the lower parts. This segregation mechanism is called sifting (Schulze, 2007).
- **Kinetic sieving:** Like the sifting mechanism, this mechanism is based on the difference between particles' sizes, which gives more chance to the smaller particles to fall into the cavities between bigger particles. Thus the smaller particles can fall all the way to the bottom of the bed, and the concentration of the smaller particles in the bottom parts increases gradually, and segregation occurs (S. Savage & Lun, 1988).
- **Elutriation:** This segregation happens when there is a fluid flow which imposes different drag forces on particles with different sizes and densities, and as a result, larger and denser

particles settle sooner than the finer and low-density particles. This type of segregation is called elutriation.

- **Percolation:** Percolation happens when there is a deformation, due to vibration or avalanching, for instance, in a dense bed of particles that causes the particles to move against each other. So by the gravity force, the small particles start to fall into the cavities and spaces between bigger particles and shift to the lower parts while forcing the bigger particles to go to the surface (Schulze, 2007). In the case of avalanching this mechanism is called kinetic sieving.
- **Different repose angles:** Particles with a round surface and bigger size flow easier and form smaller repose angles than particles with sharp-edged surface and smaller size, due to more cohesive forces. This can be the reason for a type of segregation in granular flows with different size and shape particles.

In rotary drums, segregation happens in both axial and radial directions with a much higher speed in the latter case (F Cantelaube & Bideau, 1995). Due to the fast convective motion in the radial direction and based on the segregation mechanisms described above, small and dense particles move to the core part of the bulk mixture, near the rotation axis while bigger and denser ones flow on the free surface (F Cantelaube & Bideau, 1995; Rapaport, 2007; Thomas, 2000; Wightman & Muzzio, 1998a). Since there is only a small amount of relative movement in the passive layer, most of the segregation happens in the active layer (Aranson & Tsimring, 1999; Meier, Lueptow, & Ottino, 2007; Zik, Levine, Lipson, Shtrikman, & Stavans, 1994). Axial segregation has been studied by several researchers in the last two decades (Alexander, Muzzio, & Shinbrot, 2004; Bridgwater, Foo, & Stephens, 1985; P. Chen, Ottino, & Lueptow, 2010; Choo, Baker, Molteno, & Morris, 1998; Hill & Kakalios, 1995; A. Huang & Kuo, 2012; Rapaport, 2007; Taberlet, Newey, Richard, & Losert, 2006; Zik et al., 1994), however still the mechanism of the segregation in this direction of the rotating drums is not completely known. In these studies, the difference in dynamic repose angles and the effect of the end walls have been mentioned as the reasons for axial segregation in rotating drums.

2.4.3 Methods for characterization of the mixing and segregation in a rotary drum

As mentioned before, it is important to know the relative configuration of our grinding media and solid particles in the process of the production of $LiPO_3$ from LiH_2PO_4 in rotary kiln ball mill. To characterize the mixing and segregation situation of rotary drums, in general, the following methods have been applied in the literature and will be reviewed in the following sections.

2.4.3.1 Direct (intrusive) methods

The thief Sampling method is used to take a small amount of the mixture from a specific point and at a certain time to analyze the number and fraction of different particles that are being mixed or segregated. After taking the sample, one way to analyze it would be to fix it on a surface and perform a visual inspection upon different colours of the particles (Ottino & Khakhar, 2000). In order to be the real representative of the stream, sampling should be taken when the particles are in motion, and also it should be a uniform sample (T. Allen, 2013). The common method to take such samples is thief sampling that uses special probes with empty spaces at the tip or side of the probe end. This method may be very sensitive to many parameters, such as sample size and location (F. Muzzio et al., 2003; F. J. Muzzio, Robinson, Wightman, & Brone, 1997). Furthermore, collection preparation and analysis of too many samples is very time-consuming.

2.4.3.2 Non-intrusive methods

Transparent systems:

For transparent systems which are very limited cases, optical methods such as, Laser Doppler Anemometry (LDA), Phase Doppler Anemometry (PDA) and Particle Image Velocimetry (PIV), have been successfully applied. However, for opaque systems, these methods become inapplicable.

Opaque systems:

For the opaque systems which consist the most cases in the real world, tomographic methods such as computed tomography (CT), electrical capacitance tomography (ECT), and magnetic resonance

imaging (MRI), spectroscopic methods such as infrared (IR), and particle tracking methods such as radioactive emission tracking methods have been applied. Positron Emission Particle Tracking (PEPT) (Hawkesworth et al., 1991; Parker, Broadbent, Fowles, Hawkesworth, & McNeil, 1993) and Radioactive Particle Tracking (RPT) (Larachi, Kennedy, & Chaouki, 1994) are two of this kind of methods which have been developed in recent decades. The second method is less costly and more compact in comparison to the PEPT method, and its flexible set of detectors can be applied to larger systems.

Despite all advantages of the RPT method in the characterization of mixing and segregation in opaque granular mixtures, it has some limitations which can be mentioned as follows:

- It cannot be applied in real systems made from thick and dense walls, and instead, the vessel should be simulated.
- Because of the limitation in reducing the size of the tracer, the method cannot be applied to ultrafine particles.
- In the real-world mixtures, particles have a size distribution, so the trajectory of the tracer particle is the only representative of the particles of the same size.
- It is usually difficult to prepare a tracer with the same size, shape, density, and roughness of the inert particles.

2.4.3.3 Computational methods

The following simulation or computational methods have been used in the study of granular flows (Ottino & Khakhar, 2000):

Monte Carlo Simulation:

Monte Carlo simulations are used to draw number fraction profiles at equilibrium for mixtures of particles which are assumed to be spherical, hard and elastic, under the gravity force. The temperature is assumed to be constant all around the system as well as the total number of the particles and the total domain volume. In this method, particles are uniformly distributed at first, and then they are given displacements based on random walk theory and some other conditions

and rules until they come to equilibrium (A Rosato, Prinz, Standburg, & Swendsen, 1986; Anthony Rosato, Strandburg, Prinz, & Swendsen, 1987).

Particle Dynamics Simulation:

Particle Dynamics (PD) or Discrete Element Method (DEM) in granular flow (Cundall & Strack, 1979), is an adaptation from the methodology of molecular dynamics in the study of fluids which was first introduced by Allen and Tildesley in 1987 (M. P. Allen & Tildesley, 1989). This method is definitely more realistic than Monte Carlo simulation and needs the real values of interparticle interactions to be introduced from the experiment.

Heuristic Models:

When the particles are all of the same size, shape, and roughness, and the only difference is in their densities, then the different buoyant forces imposed to the particles will be the reason for segregation. In this case, particles with lower density are considered to be in a heavier medium and particles with higher density, in a lighter medium. This idea, for instance, is the basis of a heuristic model for the segregation due to the difference in densities, proposed by Khakhar et al. (Khakhar, McCarthy, Shinbrot, & Ottino, 1997).

Kinetic-theory-based Models:

Haro et al. proposed a complete kinetic theory for multicomponent granular mixtures of hard spheres in 1983 (de Haro & Cohen, 1984; de Haro, Cohen, & Kincaid, 1983; Kincaid, Cohen, & de Haro, 1987; Kincaid, de Haro, & Cohen, 1983). In 1989 Jenkins and Mancini showed that the equations in this theory could only be validated to the first order of approximation for hard spheres(Jenkins & Mancini, 1989). Based on this theory, the main causes of diffusion in granular mixtures are Ordinary diffusion caused by number fraction gradients, Temperature diffusion caused by granular temperature gradients, and pressure diffusion due to pressure gradients. The first factor of these three, always results in mixing, while the other two result in segregation in the presence of density and size differences(Bird, Stewart, & Lightfoot, 1960; Hirschfelder, Curtiss, Bird, & Mayer, 1954)

2.4.4 Discrete element method

In DEM simulation, Newton's second law is applied to all particles, in order to find the position of each particle in the granular flow (Bertrand, Leclaire, & Levecque, 2005; Lemieux et al., 2007; Lemieux et al., 2008).

$$m_i \frac{d^2 x_i}{dt^2} = F_i^{total} \tag{2.16}$$

$$I_i \frac{d\omega_i}{dt} = T_i^{total} \tag{2.17}$$

where m_i is mass, ω_i is angular velocity and I_i is the momentum of particle i and F_i^{total} and T_i^{total} are the total force and the torque that act on this particle. Colloidal, drag and buoyancy forces are negligible here (because of the millimetre size of the particles and air as fluid), so the main forces constituting the total force are gravity and contact forces with other particles and the walls.

$$F_i^{total} = F_i^{gravity} + F_{ij}^{contact} \tag{2.18}$$

The contact force between two particles i and j is decomposed to normal and tangential components:

$$F_{ij}^{contact} = F^n + F^t \tag{2.19}$$

Models describing normal forces can be categorized as "the continuous potential models" (Aoki & Akiyama, 1995; Langston, Tüzün, & Heyes, 1994), "the linear viscoelastic models" (Walton, 1984), "the non-linear viscoelastic models" (Brilliantov, Spahn, Hertzsch, & Pöschel, 1996; Kuwabara & Kono, 1987; J. Lee & Herrmann, 1993; Tsuji, Tanaka, & Ishida, 1992) and "the hysteretic models" (Sadd, Tai, & Shukla, 1993; C Thornton, 1997; Colin Thornton, Cummins, & Cleary, 2013; Colin Thornton & Ning, 1998; Walton & Braun, 1986)

In linear and non-linear viscoelastic models, the contact forces between two particles that are colliding to each other consists of "elastic repulsion" modelled by a spring with Hook's law and "viscous dissipation" modelled by dashpot (Figure 2.14) (Ji & Shen, 2006).

$$F^n = F^n_{elastic} + F^n_{dissipation} = -K_n {\delta_n}^{\alpha} - C_n {\delta_n}^{\beta} v^{\gamma}_{ij,n} \qquad (2.20)$$

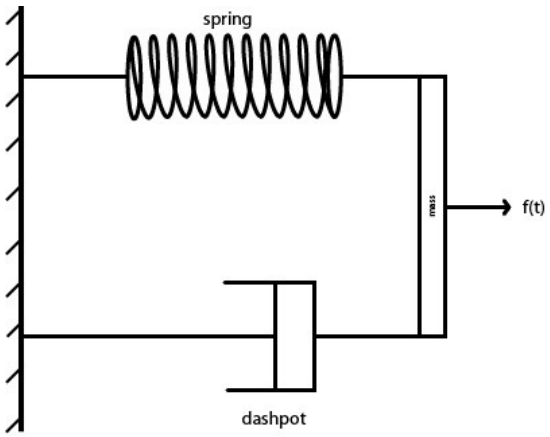

Figure 2.7 Simple schematic of spring and dashpot modelling the elastic and dissipation forces (www.wikiversity.com, 29/2/2016)

where K_n is the spring constant and C_n is the damping coefficient. With $\alpha = 1 = \gamma$ and $\beta = 0$, the model is called Linear Spring Dashpot or LSD model. In the linear contact force model, C_n is the damping coefficient and is obtained from:

$$C_n = 2\xi_n \sqrt{m_{eff} K_n} \qquad (2.21)$$

in which m_{eff} is the mean mass of particles i and j and equals the ratio of their product to their sum. ξ_n can be calculated from the following equation for LSD:

$$\xi_n = \frac{-\ln(CoR)}{\sqrt{\pi^2 + (\ln(CoR))^2}} \tag{2.22}$$

and CoR, which is the ratio of the relative velocities after and before a collision can be obtained from:

$$\ln(CoR) = -\sqrt{\frac{K_n}{m_{eff}}}\xi_n t_c \tag{2.23}$$

in which t_c is the contact time.

Mindlin and Deresiewicz have derived the following model for the tangential forces between two colliding particles, named MD model (Di Renzo & Di Maio, 2005; Mindlin, 2013; Mindlin & Deresiewicz, 1954):

$$F_{el}^t = \mu F_{el}^n \left[1 - \left(1 - \frac{K}{\mu}\frac{\delta_t}{\delta_n}\right)^{3/2}\right] \tag{2.24}$$

in which, K is the ratio of tangential stiffness to normal stiffness:

$$K = \frac{K_t}{K_n} \tag{2.25}$$

To have better precision in the results, the time step for DEM simulation should be as small as possible. However, by decreasing the time step, the number of calculations by the computer will increase. Therefore, the time step should be at most, less than the characteristic time τ_c. This characteristic time equals a typical contact time between two colliding particles (Li, Xu, & Thornton, 2005):

$$\tau_c = \frac{\pi \bar{R}}{\varepsilon}\sqrt{\frac{\rho}{G}} \tag{2.26}$$

in which ρ is the density of the particle, $\overline{R}$ is the average particle radius, $G = \frac{E}{2(1+\nu)}$ is the particle shear modulus and ε can be obtained approximately from the following equation:

$$\varepsilon = 0.8766 + 0.163\ \nu \tag{2.27}$$

For the fast colliding particles with short characteristic time, the selected time step should be small enough ($\sim 10\ \mu s$) in order to give valid results (Lemieux et al., 2008).

DEM, despite its advantages in modelling the granular motions, suffer from some limitations as follows:

- The volume of the computer calculations is high.
- The number of modelled particles is limited to computational facilities power.
- Simulations are limited to mostly spherical shapes and a few other known shapes.
- Its credibility severely depends on the particle properties obtained from the experiment.

CHAPTER 3 COHERENCE OF THE ARTICLES

As described in previous chapters, the degassing (dehydration) of LiH_2PO_4 to produce $LiPO_3$ in industrial scale is important for the scale-up of the melt synthesis process for LFP production. Therefore, the main body of this thesis (chapters 4 to 6) is dedicated to the study of the different aspects of this dehydration reaction at the lowest possible temperature in a BaMRoK reactor. These chapters are equivalent to three scientific articles published or submitted for publication with the same titles, in pertinent journals.

Chapter 4: Due to the lack of information about the mechanism and the kinetics of the dehydration reaction of LHP, the first specific objective was to determine the kinetic model of the reaction. This chapter presents a complete kinetic study of the dehydration of LHP. Isothermal and non-isothermal thermogravimetric (TG) analyses of the reaction along with differential scanning calorimetry (DSC) results were used to determine the mechanistic steps of the reaction. Based on these results, two intermediate samples were separated in sufficient amounts in isothermal conditions to be characterized by XRD and Raman. The activation energy profiles were estimated by the model-free isoconversional method and model fitting. Using this profile and the thermogravimetric studies of the first section, three intermediate species with degrees of oligomerization of 2.5, 3 and 4 were identified that convert through six reaction reaction-steps to the final product. The evaluation of the performance of the fitted kinetic model is presented for the non-isothermal analyses with different constant heating rates as well as the isothermal analyses at different constant temperatures.

Chapter 5: This chapter aims to study the configuration of the LHP particles in the bed of the balls in the BaMRoK reactor as the reported studies on the segregation of the binary particles are only limited to large size ratios. Rotating drum with a different combination of the particle sizes are considered. Two different approaches are presented to evaluate the segregation of the binary systems in a vast range of size ratios. The first approach is an innovative direct sampling method which against traditional thief sampling methods is representative of the whole cross-section of the bed and do not alter the configuration of the particles. The results of these experiments revealed two different segregation behaviours that happen in large and small size ratios. A critical size ratio with a transitional behaviour was identified that separates these two behaviours and corresponds to

the least segregation or most uniform configuration. The second approach is the discrete element method (DEM) that was used to model the same system for the purpose of comparison and evaluation. The results of the two approaches were acceptably in agreement.

Chapter 6: This chapter evaluates the kinetic and hydrodynamic models found in previous chapters during the production of LPO in the BaMRoK. Based on the results of chapters 4 and 5, ball and particle sizes were chosen to keep the material at the hottest part, i.e. the internal surface of the rotary-kiln wall. Also based on the kinetic model, the temperature was adjusted to 400 °C on the internal wall surface of the rotary kiln. LHP was dehydrated in the scale of up to 1 kg in a semi-industrial setup including a BaMRoK and characterized by XRD and Raman. Temperature of the carrier gas, internal and external surfaces of the kiln, as well as the balls, were measured during the constant rate heating, and the humidity profile of the carrier gas was measured at the same time. Temperature profiles of the bed were modelled using COMSOL Multiphysics and curve fitting. The percolation segregation predicted by the hydrodynamic model from chapter 5 and the kinetic model from chapter 4 was verified with the results of this chapter.

Finally, chapters 7 presents the conclusions of the research and recommendations for future works.

CHAPTER 4 ARTICLE 1: KINETICS OF THE DEHYDRATION OF LITHIUM DIHYDROGENPHOSPHATE

Bahman Yari, Pierre Sauriol, Jamal Chaouki[1]

Department of Chemical Engineering, Polytechnique Montreal, C.P. 6079, Succ. Centre-Ville, Montreal, Quebec H3C 3A7, Canada

Published in Canadian Journal of Chemical Engineering, https://doi.org/10.1002/cjce.23558

4.1 Abstract

Phosphate-based lithium materials, such as lithium iron phosphate (known as lithium ferrophosphate, $LiFePO_4$, LFP), are among the safest materials for large scale lithium-ion batteries due to the stability of the phosphate-bound oxygen at elevated temperature. LFP can be melt-synthesized where the kinetics are faster, allowing for coarser and lower cost reactants. Most common lithium- and phosphate-bearing reactants can react violently upon heat up and release a large volume of gaseous by-product. Lithium metaphosphate ($LiPO_3$, LPO) can improve the processability and safety of the operation. In this work, we investigate the thermal decomposition of lithium dihydrogenphosphate (LiH_2PO_4, LHP) to LPO up to 400 °C. The decomposition was analyzed by isothermal and constant rate differential thermo-gravimetric (DTG) experiments. Activation energy profiles were estimated by an isoconversional model-free approach and kinetic model fitting. $Li_5H_4P_5O_{17}$ (L2.5) was determined to be the most stable reaction intermediate, and it can be isolated at a temperature of 240 °C. The resulting reaction comprises 6 reactions, where the LHP is progressively polymerized by condensation reactions leading successively to L2.5, $Li_3H_2P_3O_{10}$ (L3), $Li_4H_2P_4O_{13}$ (L4), and LPO. The first reaction step (LHP => L2.5) was fitted with 3 reactions series/parallel describing the solid surface reaction, the viscous/liquid surface reaction, and the bulk reaction. Limiting the reaction temperature to 400 °C

[1] Corresponding author: jamal.chaouki@polymtl.ca; +1-514-340-4711 x4034

results in a solid product which can be advantageous if LPO is to be prepared in advance and dosed for LFP synthesis.

Keywords: LiH_2PO_4, $LiPO_3$, thermal decomposition, dehydration, reaction steps, reaction kinetics, isoconversional method

4.2 Introduction

$LiFePO_4$ (LFP) is a potentially inexpensive cathode material for lithium-ion batteries (LIBs) designed for the automotive market. It is also less toxic, safer, and more environmentally benign as compared to other LIB cathode material. LFP was first introduced by Padhi et al. in 1997 (A. K. Padhi, K. S. Nanjundaswamy, & J. B. Goodenough, 1997). Over the following 20 years, different LFP syntheses routes were introduced. The melt casting technique developed by Gauthier et al. at the Université de Montréal discloses a promising low-cost route to manufacture LFP (L. Gauthier, Gauthier, Lavoie, Michot, & Ravet, 2009b). This approach is currently examined at the laboratory- and pilot-scales. This process family presents advantages especially over alternate synthesis technologies, such as the solid-state process, in that it can utilize a wide range of reactants types and sizes or their mixtures as long as the stoichiometric ratios are respected, and that the reducing atmosphere is controlled within a range of acceptable P_{O_2} (Majid Talebi-Esfandarani et al., 2015). Depending on the chemistry favoured, gaseous waste streams may require treatment varying from dilution, post-combustion, or capture.

The initial work conducted at UdeM evidenced the capability of the melt-casting to handle a wide range of reactants and producing high purity LFP. This flexibility opens the door to commodity grade reactants, and even ore concentrates (Majid Talebi-Esfandarani et al., 2015; M Talebi-Esfandarani et al., 2016).

4.2.1 Gas release from potential chemistries to produce LFP

LFP through melt synthesis can be achieved with a wide range of starting materials. However, for most of the chemistries considered, one of the issues facing its scale-up especially for continuous or semi-continuous production is the sudden evolution of large amounts of gases at temperatures in the range of the LFP melting point (around 1000 °C). One considered reaction shown in Equation

1, releases 22.2 moles of different gases (NH_3, H_2O, CO_2, and CO) per kilogram of LFP synthesized, which is equivalent to 2.3 cubic meters of gas at the reaction temperature (1000 °C).

$$2\ NH_4H_2PO_4 + Li_2CO_3 + Fe_2O_3 + C \longrightarrow 2\ LiFePO_4 + 2\ NH_3 + 3\ H_2O + CO + CO_2 \quad (4.1)$$

This amount of gas is released spontaneously or at the very least in a short period of time. Therefore, operation safety concerns necessitate that this amount of gas is reduced or expelled under more controlled conditions as part of a pretreatment degassing step.

Another potential implementation of the reaction could be achieved by relying on LiH_2PO_4 (LHP) as a reactant. Solid LHP can be produced from abundant and commercially available lithium carbonate (Li_2CO_3) or lithium hydroxide monohydrate ($LiOH{\cdot}H_2O$) and industrial phosphoric acid (H_3PO_4) (Kowalski et al., 1987) after drying the solution. Direct use of LHP in the LFP synthesis (Equation 2) produces, 9.5 mol or 0.23 standard cubic meter of gas (H_2O and CO) per kilogram of LFP synthesized. Another improvement could be the use of lithium metaphosphate ($LiPO_3$, LPO) instead of LHP (M Talebi-Esfandarani et al., 2016). This rendition of the LFP synthesis reaction (Equation 3) would produce 3.17 mol or 0.07 standard cubic meter of gas (CO) per kilogram of LFP. $LiPO_3$ could be generated from the decomposition of LHP and has the added advantage of increasing the bulk density and lowering the total mass required for the synthesis, e.g., more LFP can be produced for a given batch volume.

$$2\ LiH_2PO_4 + Fe_2O_3 + C \longrightarrow 2\ LiFePO_4 + 2\ H_2O + CO \quad (4.2)$$

$$2\ LiPO_3 + Fe_2O_3 + C \longrightarrow 2\ LiFePO_4 + CO \quad (4.3)$$

Even though $LiPO_3$ can be synthesized directly from reacting metaphosphoric acid with LiOH in solution (Prakash, Tuli, Basu, & Madan, 2000) or from the solid-state reaction of different phosphates of ammonium with a lithium source such as Li_2O, Li_2CO_3, LiOH or $LiNO_3$(Angaiah, Thiagarajan, Ramaiyer, & Meenakshisundaram, 2003), these methods have the disadvantages of producing wastewater in the former and ammonia gas in the latter, which adds extra environmental and safety considerations.

4.2.2 Decomposition of alkali metal dihydrogenphosphates

Although there is limited data on the decomposition of LHP, the decomposition of dihydrogenphosphates of several other alkali metals (MH_2PO_4 where M =Na, K, Rb, Cs) was previously investigated (M. Brown et al., 1980; Osterheld & Markowitz, 1956). The thermal decomposition of acid phosphates of alkali metals generally includes more than one step. It starts with the condensation of two anions by the elimination of one water molecule. This step, along with the consecutive dehydration step/steps, may overlap with physical transitions adding to the intricacy of the study of these processes. Despite its importance, all the research about this vast category of reactions is limited to the qualitative identification of the chemical and physical transitions and little or no detailed kinetic information is available in the literature.

The onset temperature of the dehydration reaction of MH_2PO_4 (loss of 0.1% mass) decreases with the ionic radius of the alkali metal (M), but the temperature of maximum rate does not follow the same trend (Gallagher, 1976). The formation of dehydration intermediates, of the form $M_yH_2P_yO_{3y+1}$, has been reported in the literature (Bagryantseva & Ponomareva, 2016; Blinc, O'Reilly, Peterson, & Williams, 1969; M. Brown et al., 1980; Gallagher, 1976; Martinez, Botez, Tackett, & Chianelli, 2009; Park, Lee, & Choi, 2001; Pechkovskii, Shchegrov, Mel'nikova, Shul'man, & Gusev, 1968). Osterheld et al. showed that $Li_2H_2P_2O_7$ (L2), $Cs_2H_2P_2O_7$, are stable at the temperature of formation, i.e., up to 240 °C, but $K_2H_2P_2O_7$ was not and rather readily decomposed to KPO_3. TGA and DTG curves of the dehydration of KH_2PO_4 (also KD_2PO_4) and RbH_2PO_4, support the observation that the intermediates readily transform to the metaphosphate form, however, the peaks in the corresponding DTG curves were overlapping, suggesting various oligomer intermediates (Gallagher, 1976).

Phase transitions prior to or during the decomposition of the alkali metal dihydrogenphosphates have attracted substantial attention. Lee et al. studied these phase transitions by monitoring the dielectric constant and electrical conductivity of LiH_2PO_4 crystals from room temperature to 220 °C and observed two anomalies in dielectric constant at 178 °C and 196 °C. These dielectric anomalies coincided with increases in electrical conductivity to superprotonic magnitude at almost the same temperatures: 0.03 $\Omega^{-1}cm^{-1}$ at 178 °C and 10 $\Omega^{-1}cm^{-1}$ at 196 °C. They suggested thermal decomposition on the surface of the particles, as the most probable reason for their observation

(K.-S. Lee, Moon, Lee, & Jeon, 2008). They had previously suggested the following general reaction for the first step of the decomposition reaction of dihydrogenphosphates of alkali metals (M= K, Rb):

$$y\ MH_2PO_4\ (s) \rightleftarrows M_yH_2P_yO_{3y+1}\ (s) + (y\text{-}1)\ H_2O\ (g) \qquad (4.4)$$

in which, dehydration or polymerization reaction (left-to-right arrow), which is an endothermic reaction, takes place as soon as the phase transition temperature is reached, hydrolysis or depolymerization reaction (right to left arrow) happens under appropriate water vapour pressure (K.-S. Lee, 1996). Abdel-Kader et al. observed that the dehydration of $K_2H_2P_2O_7$ to KPO_3 happened in two steps (265 °C and 310 °C) after a phase transition at 230 °C. They calculated the activation energies for these steps by an isoconversional model-free method (Abdel-Kader, Ammar, & Saleh, 1990).

4.2.3 Present study

Our study investigates the thermal decomposition of LHP to LPO and is divided into two main parts. In the first part, we distinguish different steps of the overall reaction by TGA, DTG, and DSC techniques. We then isolate reaction intermediates for characterization. In the second part, we apply isoconversional methods to determine the activation energies and propose a kinetic model. Here, we try to apply the recommendations of the Kinetics Committee of the International Confederation for Thermal Analysis and Calorimetry (ICTAC) (M. Brown et al., 2000; Burnham, 2000; Maciejewski, 2000; Vyazovkin, 2000; Vyazovkin et al., 2011; Vyazovkin et al., 2014).

4.3 Materials and methods

Battery grade crystalline LHP with less than 0.5 % impurity was supplied by Sichuan Tianqi Lithium Industries Inc., China. LHP is sensitive to humidity and agglomerates over time. At the time of use, the LHP supply had agglomerated into lumps that were larger than a few centimetres in size. These lumps were easily broken down to reveal a particle size ranging from 250 to 350 µm. Melting of these particles starts at around 210 °C based on DSC (Figure 4.5). This is in accordance with other observations in the literature (Benkhoucha & Wunderlich, 1978; Bernard Wunderlich, 1990). The LHP was ground down using a mortar and pestle and sieved into the

class 25-75 µm. Another considered starting material was LHP droplets obtained by spray drying a 1 M solution of LHP (made by dissolving dried solid salt in distilled water) and yielding a particles size of around 10 µm. To minimize the regrowth, all the LHP materials were kept in a vacuumed desiccator until used. The 10 µm class of particles was very cohesive and did not provide repeatable results due to regrowth despite the desiccator. We thus selected the 25-75 µm class for the majority of the trials to limit the influence of particle size on heat and mass transfer during the decomposition reaction (Klaewkla, Arend, & Hoelderich, 2011).

The morphology and size distribution of the LHP was studied by scanning electron microscopy (SEM; model JSM-7600 TFE, JEOL, Japan) at 2 kV with LEI imaging mode and a working distance of 8.5 mm.

The starting LHP, intermediates, and the final product were characterized by X-ray diffraction (XRD). The XRD was performed with a Philips X'Pert diffractometer (Now Panalytical B.V., The Netherlands) with Cu Kα radiation (0.154 nm) at a generator voltage of 50 kV and a current of 40 mA. The scanning rate was 0.02°/s, with a resolution of 0.02°.

For Raman characterization, we used a Witec alpha300 access confocal Raman microscope equipped with a motorized stage, CCD detector, and 1800 grooves/mm optical grating. The light source was a 532 nm Cobolt laser with 25 mW power. The spectra were obtained at 514 nm excitation wavelength, with 50x collecting lens, and 10 seconds for signal integration time.

Isothermal and high-resolution TGA tests were performed. The isothermal tests were conducted to intercept stable intermediates to distinguish different steps of the overall reaction, whereas the high-resolution tests were to generate data for kinetic modelling following isoconversional model-free method and also to help distinguish reaction steps. All the TGA tests were performed using a TA Instruments Q-5000, under a 40 mL/min nitrogen flow. The isothermal tests were performed on samples of approx. 15 mg. The heating ramp was 10 °C/min from 110 °C to a final temperature isotherm ranging from 180 to 400 °C. The high-resolution tests used approx. 5 mg samples. The ramp rates were 1, 3, 5, 7, 10, 15, 20, 25, and 30 °C/min from 110 °C to 400 °C. For both approaches, the LHP was heated from ambient temperature to 110 °C and held 10 min to eliminate excess moisture it may have contained prior to initiating the analysis. The mass after the 110 °C hold was taken as the dry mass of LHP defining the 0-conversion extent (α).

Physical and chemical transitions were analyzed by differential scanning calorimetry (DSC) using a TA-instruments Q-2000 differential scanning calorimeter with 1 °C/min constant heating rate from ambient to 400 °C with a starting sample mass of approx. 5 mg, and a gas flow rate of 50 mL/min of nitrogen.

Larger quantities of reaction intermediates were prepared by putting approx. 100 g of LHP in a programmable muffle furnace (3-550 series Ney Vulcan). The resolution of the temperature reading was 1 °C, and the accuracy was ±5 °C. The resolution of the heating rate was 0.1 °C/min, and the temperature uniformity of the furnace was ±8 °C. The temperature was increased to 110 °C with a rate of 10 °C/min and remained for 15 min to evaporate the free humidity, and then it was increased to a desired final temperature at a rate of 5 °C/min where it remained for 6 h. The intermediates were cooled down to 120 °C in the muffle furnace at a rate of around 1 °C/min and cooling to room temperature was done inside a vacuumed desiccator, where the powders were kept until they were used or analyzed.

4.4 Results and discussion

4.4.1 Part 1: Identifying the main reaction steps

TGA analysis is a simple yet effective tool to investigate the decomposition of LHP to LPO since the loss in mass (water) associated with the reaction is 17.3% of the start mass is well within the measurement capacities of the instrument. Past reports on LHP dehydration to LPO, based on the work of Thilo et al. have suggested that a step-growth homogeneous reaction (ref: Wunderlich 1990 and 1968) leading to a Flory-Schultz distribution of oligomers up to the point where nucleation occurs after which the mechanism becomes chain growth (Thilo & Grunze, 1955; B Wunderlich, 1968; Bernard Wunderlich, 1990). Benkhoucha and Wunderlich, initially intended to model the reaction as a general step-growth but found that the amount of L2 was excessive and did not track well with the assumption, they modified their step-growth model to allow a 200 times greater rate constant for the formation of L2 compared to all other oligomers (Benkhoucha & Wunderlich, 1978). This, in effect, was similar to defining the L2 formation as sequential and the other oligomer formation as step-growth. Osterheld and Markowitz also observed a high concentration of L2 with the near absence of higher oligomers (Osterheld & Markowitz, 1956).

Our isothermal TGA investigation of the 25-75 µm class particles have shown rate transitions when approaching the key conversion extents associated with the dominant formation of specific oligomers L2.5 ($\alpha = 0.6$), L3 ($\alpha = 0.666$) and L4 ($\alpha = 0.75$). The sequential formation assumption is consistent with such observations. Optimization of the isoconversional data for the same particle class was also consistent with rate transitions occurring at those conversion extents supporting the assumption. The decomposition beyond conversion extents greater than 0.75 was far from trivial, and the reaction in this region exhibits a more complex behaviour, especially when examining the activations energy, perhaps indicative of nucleation, crystal growth and annealing steps as suggested by Benkhoucha and Wunderlich (Benkhoucha & Wunderlich, 1978).

According to (Equation 4), assuming that the reactions are forming the oligomers in sequence, we would expect the first 3 oligomers (y =2, 3 and 4) to have been produced at mass losses of 8.7% ($\alpha = 0.5$) for $Li_2H_2P_2O_7$ (L2); 11.6% ($\alpha = 0.667$) for $Li_3H_2P_3O_{10}$ (L3); and 13.0% ($\alpha = 0.75$) for $Li_4H_2P_4O_{13}$ (L4).

For the purpose of identifying the reactions steps, we applied a constant heating rate as well as isothermal programs for thermogravimetric analysis. To distinguish between surface-solid-state reaction and molten or sintered phase bulk reaction (the first two peaks of the TGA), we compared the ground (25-75 µm) and the original (250-350 µm) particle classes. TGA and DTG conducted on the fine particle with a heating rate of 1 °C/min show four distinguishable steps (Figure 4.1a) with maximum rate peaks identified as peaks 1-4. For the original particle class (Figure 4.1b), the same 4 peaks can be observed in the DTG curve. However, 3 minor peaks (identified as 2a, 2b, and 2c) between peaks 2 and 3 are also present. When identifying the position of the potential oligomers on the TGA curve and projecting onto the DTG curves, we can see that peaks 1, 2 and 2a occur prior to the mass loss equivalent to the complete conversion of LHP into L2. Relatively the size of peak 1 is greater for the fine particles than for the coarse particles and is attributed to a surface reaction. The temperature where it occurs is consistent with the observations of Lee et al. (K.-S. Lee, Moon, et al., 2008). Peak 3 covers the appearance of L3 and L4 and ends well after the mass loss equivalent of L4 is reached. Peak 4 is small but visible when reaching above 350 °C and 375 °C for both classes of particles respectively. The conversion equivalent would be consistent with high-level oligomers with $y >> 4$. For the larger class particles, the 2b peak coincides with a mass loss equivalent to a composition of L2. However, peak 2c occurs at a conversion well between

those corresponding to L2 and that of L3. The onset of the peak coincides with a remaining mass between 89.5% and 90% which is close to an oligomer with composition $Li_{2.5}H_2P_{2.5}O_{8.5}$, equivalent to ½ $Li_5H_4P_5O_{17}$ (oligomer with y = 2.5, henceforth L2.5). For the smaller particle class, the equivalent L2.5 composition occurs at the onset of the peak 3.

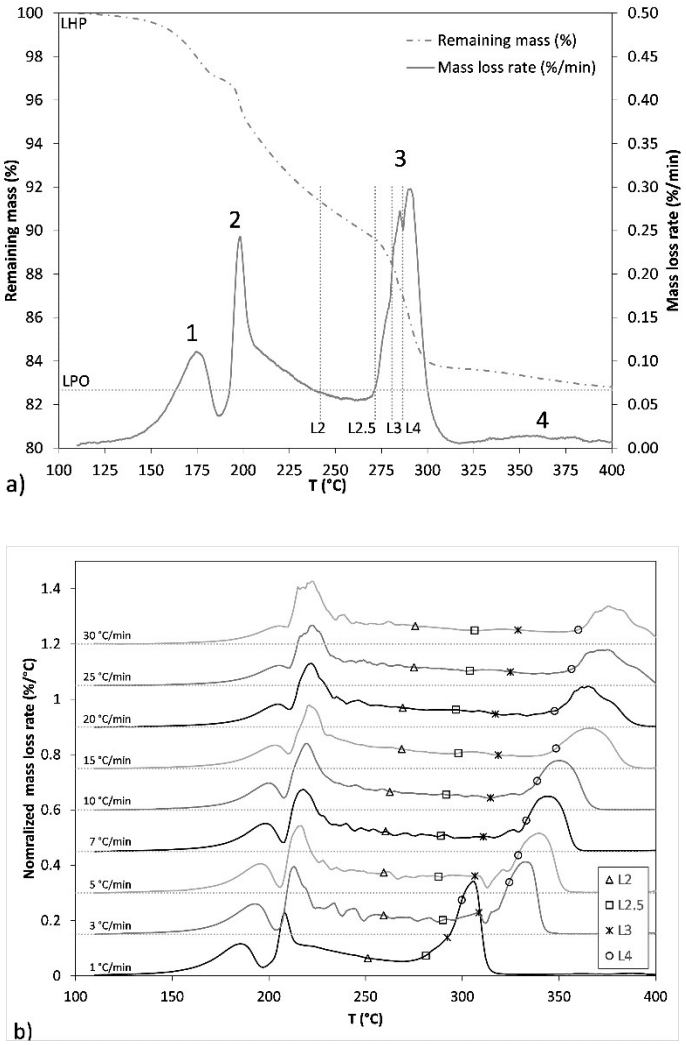

Figure 4.1 TGA and DTG of LiH2PO4 with constant heating rates, locations where mass loss coincides with specific intermediates are identified for reference. (a): 25-75 µm particle size, 1°C/min heating rate (b): 25-75 µm particle size, 1-30 °C/min different heating.

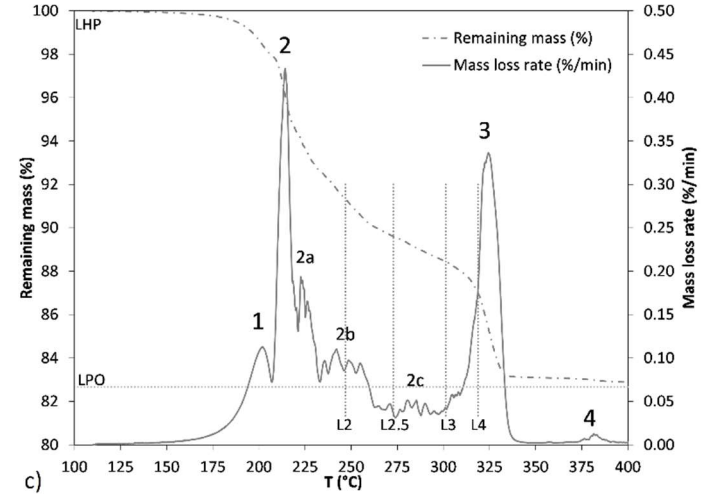

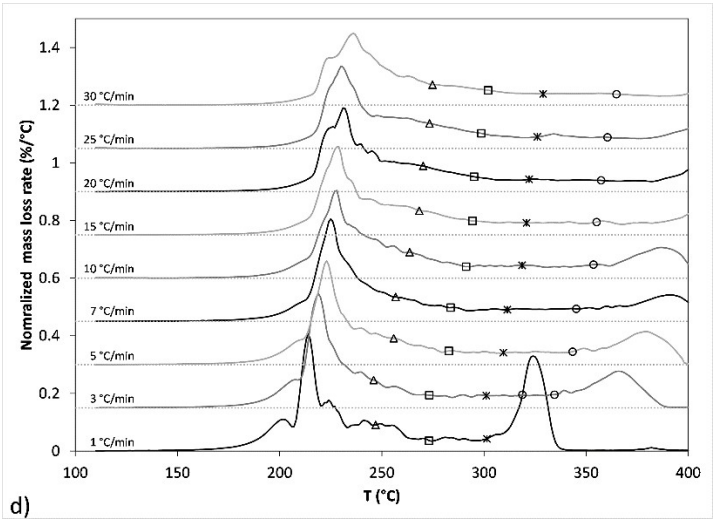

Figure 4.2 TGA and DTG of LiH2PO4 with constant heating rates, locations where mass loss coincides with specific intermediates are identified for reference. (c): 250-350 µm particle size, 1°C/min heating rate (d): 250-350 µm particle size, 1-30 °C/min different heating rates.

Reaction step 1 with 25-75 µm particle size, has a peak at T = 172 °C and reaches its slowest reaction rate (end of the step), at T = 186 °C, and α = 0.20 (Figure 4.1a). However, with bigger particles, i.e., 250-350 µm, the maximum reaction rate is at 202 °C and the slowest reaction rate (end of the step) happens at T = 207 °C, and α = 0.12 (Figure 4.2). As LiH_2PO_4 is still in solid form at these temperatures, this difference in the extent of conversion (0.08), between two particle sizes

is due to the difference in their specific surfaces. Therefore, this step is attributed to the surface reaction. The respective conversion extent is consistent with the first step involving approx. a 5 and 10 μm thick layer respectively for both particle classes.

Reaction step 2 for the smaller particles (25-75 μm) reaches a maximum reaction rate at T = 198 °C, and the reaction slows down until it reaches a minimum rate at T = 262 °C and α = 0.57 (Figure 4.3). This is close to a composition equivalent to L2.5. On the other hand, for the bigger particles (250-350 μm), the maximum reaction rate is at T = 214 °C, and the minimum reaction rate is at T = 301 °C and α = 0.66 (including the minor peaks), closer to the composition equivalent to L3. In both cases, there is a slow drop of the reaction rate after the peak, which is because of the gradual liberation of vapour bubbles from the viscous phase. In the case of bigger particles, there is also some fluctuations in the reaction rate in this region for the same reason.

In reaction, step 3 covers the decomposition from L2.5 (25-75 μm) and L3 (250-350 μm) to mostly LPO ($y >> 4$). This step reaches the maximum reaction rate at T = 291 °C and T = 325 °C for 25-75 μm and 250-350 μm particles respectively, at a composition equivalent $y > 4$. It also slows down to a minimum rate at T = 318 °C, and between T = 345 to 365 °C, for 25-75 μm and 250-350 μm particles, respectively. These conversion extents are between those expected for LPO and L4. Higher-order oligomer with $y > 4$ are not considered herein, but the conversion extent at the end of step 3 of around 0.97 corresponds to a y of 30.

Reaction step 4 gives a very small but wide DTG peak at T between 325 to 400 °C with a maximum rate around 365 °C for the 25-75 μm particles. The peak is sharper for the coarse particle with a maximum at T = 382 °C. The reaction becomes near-complete ($\alpha > 0.99$) at T = 400 °C for both particles classes. This step is attributed to the conversion of higher polymer ($y \geq 4$) to LPO.

Despite the difference in the range of temperature and conversion extent describing steps 1 and 2 for both particle classes, the temperature at which they reach a mass loss equivalent to the sole conversion to L2 and L2.5 as identified in Figures 4.1 and 4.2 are similar at 244 ± 2.5 °C and 272 ± 0.7 °C, respectively. The size effect becomes more important when reaching L3 and L4 equivalent compositions with temperature differences of 20 °C and 30 °C between the two particle-classes, the larger particles always requiring a greater temperature (and time, since constant rate heating is used) to achieve the same conversion extent. The temperature required to finish the

decomposition reaction and reach LPO compositions from the highly polymerized intermediate state during step 4 lies within 1 °C as both particle classes reach a conversion extent of 0.99 at 395 °C.

From the TGA and DTG with most peaks coinciding to specific oligomer compositions, we can assume that the decomposition of LHP to LPO generally follows a step-wise evolution.

4.4.1.1 Reaction intermediates

The peak and transition temperatures steps 1-4 observed in Figure 4.1, may slightly differ from the isothermal temperatures at which these steps occur. To confirm the stepwise approach and help identify the decomposition intermediates and their stability domains, a series of isothermal TGA runs were performed. In each run, the sample was heated at 10 °C/min (except 20 °C/min in a few cases) up to the isothermal temperature where it was held for a sufficient time to find the trends (Figures 4.3 and 4.4). The temperature range investigated is based on the observation from Figure 4.1. The isothermal tests, as opposed to constant rate tests, allow us to slow down the reaction approaching a given temperature and this, in turn, allows to evidence with greater sensitivity the rate changes approaching various reaction intermediates. This information will allow us to identify and isolate stable intermediates for characterization.

Figure 4.3a shows that only for isothermal temperature above 210 °C that LHP can pass the step one (surface) and two (bulk) and completely convert to L2 (exceeding it) in a reasonable time of 2 hours. Beyond this time, the material continues to decompose at a slow rate reaching almost a plateau. The conversions at the 210 °C and 220 °C isotherms after 6 hours are around 90.5 and 90.0% remaining mass, respectively. This corresponds to conversion extents of $\alpha = 0.55$ and 0.58, between those expected for L2 and L3, in agreement with observations at the end of step 2 in Figure 4.1a. The mass loss pattern at 220, 210 and to a lesser extent 200 °C seem to approach that equivalent to a conversion extent of 60% which would be consistent with the production of L2.5. This contrasts with previous reports of a stable L2 intermediate up to 240 °C (Osterheld & Markowitz, 1956).

In fact, the mass loss patterns of Figure 4.3a for 210 and 220 °C do not show a notable slowing down of the upon approaching the L2 equivalent conversion, suggesting that such a compound may not form under the test conditions (dry nitrogen) even as a metastable compound. The 200 °C

isotherm is the only one that presents a slowing down of the reaction approaching L2. The isotherms at 240, 260 °C break, through the L2.5 equivalent conversion line. At 260 °C, the mass-loss rate slows down prior to reaching beyond a conversion equivalent of L2.5, which is not observed at 240 °C. L2.5 can only form, at a limited range of 200 °C - 240 °C, preferentially around 220 °C considering the reaction rates.

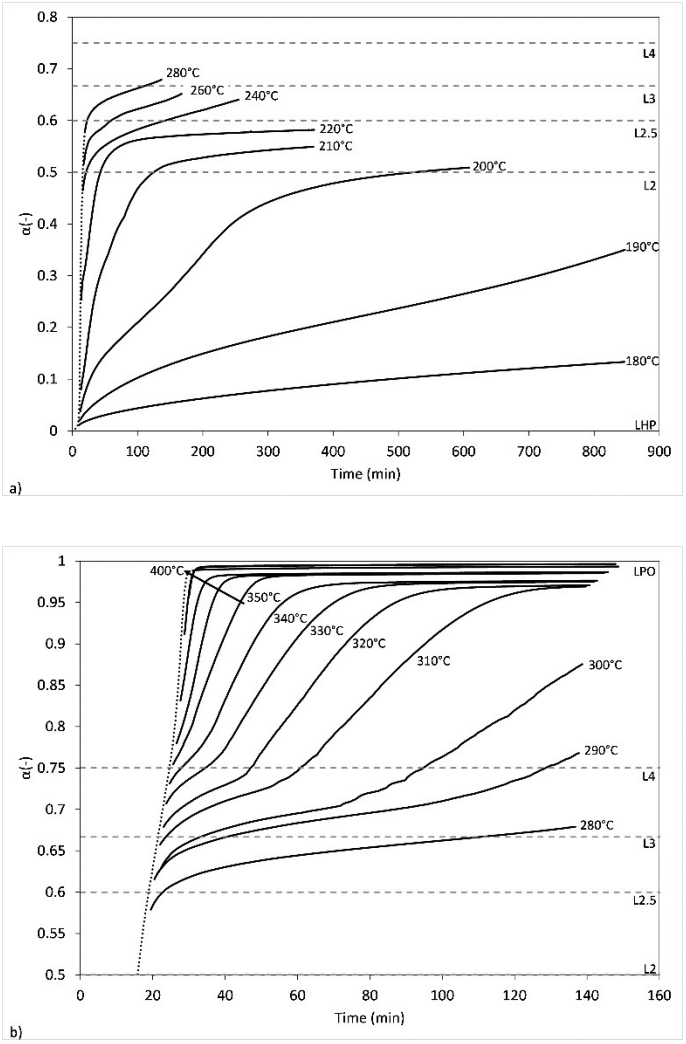

Figure 4.3 Combined constant heating rate/isothermal TGA curves of LHP and intermediate #1 at different final temperatures. (a): LHP (180-280 °C), (b): LHP (280-400 °C), 25-75µm and ramp rate 10 °C/min

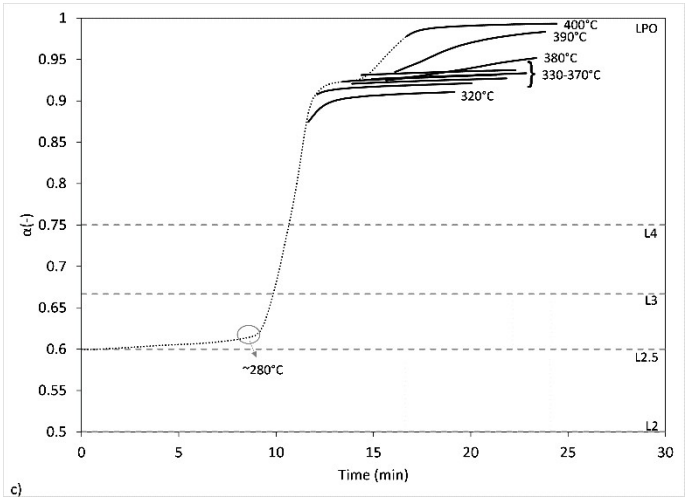

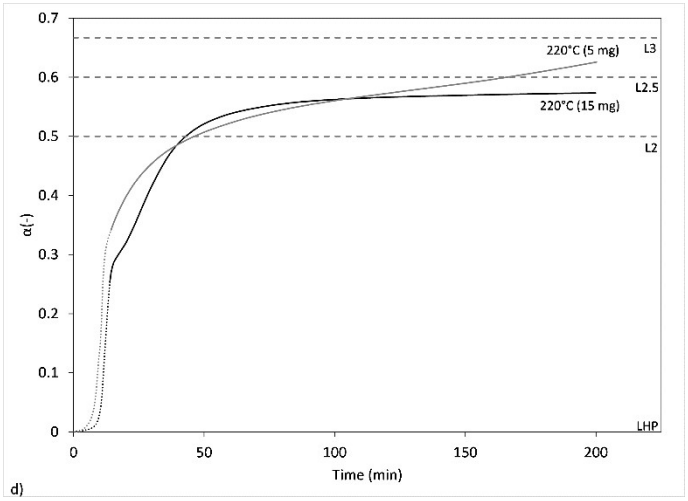

Figure 4.4 Combined constant heating rate/isothermal TGA curves of LHP and intermediate #1 at different final temperatures. (c): 1st Intermediate (320-400 °C), (d): effect of starting mass for 220°C isotherm (5 mg vs 15 mg). In (c) re-ground after synthesis 25-75 µm and ramp 20 °C/min, in (d) 25-75µm and ramp rate 10 °C/min;

The data obtained above 260 °C show that L3 and L4 are metastable intermediates (Figure 4.3b). At the lower temperatures (< 300 °C), the reaction typically slows down on the approach to the L3 composition and accelerates again as the conversion crosses it. The data for temperature isotherms between 320 °C and 350 °C exhibits a similar slow down/acceleration around the conversion

equivalent of L4. At 330 °C and above, the near-complete conversion of LHP is achieved with residual mass equivalent to a conversion extent around 0.98, similar to the conversion extent before step 4 in Figure 4.1a or a oligomer with a y value of 30 according to the general formula, although the composition is more likely to be that of LPO with a small fraction of residual oligomer(s) having a lower y value.

A larger quantity (100 g) of intermediate #1 was obtained at 220 °C where it was held for 6 hours by isothermal procedure and reground to 25-75 μm to eliminate agglomeration that took place during its preparation. Taking this intermediate as starting material, we examined isotherms in the range of 320-400 °C (Figure 4.4c). The data presented here is rescaled so that the scale matches those of the LHP – LPO conversion; the final mass at 400 °C isotherm intermediate corresponds to the near-complete conversion to LPO as obtained in the other 400 °C isotherm starting with LHP. Below 110 °C, free moisture accounting up to 0.5% of the starting intermediate mass is released. This contrasts with LHP that typically contained about 0.1% of such free-moisture. After drying the sample and resuming the ramp, the rescaled data shows that the conversion extent of the starting intermediate #1 is very close to that of L2.5 with a conversion extent equivalent to 0.602. This disproves the stability of L2 up to 240 °C, at least under dry conditions. When the temperature reaches around 265–270 °C, the conversion extent of the intermediate is around 0.62 before the mass sharply drops to a conversion extent below 0.91 in the temperature range 325–340 °C leading to a stable plateau at a conversion extent of 0.93. This occurs much earlier than when decomposing LHP directly. As opposed to observation in Figure 4.3b, the mass loss data does not show a slowing down when crossing the mass corresponding to L3 and L4. On the contrary, the mass loss accelerates, but as opposed to Figure 4.3b, here the temperature is still increasing towards the isotherm when the L3 and L4 equivalents are reached. In fact, the temperature is still increasing when the plateau associated with the higher-level oligomers is reached. For all isotherms in Figure 4.4c, upon reaching a conversion extent of 0.93, temperatures of 390 and 400 °C are required to complete the conversion to LPO within a short time of 15 and 5 min respectively. At 360–380 °C, a mass loss is observed but small requiring in excess of 40 min at 380 °C, determined by extrapolation, to complete the conversion to LPO. This temperature range for the finalization of the conversion of LPO is consistent with observations of step 4 in Figure 4.1a. However, the mass amount attributed to oligomers exceeds those determined when processing LHP directly (Figure

4.1a and Figure 4.3b). The conversion extent of 0.93 corresponds to a y value of 15. The greater mass loss rate observed with the intermediate isolated at 220 °C can be in part explained by lower mass transfer resistance. After its production, the intermediate was ground/deagglomerated to the 25–75 μm range using a mortar and pestle. On the contrary, when starting from LHP, sintering and particle size growth takes place around the melting point.

The isotherms were generated with a starting mass of approx. 15 mg. The effect of the starting mass was examined at 220 °C, where a 5 mg sample was also tested (Figure 4.4d). In this figure we can see that upon reaching 220 °C (transition from dotted lines to solid lines), the 5 mg sample has achieved a conversion extent far greater than the 15 mg sample (0.34 vs. 0.25). This conversion remains greater up to a time of 40 min after which both conversion extents remain within 0.02 up to a holding time of 100 min where the 5 mg sample continues to lose mass while the 15 mg sample exhibits a plateau approaching a conversion extent equivalent to L2.5 while the 5 mg sample breaks through the L2.5 equivalent accelerating around the transition point. After nearly 370 min, the conversion extent of the 5 mg sample reaches a conversion extent of 0.78. The effect of sample size is believed to be the result of transfer limitations that can arise from the sintering of particles during the heating of the sample. Despite being a generally porous arrangement, the particles in the 15 mg sample generally pile up as a single mound, while the 5 mg sample presents a few dispersed lumps at the bottom of the pan with much less contact between each lump.

4.4.1.2 Characterization

Based on the observed transition temperatures, two reaction intermediates were produced in larger amounts using a muffle furnace so that they could be further characterized by DSC, X-ray, and Raman spectroscopies, along with LHP and LPO. The first intermediate (L2.5-rich), is produced at an isotherm of 220 °C, while the second intermediate (LPO-rich, with traces of oligomers) was produced at an isotherm of 350 °C.

Complementary DSC confirms that endothermic peaks of LHP correspond to reaction DTG peaks 1-3 (Figure 4.5). While peaks 1 and 2 are clearly observed on the DSC for the LHP, peak 3 is not. Instead, it presents a wide endothermic transition between 250 and 310 °C. On the other hand, for the 1st intermediate (220 °C), only a sharp peak ranging from 285–315 °C corresponding to step 3 is observed. In contrast, the 2nd intermediate (350 °C) does not show any transitional peaks and

generally mimics the baseline signal of both LHP and 1st intermediate. In all DSC cases, the peak attributed to DTG peak 4 is not perceived clearly. Furthermore, it appears that the processes involved with the minor DTG peaks 2a and 2b (between 225 and 260 °C) could be mildly exothermic, as the heat flow from LHP sample lies slightly above the baseline derived from the intermediates, which could be because of nucleation and subsequent crystallization. Also, the peaks at 218.1 °C and 302.2 °C in the DSC correspond to the melting of LHP and the 1st intermediate that increase the mobility of the reactive and increase the oligomerization rate.

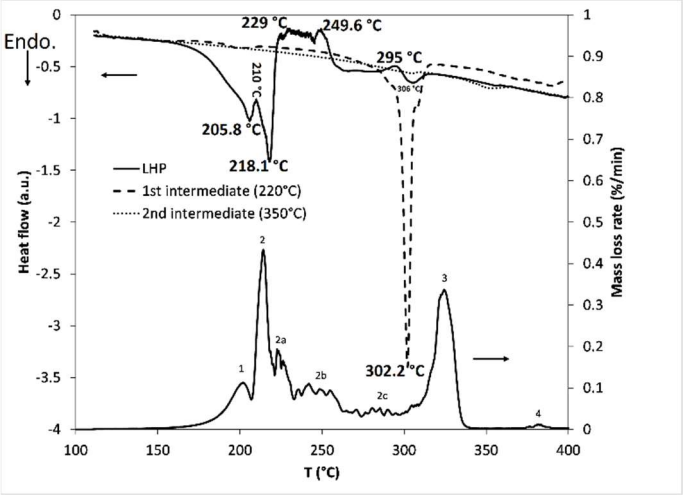

Figure 4.5 DSC and DTG of LHP (250-350 μm particle size) along with DSC of 1st and 2nd intermediates (220 and 350 °C), at 1 °C/min constant heating rate

LHP, 1st and 2nd intermediates and product LPO present notable discrepancies in their X-ray diffractograms, owing to the transformations taking place during the decompositions of LHP (Figure 4.6). Crystalline LHP has an orthorhombic crystal system, a $Pna2_1$ space group (number 33) with lattice parameters a = 6.241 Å, b = 7.643 Å, c = 6.870 Å, with Z = 4. In the low range 2θ angle, it has 12 strong peaks with the strongest ones being at 22.5°, 35°, and 17.5° with Miller indices (111), (022) and (011), respectively (K.-S. Lee, Oh, Kweon, Lee, & Ahn, 2012). These peaks completely disappear in the 1st intermediate (220 °C) and instead new peaks at 2θ = 21°, 22°, 28°, 33°, and 34° appear. These new peaks become weak in the 2nd intermediate (350 °C) and completely disappear in the final product, LPO (at 400 °C). Only 2 peaks present in the 2nd

intermediate, those at 29° and 31°, do not belong to either LPO or to the 1st intermediate. Therefore, the 2nd intermediate can be taken as a mixture of LPO, predominantly, with small amounts of the 1st intermediate remaining and very small amounts of a higher y oligomer, that will decompose to LPO at around 390–400 °C. The LPO sample shows characteristic peaks at 2θ angles of 16.5°, 18.5°, 25°, 27.5°, with a monoclinic structure with lattice parameters of a = 13.074 Å, b = 5.4068 Å, c = 16.452 Å, with Z = 20, and space group of P2/m (Murashova & Chudinova, 2001). In one extreme case, we heated the LPO above its melting point (656 °C), with no loss of mass, and quenched it rapidly by pouring it into a cold graphite mould, and we ended up with an amorphous LPO, (Figure 4.6). However, upon reheating it to 400 °C and cooling down slowly, it reverted back to the crystalline pattern obtained.

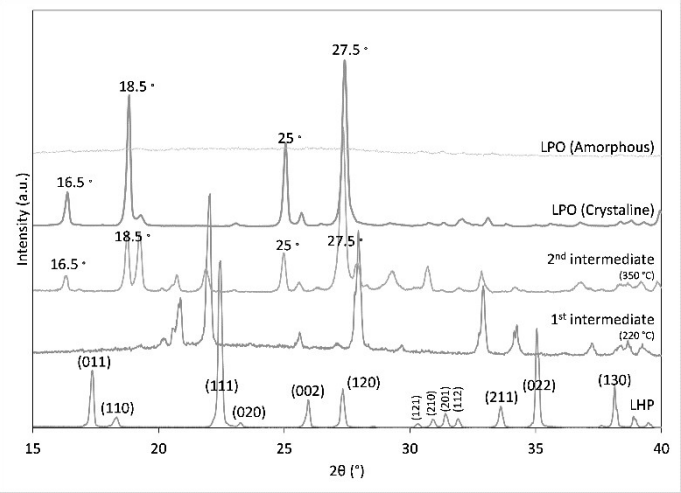

Figure 4.6 X-ray diffractograms of LHP, 1st intermediate (220 °C, L2.5-rich), 2nd intermediate (350 °C, LPO-rich with oligomers), and LPO (crystalline and amorphous)

Raman spectra of the LHP, 1st, and 2nd intermediates and LPO (crystalline) were measured at room temperature in the wavenumber range of 100 to 2000 cm^{-1} (Figure 4.7). For LHP we have signals related to vibrational modes in the low range (under 500 cm^{-1}) and high range (700 to 1200 cm^{-1}). As opposed to all other MH_2PO_4 (M= K, Cs, Rb, Tl, NH_4) molecules whose crystal structure is composed of M^+ and $H_2PO_4^-$, the crystal structure of LHP consists of LiO_4^+ and $H_2PO_4^-$ that share the four oxygen atoms. The low vibrational modes under 300 cm^{-1} correspond to the external

vibrational modes of the PO_4 tetrahedra and LiO_4 tetrahedra. However, the internal modes of LiO_4 tetrahedra showed up around 390 to 500 cm^{-1}. The peaks around 900 and 1080 cm^{-1} correspond to the internal vibrational modes of PO_4 tetrahedra (K.-S. Lee, Ko, Moon, Lee, & Jeon, 2008a). In the case of the 1st intermediate, the characteristic peaks of PO_4 at 900 and 1080 cm^{-1} disappear. Also, there is no sign of the peaks at 1180 and 1220 cm^{-1} which represent the formation of metaphosphate PO_3. These two peaks appear in the 2nd intermediate owing to the presence of LPO.

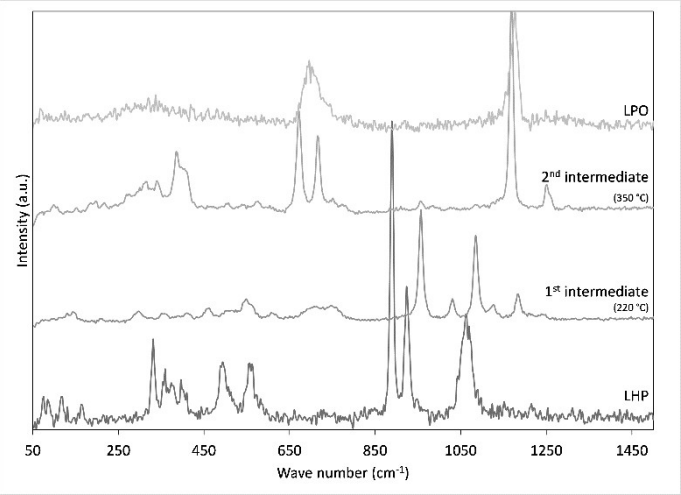

Figure 4.7 Raman spectrogram of LHP, 1st intermediate (220 °C, L2.5-rich), 2nd intermediate (350 °C, LPO-rich with oligomers), and LPO (crystalline).

The TGA, DTG, DSC during the thermal treatment of LHP, as well as XRD and Raman characterization of the main stable compounds/intermediates indicate that LHP decomposes to form LPO in a stepwise manner with L2.5 as the main stable reaction intermediate, and L3 and L4 as metastable intermediates. L2 which had been identified by previous authors as a stable intermediate up to 240 °C was not observed as either a stable or metastable intermediate. A 2nd stable intermediate, with stability range between 290–360 °C exists. The composition of this intermediate is that of LPO with a small content of a higher oligomer ($y \geq 3$) leading to conversion extent α between 0.93 and 0.98. The fraction of oligomers appears to differ with the thermal process. When generating the second intermediate, starting from LHP (isothermal curve at 350

°C) (Figure 4.3b), the composition is richer in LPO (higher α) compared to the same isothermal curve when starting from the first intermediate (Figure 4.4c). In all cases, pure LPO is obtained as a solid material at temperatures > 380 °C; ideally 400 °C, to reduce the processing time.

In summary, the thermal decomposition of LHP to LPO passes through stepwise dehydration reactions which results in sequential oligomer intermediates of LHP. 4 potential intermediates were considered based on our TGA, DTG and DSC results as L2, L2.5, L3 and L4, and transition points. Based on the isothermal TGA, only two relatively stable intermediates were isolated. They were produced at constant temperatures of 220 °C and 350 °C and characterized using XRD and Raman spectroscopy. This agrees with previous studies that have briefly speculated the possibility of the existence of oligomer intermediates in the dehydration of LHP to LPO or roughly considered one intermediate as L2 (Kowalska & Kowalski, 1962; Kowalska, Kowalski, & Truszkowski, 1963; Kowalski et al., 1987; K.-S. Lee, 1996; K.-S. Lee, Moon, et al., 2008). Our findings suggest that rather than L2, the most reaction intermediate is a compound with a slightly higher degree of decomposition (α = 0.6) than that of L2 (α = 0.5) which we have considered to be $Li_5H_4P_5O_{17}$ (or an equivalent $Li_{2.5}H_2P_{2.5}O_{8.5}$, L2.5). This intermediate could be preferentially formed at between 200 and 240 °C but preferentially 220 °C. The stable intermediate obtained at 350 °C is, however, a mixture of LPO with a degree of residual oligomers present (α between 0.93 and 0.97). The amount of residual oligomer is a function of the treatment, and possibly its nature is a function of the thermal profile the sample was subjected to. In all cases, at 400 °C, pure LPO is obtained.

4.4.2 Part 2: Determination of kinetic parameters

In part 1, we determined from isothermal analyses that the decomposition of the LHP to LPO takes place in a stepwise manner with at least 4 reactions steps and the formation of L2.5 as the main reaction intermediate. L3 and L4 were observed as metastable intermediates. In the present section, we attempt to determine the kinetic models and parameters that describe the decomposition reaction steps.

The dehydration of LHP to form LPO is a complex process that involves the formation of many oligomers, in amorphous and crystalline forms, as well as the melting/decomposition of LHP around 200 °C (Thilo & Grunze, 1955). Thilo and Grunze also reported the effect of the gas phase moisture content on the evolution of the reaction, illustrating the reversibility of the dehydration

reactions. Wunderlich suggested that the dehydration of LHP to LPO progressed by a step reaction with random coupling of oligomers up to the point of nucleation, which up to that point would exhibit a Flory–Schulz distribution, followed by a chain-growth process at the surface of the crystals (B Wunderlich, 1968; Bernard Wunderlich, 1990). A similar process is considered by Benkhoucha and Wunderlich, followed by a final annealing step (Benkhoucha & Wunderlich, 1978). They noted that the dimer concentration exceeded that which would be expected of a random step reaction (Flory–Schulz distribution). When fitting their data, they considered that the reaction rate constant for the formation of the dimers differed from that for the formation of the higher oligomers. They also estimated that the critical oligomer length involved in the nucleation ranged from 18 to 15 for the temperature range between 275 and 300 °C. In all cases the decomposition of the LHP begins around 145-150 °C in the solid state but accelerates when approaching the melting point. Given the complexity of the reaction steps involved, the kinetic fitting efforts often lump multiple phenomena into a unique equation which can lead to challenges when transferring to other sets of data or process scales. In the above-mentioned efforts, the particle size, particle size distribution, and in some cases even the sample size and mass are not clearly stated, and these factors are key to describe the thermal and mass transfer limitation that also adds a level of complexity that extends beyond the reaction fundamentals. Furthermore, the data was often obtained for either long term isotherms, which may reflect thermodynamics aspects rather than the kinetic and may alter the perceptions of how the reaction evolves within a limited time frame. In these cases, the data from single rate TGA/DTG are considered and do not allow to put in perspective transfer effects. Here we also lump the different phenomena happening simultaneously. However, we try to use different heating rates and particle sizes to obtain more intrinsic kinetic parameters.

4.4.2.1 Activation energy

Non-isothermal TGA analyses were performed on ground LHP with constant heating rates of 1, 3, 5, 7, 10, 15, 20, 25, and 30 °C/min. The mass loss data was converted into overall conversion extent (α) considering the mass after drying the sample for 10 minutes at 110 °C as being that of pure and dry LHP and the expected mass of LPO determined therefrom. The activation energy vs. α was extracted from the data using the model-free isoconversational methods. For every temperature rate, the temperature corresponding to the values of α from 0.01 up to 0.95 in 0.01 increments was

extracted from interpolation using local fitting of the α vs. T data around the target α value. The activation energy for a given α was then determined by integral isoconversional methods using either the approximations of Ozawa-Flynn-Wall (OFW),(Koga, 2013; Ozawa, 1965) Kissinger-Akahira-Sunose (KAS),(Kissinger, 1957) Starink,(Starink, 2003) or the minimization method proposed by Vyazovkin (Vyazovkin & Dollimore, 1996). All 4 approximations lead to Ea/R values that follow the same trends and differ by about ±1% at most with OFW being the one with the greatest deviation, the other three lying within 0.1% (Figure 4.8).

Figure 4.8 presents 2 sets of activation energies derived from limited ramp rates ranges. The activation energy profile obtained for both sets differs notably by the pattern and amplitude. A critical examination of the results obtained at ramps rates < 5 °C/min were eventually discredited as their results were considerably affected by particle growth and shape transformations that occurs at the approach and at the melting point of LHP (around 200 °C). At ramp rates > 5 °C/min, sintering of the ground LHP and melting is limited and more consistent.

The Ea/R curves obtained for the 25-75 µm class of LHP particle show four main plateaus/regions (Figure 4.8b) that we try to parallel with the various steps observed by DTG data (Figure 4.1b). The first plateau ranges up to conversion extent α of 0.15 and corresponds to the first DTG peak 1 attributed to the surface reaction; the second plateau covers α between 0.15 and 0.3 and only covers a part of the second DTG peak. The identified DTG peak 2 (Figure 4.1a) is only completely covered when including the third plateau, which extends from 0.38 up to 0.68. Beyond α of 0.70, the activation energy decreases continuously with no obvious plateau; this region covers the third DTG peak. Having limited the analysis to α of 0.95, DTG peak 4 which we considered to be due to the dehydration of higher-level oligomers is not captured here.

The fact that the second step is described by two Eα/R plateaus suggests a more complex reaction scheme than initially believed with perhaps multiple steps involved. For all the ramp rates considered, the temperature when α reaches 0.17-0.2 is around 200 °C, close to the melting point of LHP. We thus consider that the second plateau describes the dehydration of molten surface LHP and coincides with peak 2 (only the peak) in the DTG, while the third plateau describes the dehydration of molten LHP in bulk (corresponding to the tail of peak 2 in the DTG curves from 210-270 °C in Figure 4.1a). The continuous decrease of the activation energy beyond α of 0.70 is also not trivial and may present more complex reaction steps.

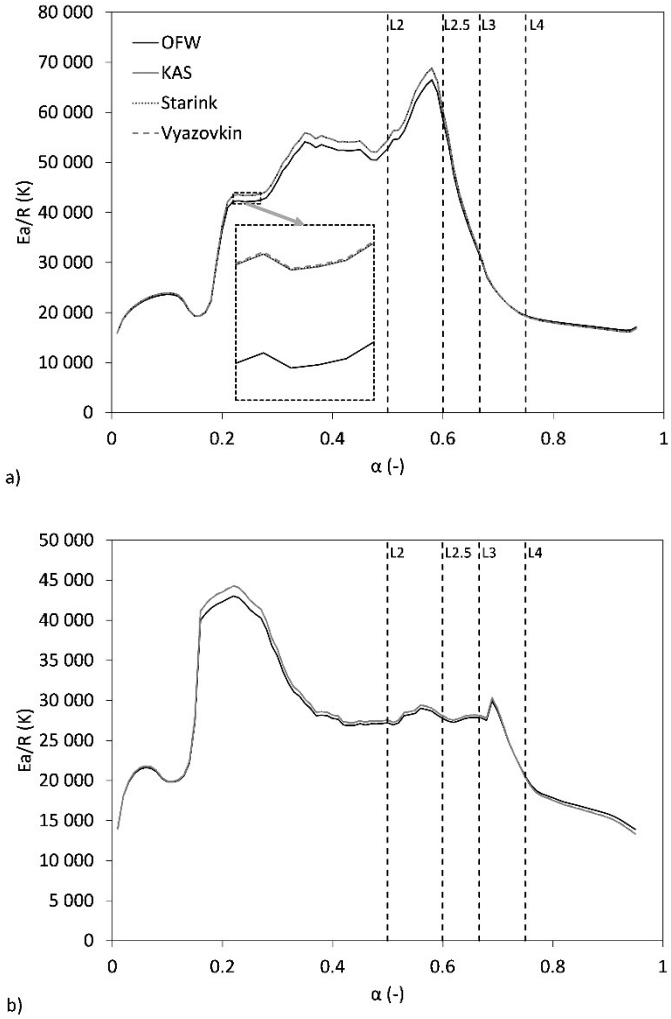

Figure 4.8 Activation energy estimation from model-free iso-conversional integral methods for LHP 25-75 μm as starting material. (a) For ramp rates < 10 °C/min; (b) ramp rates ≥ 5 °C/min

4.4.2.2 Reaction mechanism and kinetic parameter estimation

The starting kinetic mechanism consisted of 4 reaction steps covering peaks 1-3 from the DTG plots and considering that the second peak and tail was described by 2 reaction steps as derived from the activation energy analysis. As we fitted the kinetic parameter for the model, we

introduced additional reaction steps to account for the discrepancies and improve the model predictions. In what follows, we present the final model retained.

The model fitting procedure consisted of defining for each reaction a model (Table 4.1) and activation energy. Estimates of the pre-exponential factor for each reaction step, a transition temperature between reaction steps 1 and 2, and a mass fraction of surface to bulk were proposed. For each set of defined model parameters, the estimated parameters were optimized by Matlab following a Nelder-Mead error minimization algorithm. The error was obtained by solving the kinetic model for each ramp rate from 110°C up to the time (or temperature) where the experimental α reached 0.95 and integrating the absolute difference between the experimental values and the model prediction along the experimental α. The procedures were repeated for different sets of defined model parameters and the data collated. The collated data was used to derive trends as to the best combination of reaction models and activation energy ranges. Decoupling the Ea and A optimization in this way prevents runoffs when values of Ea and A subject to the same optimization loop can deviate without converging because both acting on the same reaction compensate each other's effect.

The final model proposed comprises of 6 reaction steps as follows:

- Reaction 1a: $LHP_{(surf,s)}$ => 2/5 $L2.5_{(s)}$ + 3/5 $H2O_{(g)}$
- Reaction 1b: $LHP_{(surf,l)}$ => 2/5 $L2.5_{(s)}$ + 3/5 $H2O_{(g)}$
- Reaction 2: $LHP_{(bulk)}$ => 2/5 $L2.5_{(s)}$ + 3/5 $H2O_{(g)}$
- Reaction 3: $L2.5_{(s)}$ => 5/6 $L3_{(s)}$ + 1/6 $H2O_{(g)}$
- Reaction 4: $L3_{(s)}$ => 3/4 $L4_{(s)}$ + 1/4 $H2O_{(g)}$
- Reaction 5: $L4_{(s)}$ => 4 $LPO_{(s)}$ + $H2O_{(g)}$

where steps 1a, 1b and 2 represent the conversion of LHP to L2.5, respectively from the solid surface, liquid surface and bulk. The surface (1a and 1b) and bulk (2) reactions were allowed to progress in parallel. The solid surface (1a) and liquid surface (1b) were switched based on reaching a transition temperature criterion. The other reaction steps (3-5) were sequential and consisted of the conversion of L2.5 to LPO.

The conversion extent for each reaction is given by considering the fractional amount of material that converted according to this reaction.

$$\alpha_1 = \alpha_{LHP,surf} = 1 - n_{LHP,surf} \Big/ \left(n_{LHP,0} \cdot x_{surf} \right) \tag{4.5a}$$

$$\alpha_2 = \alpha_{LHP,bulk} = 1 - n_{LHP,bulk} \Big/ \left[n_{LHP,0} \left(1 - x_{surf} \right) \right] \tag{4.5b}$$

$$\alpha_3 = \alpha_{L2.5} = \left(3 \cdot n_{L3} + 4 \cdot n_{L4} + n_{LPO} \right) \Big/ n_{LHP,0} \tag{4.5c}$$

$$\alpha_4 = \alpha_{L3} = \left(4 \cdot n_{L4} + n_{LPO} \right) \Big/ n_{LHP,0} \tag{4.5d}$$

$$\alpha_5 = \alpha_{L4} = n_{LPO} \Big/ n_{LHP,0} \tag{4.5e}$$

$$\alpha = n_{H2O} \Big/ n_{LHP,0} \tag{4.5f}$$

x_{surf} is the fraction of the starting LHP that belongs to the surface and reacts according to reactions 1 and 2. The value of x_{surf} is a property of the particle class and will be determined as part of the optimization process. Only one of Reaction 1a or 1b can take place at a time, depending on the temperature is greater than a transition temperature around 200°C. The transition temperature is determined as part of the optimization process.

The typical reaction rate equation and ordinary differential equations for mole and temperature are given by

$$r_{i,k} = w\left(\alpha_{i-1} \right) n_{LHP,0} A_i \exp\left(-\frac{E_{a,i}}{RT_k} \right) f\left(\alpha_i \right) \tag{4.6}$$

$$\frac{dn_{j,k}}{dt} = \sum_i \left(\nu_{i,j} r_{i,k} \right) \tag{4.7a}$$

$$\frac{dT_k}{dt} = \beta_k \tag{4.7b}$$

where indices i, j and k represent the reactions, species and ramp rates respectively. $n_{LHP,0}$ is a sample size scaling parameter corresponding to the initial moles of LHP. $w(\alpha_{i-1})$ is a weighting function based on the smoother step function (for α_{i-1} between 0.85 and 0.95; when $\alpha_{i-1} \leq 0.85$ w =

0; when $\alpha_{i-1} \geq 0.95$ w = 1) to activate a reaction step only when the previous reaction step approaches completion (Ebert, Musgrave, Peachey, Perlin, & Worley, 2003). This applies to reaction steps 3 to 5. For reaction step 3, the average of α_1 and α_2 weighted according to their starting molar ratios is used. This smooth step function allows the reactions to occur successively without having to implement thermodynamic reversibility considerations that would greatly exceed the motivations of the present work. f is the model-dependent function. The data collected in the isotherm trials generally exhibit a deceleratory behaviour which will likely be best described by models belonging to the F, D, or R groups of reaction models (Table 4.1).

For each temperature ramp rate, the resolution of the ODE system is performed with convergence at every for the times (temperature) where the isoconversional data was obtained, e.g., corresponding the range of α from 0 to 0.95 in increments of 0.01). The initial temperature is considered to be 110°C following the drying phase of the ramps. The average error is then computed as

$$Err = \frac{1}{n_k} \sum_k \int_{\alpha_{exp}=0}^{0.95} \left| \alpha_{exp,k} - \alpha_{\mathrm{mod},k} \right| d\alpha \tag{4.8}$$

4.4.2.3 Fitting procedure

The kinetic model optimization was performed in a series of 4 steps to progressively limit the search breadth.

In the first step, the activation energies determined from Figure 4.8a were used. At this stage, we considered that all reaction steps were described using a D3 model (3-dimensional diffusional model). With the assumed models and activation energies, the fraction of surface, the temperature transition between reaction 1a and 1b and the pre-exponential terms were determined by minimizing the computed error. The initialization of the fitted parameters is key, and this step was largely performed with manual intervention until a sensible set of parameters was found.

As a second step, the reaction models are optimized in a more systematic manner. Since the reactions considered mostly occur sequentially, we opted to optimize the model selection by adding one reaction step at a time starting from reaction step 1a. The initial estimate of the pre-exponential factor of the reaction whose model was being investigated was rescaled relative to the ratio of the

average f(α) over the range 0.1 to 0.9 (Table 4.1). For each reaction, the optimal model is thus determined and used for the optimization of the subsequent reaction models. When expanding to the next reaction steps, the previous steps' parameters were investigated again in order to account for compensation effects from the other reactions. At the end of the optimization procedure, the best models for every reaction are ranked. Typically, up to 4 reaction models were retained for each reaction steps.

The third step consisted of performing the optimization on the various combinations extracted from the best reaction models (typically the 3 top) for each reaction step to determine the best combinations of models.

The fourth step consisted of varying the activation energies for each reaction in order to determine the most suitable set of conditions while allowing a reduced set of model combinations to be tested. This step is performed using a Monte Carlo approach during which the activation energy of each reaction is independently varied using a normal distribution centred on the original activation energies and the model combination selected using a flat random number. Here the initial estimates of the pre-exponential factor are initially adjusted considering Equation 9, where $\overline{T_i}$ is an average temperature initially estimated graphically as a mid-range temperature for each reaction step, after collating a with sufficient number of calculation for a given reaction step with the same reaction model, and various activation energies, the a more accurate $\overline{T_i}$ is determined from fitting the results. Likewise, after performing a sufficient number of optimizations for various reaction models, their $\overline{f}$ on A were updated. The fourth step performed typically on 50 sets of reaction models and activations energies. For each set, the error minimization procedure provides the best-fitted values and the error. The results from the 50 sets are collated and ranked. The error distributions with respect to model selection and activation energies are examined to determine trends. According to the findings, models are progressively dropped from consideration, and the activation energy windows moved as necessary to identify an optimum set of parameters. From the collated results, average $\overline{T_i}$ and $\overline{f}$ are updated considering the new results. The fourth step is repeated as often as needed until a satisfactory set of model parameters are determined.

$$A_{i,new} = A_{i,ref} \frac{\overline{f}_{i,ref}}{\overline{f}_{i,new}} \exp\left(\frac{Ea_{i,new} - Ea_{i,ref}}{R\overline{T}_i} \right) \tag{4.9}$$

Table 4.1 Description of deceleratory reaction models considered

Model	$f(\alpha)$	$\lim_{\alpha \to 0} f(\alpha)$	$\overline{f_{0.1-0.9}} = \frac{\int_{0.1}^{0.9} f(\alpha) d\alpha}{0.8}$	Final $\overline{f}$ from fitted results
F1	1-α		0.5	0.5
F2	$(1-\alpha)^2$		0.303	0.229
F3	$(1-\alpha)^3$		0.205	0.133
D1	$1/(2\alpha)$		1.373	1.303
D2	$\frac{-1}{\ln(1-\alpha)}$	1/α	2.179	1.634
D3	$\frac{3(1-\alpha)^{2/3}}{2[1-(1-\alpha)^{2/3}]}$	9/(2α)	7.935	3.807
D4	$\frac{3}{2[(1-\alpha)^{-1/3}-1]}$	9/(2α)	9.091	5.135
R1	$1.5(1-\alpha)^{1/3}$		1.157	1.303
R2	$2(1-\alpha)^{1/2}$		1.370	1.590
R3	$3(1-\alpha)^{2/3}$		1.839	2.128

Where specified, the simplified approximation of f(α) for small α is used when $\alpha < 10^{-6}$ to minimize numerical truncation errors in evaluating the original equation; also, to avoid division by 0, the values of α are forced greater than 10^{-40}; this lower limit does not introduce notable deviations when using the f(α) to numerically calculate g(α) vs. the algebraic g(α).

4.4.2.4 Fitting results

The optimal reaction models, the best parameters, and key results are reported in Table 4.2. The proposed model explains 99.8% of the variability (R^2).

Table 4.2 Summary of the optimum parameters as fitted

Reaction step	Optimal Ea/R (K), (range)	A (min^{-1})	Reaction model (other)	$\overline{T}_i$ (K)
1a	27727 (20000–30000)	9.252×10^{23}	D2	460.7
1b	41168 (37000–45000)	1.481×10^{35}	D3	489.8
2	22856 (20500–24500)	1.943×10^{18}	F2	534.6
3	37710 (27000–39000)	3.243×10^{26}	D4 (D3, D2, D1)	571.4
4	19452 (17500–21000)	7.228×10^{13}	F2	599.3
5	6400 (5300–10000)	623.2	D4 (D3)	661.6

The fitted x_{surf} is 0.565, which is reasonable when we examine the range conversion extent α between the second and third activation energy plateaus in Figure 4.8b and the conversion extent expected for L2.5 (0.35/0.6 = 0.58). The fitted transition temperature between reaction 1a and 1b is 473.9K, is close to the melting of LHP.

The Ea/R range describes the range of activation energy values; each reaction step could have while not increasing the fit error by more than 5% (relative). For reactions steps 1a, 3 and 5 this range is wide implying that the activation energy is less sensitive to the model performance, while for steps 1b, 2 and 4 it is rather narrow and not always centred on the optimal value. The values of the optimal activation energies for every reaction steps are generally in agreement with the trends that were derived from the isoconversional analyses to within 20%. The activations energies for reaction steps 1a and 2 appear inverted, but when we attempt to have both of them closer to the isoconversional results, the prediction error increases. The activation energies for reaction steps 2 and 3 are within 5% of those from the isoconversional analysis. For reaction steps 4 and 5, where the isoconversional results exhibit a continuous decline, the activation energy fitted are somewhat at the lower end of the isoconversional activation energy for reaction step 4 and about half of the one at the end of reaction step 5. Attempts to describe these reaction steps with a modified Arrhenius equation ($r_{i,k} = w(\alpha_{i-1}) n_{LHP,0} A_i T_k^{\gamma} \exp(-E_{a,i}/RT_k) f(\alpha_i)$) did not provide appreciable improvement.

The reaction model determined from the optimization procedure gives an indication of the way the specific reaction steps evolve. However, this requires caution as each reaction step may involve multiple "sub-steps," making it more complex than what is accounted by the models (M. E. Brown, 2005). Here we see that reaction 1a, 1b, 3 and 5 present diffusive type evolutions. In the case of reaction steps 3 and 5, despite being better fitted with a D4 model, the fit error would not have increased by more than 5% for alternate diffusive models (Table 4.2). While reaction steps 1b, 3 and 5 are better fitted by D3 and D4 models which are 3-dimensional diffusion models associated with spherical particles, reaction step 1a is better fitted by a 2-dimensional diffusion model. This 2D is generally attributed to the diffusion along the radius of a cylinder shape (Khawam & Flanagan, 2006). However, our SEM observation of the LHP expected to react during reaction step 1a does not suggest the presence of such cylindrical shapes but rather spherical shapes. As for reaction steps 2 and 4, they are better described with a F2 model which would suggest that the rate-limiting sub-step involves the combination of 2 reactant molecules.

The values of $\overline{T}_i$, which relates the way the Ea_i and A_i vary relative to one another, are within the temperature range at which these steps take place. If an interested party wanted to modify the

activation energy to reflect the isoconversional data more closely, the A_i values should be modified according to Equation 9.

The conversion from the model is compared against the experimental conversion for the constant rate trials which were used to fit the model (Figure 4.9). As can be observed, the conversion predictions are in good agreement with the experimental data. A closer examination of the error distribution with α (in b) shows that the error is generally lower than ± 0.025 for ramp rates ≥ 5 °C/min. The average error achieved for the model is 0.0085. The data for 30 °C/min shows the greatest deviation for α ranging from 0.15 to 0.3, where the model under predicts the conversion experimentally achieved and the opposite trend for the lower ramp rates. This could be due to the particle sintering effect that affects the ramp rates differently, being lumped into the kinetic model. More severe sintering observations previously made for the 1 and 3 °C/min ramp rates led to their exclusion from the kinetic determination effort. Also, we note that the difference between the model and experimental conversion extents exhibit several waves occurring around the conversion extents 0.15, 0.35, 0.45, 0.68, and 0.75. These are the results of the transitions from one reaction step to another.

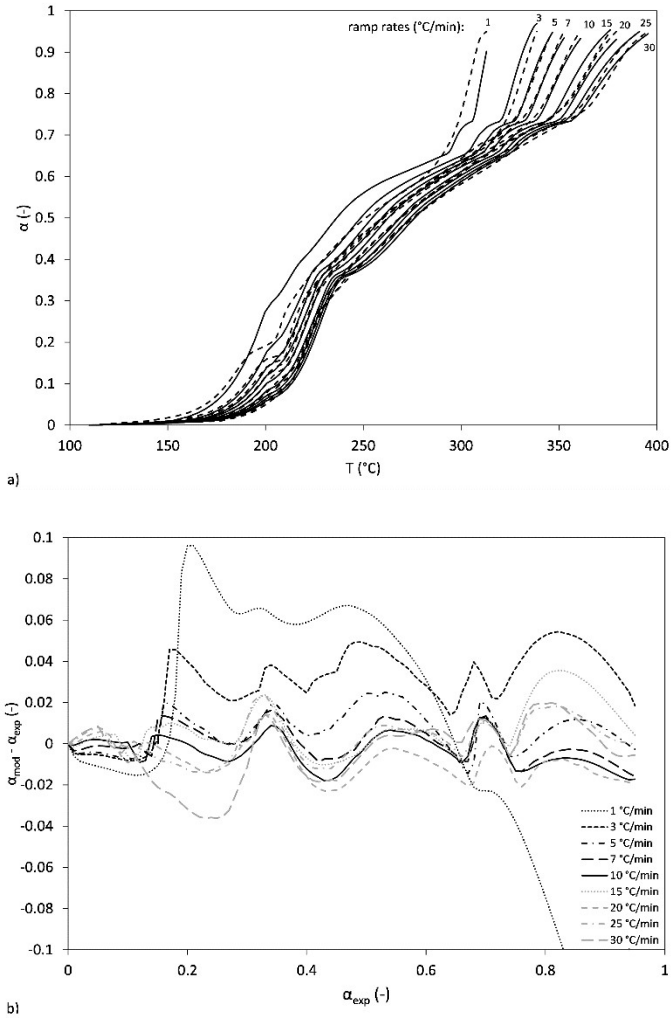

Figure 4.9 Comparison between the experimental and fitted model prediction starting with LHP 25-75 µm with ramp rates between 1 and 30 °C/min. (a) conversion extent vs. temperature (Solid lines: model prediction; dotted lines: experimental data); (b) difference between the model predicted and experimental conversion extent. Only the data for ramp rates ≥ 5 °C/min was used for model fitting

4.4.2.5 Performance of the proposed kinetic model

The kinetic model predictions for isothermal conditions are not as good as those for the constant ramp conditions. When we examine the prediction for the isotherms achieved between 180°C and 280°C, important discrepancies become evident (Figure 4.10a). For the isotherms below 200°C,

the model predicts much more conversion than obtained experimentally. The predicted conversion for the 180°C isotherm predicts near-complete conversion of the surface LHP within 15 hours, while the experimental data is only a third of that. The kinetic rate attributed to reaction step 1a would need to be reduced by a factor 100 for it to explain such low conversions, a reduced rate that is incompatible with the findings from the isoconversional data. This is the result of significant sintering that takes experimentally, which reduces the mass transfer, which is not accounted for in the model. Observation of the sample from the 180 °C isotherm after 15 hours clearly shows that the materials have shrunk to form coarse lumps with low porosity. For 200 to 220 °C, the model prediction improves. The agreement is good with respect to the final conversion extent; however, the model predicts a faster rate of reaction in the initial stages, which is surprising considering the agreement that was observed in Figure 4.9. One possible explanation for this is the sample size. The model was fitted using data on 5 mg samples, while the isotherms were performed on 15 mg samples as exposed in Figure 4.4d. The difference in sample size appears to introduce some mass transfer limitations which lower the conversion rate. At 240 and 260 °C, the model predicts a more stable conversion around the L2.5 conversion with the conversion of L2.5 to L3 (reaction step 3) only partly occurring, while the experimental data shows clearly that the conversion reaches levels beyond the conversion to L4 equivalent. On the contrary at 280 °C, the model reaches the L3 conversion extent in good agreement with the experimental data up to that point ($\alpha = 0.67$) but beyond this conversion extent, when the reaction is allowed to convert according to reaction steps 4 and 5, the model predictions greatly exceed those of the experimental data. This shortcoming of the model persists at higher temperature up to about 360 °C where the experimental reaction rate becomes high enough to reach levels comparable to those predicted by the model at conversion extent greater than 0.75 (Figure 4.10b). In contrast, when starting with the re-ground 1st intermediate, the model prediction underpredict the reaction rate that is achieved experimentally (Figure 4.10c). This supports the hypothesis that some of the model shortcomings presented here are due to the effect related to sintering and mass transfer limitation. The rate transition predicted by the model at conversion extent approaching 0.75 is not observed experimentally. Also, since not accounted for, the model does not predict the plateaus around the conversion extent 0.93 that are experimentally observed and associated with the formation of high-level oligomers.

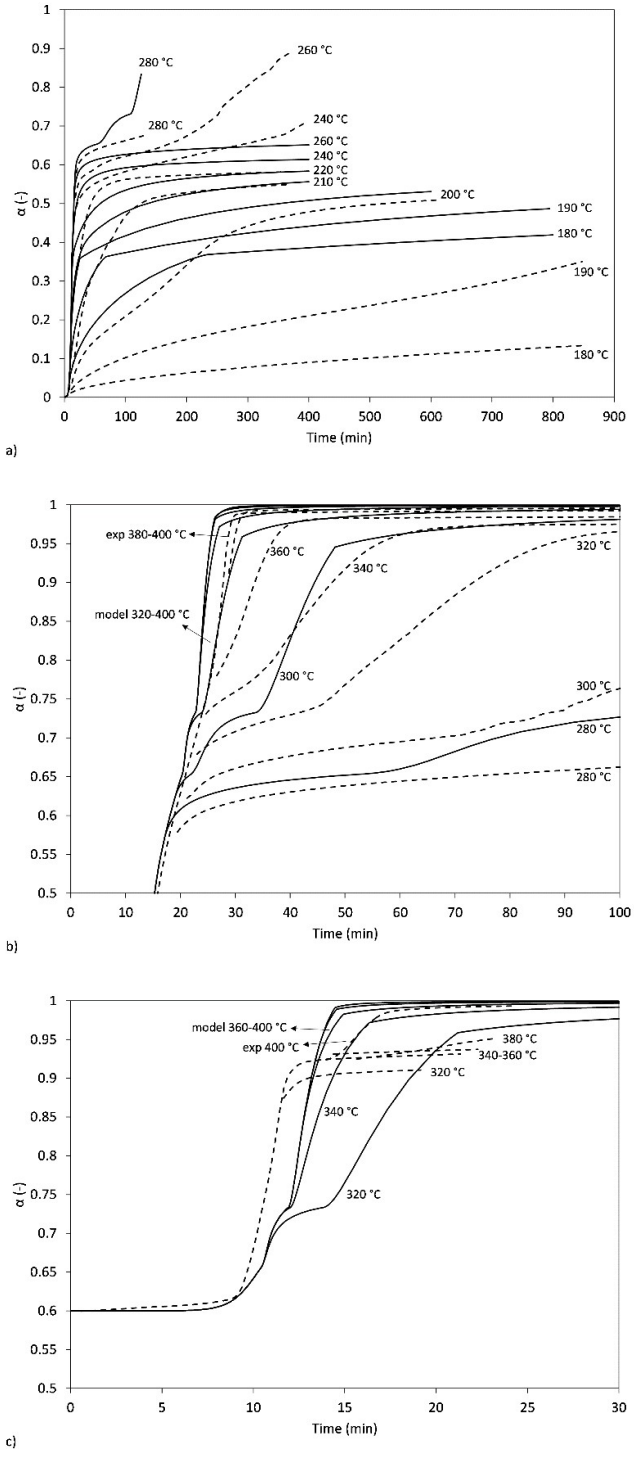

Figure 4.10 Model performance under isothermal conditions. (a) 25-75 µm LHP at 180-280 °C isotherms, (b) 25-75 µm LHP at 280-400 °C; (c) 25-75 µm reground 1st intermediate (220°C) at 320-400 °C. Solid lines: model prediction; dotted lines: experimental data

The proposed kinetic model is suitable for prediction of test conditions where the time spent in the 180-200°C range is low, corresponding to effective ramp rate in that temperature range greater than 5°C/min. We expect from other isotherm observations that no significant sintering should occur outside of this temperature window and that as a result, the kinetic model should extrapolate to lower ramp rates. Isotherm of a few hours should be predicted adequately as long as they take place above 240°C where the stable intermediate L2.5 decomposes.

4.5 Conclusion

The isoconversional study of the activation energies along with other DTG results and visual observations led us to initially propose a four-step reaction mechanism. The optimization and parameter fitting procedure and considerations from the isothermal TGA led us to expand the model to 6 reaction steps. The first 3 steps correspond to the conversion of LHP to L2.5 from the solid surface, liquid surface, and bulk, which have different rates due to the difference in diffusion. The kinetic model and parameters that describe the decomposition reaction steps were fitted assuming different kinetic models and considering as starting points the activation energies from isoconversional methods. The proposed model was in good agreement with the constant ramp rate experimental data with limitations when the ramp rate was lower than 5 °C/min. These limitations arise from the sintering and/or shape change that occurs near the melting temperature of LHP (200 °C). Another limitation comes from the unaccounted reversibility of some of the reaction steps. Thus, with isothermal processes, the model tends to over-predict the conversion when approaching the composition of important reaction intermediates (e.g., L2.5, L3, and L4).

For the practical purpose of this study which is to predict reaction rate of the dehydration of LHP in semi industrial-scale reaction vessel with constant heating rates, the findings of this study can serve well as a guide for the design and operation. Future work on the decomposition of the LHP to LPO will need to address the issues related to the starting particle size and sample amounts which add mass transfer limitations. Also, as larger-scale production of LPO based on the decomposition of LHP would lend itself to direct heating of the material with flue gas, the effect of the gas moisture content on the reversibility of the decomposition steps will need to be examined

and the models updated. Similar kinetic studies are also recommended for other alkali metal dihydrogenphosphate salts like sodium and potassium.

Abbreviations and notation

A Reaction frequency factor, pre-exponential term in Arrhenius formulation (min^{-1})

CCD Charge-coupled device

DSC Differential scanning calorimetry

DTG Derivative thermogravimetry

Ea activation energy (J/mol)

Err model prediction error (-)

f(α) reaction model function (-)

g(α) integral form of the reaction model function (-)

ICTAC International Confederation for Thermal Analysis and Calorimetry

LEI Low secondary electron image

LFP Lithium iron phosphate, $LiFePO_4$

LHP Lithium dihydrogen phosphate, LiH_2PO_4

LPO Lithium metaphosphate, $LiPO_3$

L2 Lithium pyrophosphate, $Li_2H_2P_2O_7$

L2.5 $Li_{2.5}H_2P_{2.5}O_{8.5}$ (equivalent to ½ $Li_5H_4P_5O_{17}$)

L3 $Li_3H_2P_3O_{10}$

L4 $Li_4H_2P_4O_{13}$

M generic alkali metal cation (and ammonia) defined for some chemical formulations (M can be: Li, Na, K, Rb, Cs, and NH_4)

MAP monoammonium phosphate, $NH_4H_2PO_4$

n moles of various species (mol)

n_k number of ramp rate trials considered in the analysis

P_{O_2} the partial pressure of Oxygen

P2/m Primitive monoclinic Bravais-lattice space group

r reaction rate (mol/min)

R gas constant (J/mol·K)

SEM Scanning electron microscopy

t time (min)

T temperature (°C or K as indicated)

TGA Thermogravimetric analysis

x_{surf} fraction of the starting LHP that is considered to belong to the surface, the balance belonging to the bulk (-)

w weighing function that varies between 0 and 1 and activates a specific reaction step based on the completion status of the previous reaction, this ensures that the reactions are sequential without having to introduce reversibility

XRD X-ray diffraction

y number of PO3 repeat units in the oligomer (as per Equation 1)

Z number of chemical formula units per unit cell

Greek letters

α global conversion extent for the reaction LHP to LPO based on the mass loss (-)

β ramp rate (°C/min)

ν molar reaction coefficients of species (reactant < 0; product > 0; non-involved = 0)

indices

0 initial

exp experimental

i reaction steps

j chemical species (LHP, L2.5, L3, L4, LPO, H_2O)

k ramp rates

mod model

new new condition (as opposed to reference condition)

ref reference condition

surf surface

Acknowledgements

This work was made possible by the financial support of the Natural Sciences and Engineering Research Council of Canada (NSERC) and the Canada Foundation for Innovation (CFI) through the Automotive Partnership Canada program. The authors are also appreciative for the financial and technical support from industrial partner Johnson Matthey Battery Materials. The authors would also like to thank Ms. Nooshin Saadatkhah for producing LHP particles used in some of the trials.

4.6 References

1. Padhi, A.K., K.S. Nanjundaswamy, and J.B. Goodenough, *Phospho-olivines as positive-electrode materials for rechargeable lithium batteries.* Journal of the electrochemical society, 1997. **144**(4): p. 1188-1194.
2. Gauthier, L., et al., *Process for preparing electroactive insertion compounds and electrode materials obtained therefrom*. 2009, Google Patents.
3. Talebi-Esfandarani, M., et al., *The Use of Reduced Cost and Purity Precursors in the Melt Preparation of LiFePO4.* Meeting Abstracts, 2015(6): p. 492-492.
4. Talebi-Esfandarani, M., et al., *LiFePO4 synthesized via melt synthesis using low-cost iron precursors.* Journal of Solid State Electrochemistry, 2016. **20**(7): p. 1821-1829.
5. Kowalski, Z., et al., *Manufacture of sodium dihydrogen pyrophosphate*. 1987, Zaklady Chemiczne "Alwernia", Pol. . p. 2 pp.
6. Prakash, S., et al., *Advanced Inorganic Chemistry, Volume 1; 17th Edition*. 2000: S. Chand & Co. Ltd. 1156 pp.

7. Angaiah, S., et al., *Process for the preparation of lithium metaphosphate*. 2003, Google Patents.
8. Brown, M., D. Dollimore, and A. Galwey, *Reactions in the Solid State, vol. 22 of Comprehensive Chemical Kinetics, Bamford, CH and Tipper, CFH, Eds*. 1980, Amsterdam: Elsevier.
9. Osterheld, R. and M. Markowitz, *Polymerization and depolymerization phenomena in phosphate–metaphosphate systems at higher temperatures. IV. Condensation reactions of alkali metal hydrogen phosphates.* The Journal of Physical Chemistry, 1956. **60**(7): p. 863-867.
10. Gallagher, P., *A study of the thermal decomposition of some alkali metal dihydrogen phosphates and arsenates.* Thermochimica Acta, 1976. **14**(1): p. 131-139.
11. Blinc, R., et al., *High-Temperature Phase Transition in RbH2PO4.* The Journal of Chemical Physics, 1969. **50**(12): p. 5408-5411.
12. Pechkovskii, V.V., et al., *Use of infrared spectroscopy to study the thermal dehydration of monosubstituted phosphates of magnesium and calcium.* Vestsi Akad. Navuk Belarus. SSR, Ser. Fiz.-Tekh. Navuk, 1968(1): p. 36-40.
13. Bagryantseva, I. and V. Ponomareva, *Proton conductivity and phase composition of mixed salts in the systems MH2PO4–CsHSO4 (M= Cs, K).* Physics of the Solid State, 2016. **58**(8): p. 1651-1658.
14. Martinez, H., et al. *High Temperature Phase Transitions in RbH2PO4*. in *APS Texas Sections Spring Meeting Abstracts*. 2009.
15. Park, J.-H., K.-S. Lee, and B.-C. Choi, *High-temperature transformation in KH2PO4 and RbH2PO4 crystals.* Journal of Physics: Condensed Matter, 2001. **13**(42): p. 9411.
16. Lee, K.-S., et al., *High-temperature phase transformations in LiH 2 PO 4 and possible solid-state polymerization.* Solid State Communications, 2008. **147**(1): p. 74-77.
17. Lee, K.-S., *Hidden nature of the high-temperature phase transitions in crystals of KH 2 PO 4-type: is it a physical change?* Journal of Physics and Chemistry of Solids, 1996. **57**(3): p. 333-342.
18. Abdel-Kader, A., A. Ammar, and S. Saleh, *High-temperature phase transition in potassium dihydrogen phosphate crystals.* Thermochimica acta, 1990. **167**(2): p. 225-233.
19. Brown, M., et al., *Computational aspects of kinetic analysis: part A: the ICTAC kinetics project-data, methods and results.* Thermochimica Acta, 2000. **355**(1): p. 125-143.
20. Burnham, A.K., *Computational aspects of kinetic analysis.: Part D: The ICTAC kinetics project—multi-thermal–history model-fitting methods and their relation to isoconversional methods.* Thermochimica Acta, 2000. **355**(1): p. 165-170.
21. Maciejewski, M., *Computational aspects of kinetic analysis.: Part B: The ICTAC Kinetics Project—the decomposition kinetics of calcium carbonate revisited, or some tips on survival in the kinetic minefield.* Thermochimica Acta, 2000. **355**(1): p. 145-154.

22. Vyazovkin, S., *Computational aspects of kinetic analysis.: Part C. The ICTAC Kinetics Project—the light at the end of the tunnel?* Thermochimica Acta, 2000. **355**(1): p. 155-163.

23. Vyazovkin, S., et al., *ICTAC Kinetics Committee recommendations for performing kinetic computations on thermal analysis data.* Thermochimica Acta, 2011. **520**(1): p. 1-19.

24. Vyazovkin, S., et al., *ICTAC Kinetics Committee recommendations for collecting experimental thermal analysis data for kinetic computations.* Thermochimica Acta, 2014. **590**: p. 1-23.

25. Benkhoucha, R. and B. Wunderlich, *Crystallization during polymerization of Lithium Dihydrogen Phosphate. I. Nucleation of the Macromolecular Crystal from the Oligomer Melt.* Zeitschrift für anorganische und allgemeine Chemie, 1978. **444**(1): p. 256-266.

26. Wunderlich, B., *Thermal Analysis*. 1990, USA: Academic Press Inc.

27. Klaewkla, R., M. Arend, and W.F. Hoelderich, *A review of mass transfer controlling the reaction rate in heterogeneous catalytic systems*, in *Mass Transfer-Advanced Aspects*. 2011, InTech.

28. Thilo, E. and H. Grunze, *Zur Chemie der kondensierten Phosphate und Arsenate. XIII. Der Entwässerungsverlauf der Dihydrogenmonophosphate des Lić, Nać, Kć und NH.* Zeitschrift für anorganische und allgemeine Chemie, 1955. **281**(5-6): p. 262-283.

29. Wunderlich, B., *Crystallization during polymerization*, in *Fortschritte der Hochpolymeren-Forschung*. 1968, Springer. p. 568-619.

30. Lee, K.-S., et al., *Crystal growth and morphology of LiH 2 PO 4.* Materials Chemistry and Physics, 2012. **136**(2): p. 802-808.

31. Murashova, E. and N. Chudinova, *Synthesis and crystal structures of lithium polyphosphates, LiPO 3, Li 4 H (PO 3) 5, and LiMn (PO 3) 3.* Crystallography Reports, 2001. **46**(6): p. 942-947.

32. Lee, K.-S., et al., *Raman spectroscopic study of.* Solid State Communications, 2008. **145**(9): p. 487-492.

33. Kowalska, E. and W. Kowalski, *Influence of temperature on the rate of formation of NaH pyrophosphate from monosodinm orthophosphate.* Przem. Chem., 1962. **41**(No. 2): p. 73-4.

34. Kowalska, E., W. Kowalski, and A. Truszkowski, *Influence of temperature on the formation rate of Na metaphosphate from Na dihydrogen pyrophosphate.* Przem. Chem., 1963. **42**(4-5): p. 212-14.

35. Koga, N., *Ozawa's kinetic method for analyzing thermoanalytical curves.* Journal of thermal analysis and calorimetry, 2013. **113**(3): p. 1527-1541.

36. Ozawa, T., *A new method of analyzing thermogravimetric data.* Bulletin of the chemical society of Japan, 1965. **38**(11): p. 1881-1886.

37. Kissinger, H.E., *Reaction kinetics in differential thermal analysis.* Analytical chemistry, 1957. **29**(11): p. 1702-1706.

38. Starink, M., *The determination of activation energy from linear heating rate experiments: a comparison of the accuracy of isoconversion methods.* Thermochimica Acta, 2003. **404**(1): p. 163-176.

39. Vyazovkin, S. and D. Dollimore, *Linear and nonlinear procedures in isoconversional computations of the activation energy of nonisothermal reactions in solids.* Journal of chemical information and computer sciences, 1996. **36**(1): p. 42-45.

40. Ebert, D.S., et al., *Texturing & modeling: a procedural approach*. 2003: Morgan Kaufmann.

41. Brown, M.E., *Stocktaking in the kinetics cupboard.* Journal of thermal analysis and calorimetry, 2005. **82**(3): p. 665-669.

42. Khawam, A. and D.R. Flanagan, *Solid-state kinetic models: basics and mathematical fundamentals.* The journal of physical chemistry B, 2006. **110**(35): p. 17315-17328.

CHAPTER 5 ARTICLE 2: SIZE SEGREGATION IN A BALL-MILL ROTARY-KILN REACTOR

Bahman Yari, Christine Beaulieu, Pierre Sauriol, François Bertrand, Jamal Chaouki[2]

Department of Chemical Engineering, Polytechnique Montreal, C.P. 6079, Succ. Centre-Ville, Montreal, Quebec H3C 3A7, Canada

Submitted to Powder Technology

5.1 Abstract

Mixing and segregation of media is important in a ball-mill rotary-kiln (BaMRoK) reactor in the presence of reaction, heat and mass transfer. Discrete element method (DEM) and solidified bed sampling were used to study the effect of different size ratios in mixing and segregation of bidisperse spherical beads in a rotating drum. In the experimental part of the research, we used "agar bed-fixing" together with a new sampling technique. When the size ratio between the two components was larger than a transition amount (0.26), the smaller component tended to accumulate in the core region with a maximum core-shell segregation around the size ratio 0.5, whereas in the opposite case (smaller size-ratios), they accumulated near the drum wall, in the passive layer. At ratios around the transition ratio (0.26) and at size ratios approaching unity, the most uniform distribution of smaller component was attained based on the relative standard deviation (RSD).

Keywords: solid mixing, size segregation, granular mixture solidification, powder sampling, Ball Mill-Rotary-Kiln

[2] Corresponding author: jamal.chaouki@polymtl.ca; +1-514-340-4711 x4034

5.2 Introduction

Although historically rotary kilns have mainly been used for lime calcination and cement production, today they are finding applications in different industries for sintering, drying, oxidation, reduction, dehydration and so on. The idea of a rotary kiln with grinding media (BaMRoK) has recently been implemented in laboratory scales for many solid state reactions. However, there are many aspects that should be investigated for its scale-up, such as the mixing and segregation of the balls and the material.

Size based separation of different sized granular materials from their mixtures as a consequence of any physical movement is called size segregation (G. C. Barker & Anita Mehta, 1993; G. C. Barker & A. Mehta, 1993). This phenomenon is very common in applications, including granular flows. This can be desirable in some cases where the separation of different sized granules is aimed (Choi, Hayashi, Endoh, & Sakamoto, 1999; Habib, Miles, Habib, & Hall, 2013; S. Wang, He, Wei, & Xie, 2017). However, in many cases, such as in pharmaceutical powder mixers, food industry blenders, tumbling ball mills (Cleary, 1998, 2009) and rotary kilns (A. A. Boateng, 2015), it is detrimental because of different consequences such as product inhomogeneity or operation disruption.

In a rotary kiln, different sized particles can be segregated mainly through trajectory or percolation mechanisms. In the first mechanism, in some operation modes including slumping, rolling and cataracting, when particles from the passive layer move to the top, they join the active layer by being discharged to the exposed active layer. It has been shown that bigger particles travel faster and further in the active layer, which causes their segregation (Bridgwater, 1976; Bridgwater et al., 1985). In the second mechanism, when the bed of different sized particles is disturbed, they start to rearrange. In this rearrangement, smaller particles have a better chance to fall into a void between bigger particles and go down toward the wall, displacing the bigger particles upward to the opposite direction (S. B. Savage, 1983). This mechanism is responsible for the transverse segregation in a rotating drum. Segregation may significantly influence heat transfer in a rotary kiln, and therefore, it may affect the reaction rate in different zones of the kiln because of an increased radial or axial temperature gradient. This, in turn, may decrease product homogeneity.

One of the key parameters in the efficient operation of tumbling ball mills is energy consumption. This parameter is significantly affected by the mixing and segregation state of the impacting media and the powder. Typical efficiency of a ball mill is 1 to 5%, i.e., only a small amount of supplied energy is used for breaking the particles (Cleary, 1998). This can be improved by a better understanding of the phenomena involved in the milling process. For a regular ball mill with 5 MW total power consumption, a 1% increase in its performance would save 50 kW of energy with other environmental and quality improvements. Segregation is one of the important phenomena that decrease ball mill efficiency. Segregated balls may accumulate in a certain zone say the central parts and do not enter the cataracting stream. Therefore, they cannot break the particles with high energy impacts at the end of the active layer. On the other hand, segregated particles neighbour with same-sized particles that do not have enough impact to break each other. This also results in further efficiency loss.

Segregation and mixing of granular materials have been the center of attention during the last 3 decades. Because of its abundance in different industries, one of the most studied systems in the literature is the rotating drum, operating in the rolling regime. Despite the apparent simplicity of this system, there are still many ambiguities in the granular dynamics of this system. In most part of the last century, there were rarely any studies trying to formulate the dynamics of granular flows. It was only in the last decade that the number of such studies started to increase in both experimental and computational categories with the latter being due to the help of the significant advancements of computer processors.

In the special case of rotating drums, three types of segregation occur in different dimensions of the drum. Radial segregation sets in a few revolutions, while the segregation in axial dimension needs hundreds of revolutions to take place and results in a banding pattern along the axis of the drum (Ebrahim Alizadeh, Francois Bertrand, & Jamal Chaouki, 2014a; Donald, Roseman, imprimée, & (microfilms). 1962; Pollard & Henein, 1989; Rogers & Clements, 1972; Wightman & Muzzio, 1998b). The third type of segregation in rotating drums is called coarsening and consists of the decay in the number of bands formed from axial segregation. Coarsening appears after thousands of revolutions due to microsegregation and material transport mechanisms (Finger, Schröter, & Stannarius, 2015). For radial segregation in rotating drums, it is mostly reported that smaller particles become more concentrated in the core part of the cylinder near the active layer,

while bigger particles concentrate in the shell near the drum wall. This is also the case for the rougher and denser particles, in comparison with softer and lighter ones, respectively (Pollard & Henein, 1989; Rogers & Clements, 1972). However, there are also cases with contrary observations (Wightman & Muzzio, 1998b). Axial size segregation has been observed to take place in rotating drums, although its mechanism is not still completely known. In some studies, this phenomenon has been attributed to the difference in the repose angles of small and big particles, called trajectory mechanism. Nevertheless, it is not applicable to the reversible axial segregation (Bridgwater et al., 1985; Hill & Kakalios, 1995). On the other hand, radial segregation has been found to be due to different mechanisms such as percolation, random sieving and trajectory mechanisms (A. Boateng & Barr, 1996; Nityanand, Manley, & Henein, 1986; S. Savage & Lun, 1988). The kinetics of the radial segregation has been found to be independent of the concentration in some cases (Nityanand et al., 1986), while in other cases first-order kinetics has been suggested (Florence Cantelaube, Bideau, & Roux, 1997; Rogers & Clements, 1972). There are also studies on the kinetics of the axial segregation which investigated the effect of particle volume fraction and rotational speed on band formation in different sized granular mixtures in the rotary drum (S. D. Gupta, Khakhar, & Bhatia, 1991a; Nakagawa, 1994).

Besides experimental research, modelling and simulation have also been carried out to study different aspects of particle segregation in rotating drums. Most of these modelling studies in the literature can be classified into Eulerian and Lagrangian methods. In the first group, the granular flow is considered as a continuum (Aranson, Tsimring, & Vinokur, 1999; Aranson & Tsimring, 1999; A. Boateng & Barr, 1996; Levitan, 1998; Puri & Hayakawa, 1999), whereas in the second group discrete elements and cellular automata have been used to simulate the behaviour of the granular flow (Alizadeh et al., 2014a; Ebrahim Alizadeh, François Bertrand, & Jamal Chaouki, 2014b; Arntz, Beeftink, Otter, Briels, & Boom, 2014; Arntz, den Otter, Beeftink, Boom, & Briels, 2013; Jocelyn Doucet, Francois Bertrand, & Jamal Chaouki, 2008; Doucet, Hudon, Bertrand, & Chaouki, 2008). Many parameters are involved in DEM simulation, some of which are difficult to evaluate and, in some cases, like the Young's modulus, drastically affect the computational time. The effects of the number of simulated particles, interstitial fluid in fine powders, the complexity of the geometry of some blenders and irregularities in particle shapes and their physical interactions are amongst the reasons for some inaccuracies, which are being more and more addressed in recent

studies. For instance, with new algorithms, more advanced CPU and numerous parallel GPU power, large scale DEM (discrete element method) simulations of 225,000 particles (Lemieux et al., 2008), 0.55 million particles (Dubé, Ackley, Celik, Chaouki, & Bertrand, 2014), 7.68 million particles (Radeke, Glasser, & Khinast, 2010) and 9.6 million particles (J. Xu et al., 2011) have been performed.

Several tools for the experimental scrutiny of mixing and segregation in granular flows have been developed in recent decades. A brief comparison of such tools is surveyed in Table 5.1. Except for electrical capacitance tomography (ECT), direct sampling methods and image analysis of the solidified granular beds, other methods are non-intrusive. However, nonintrusive methods need preparations that are not always available and can be expensive in some cases. Furthermore, the application of such systems requires a higher level of skill and precision without which the results lack enough credibility. On the other hand, direct sampling with thief samplers suffers from sample contamination and is always questionable about being representative of the whole system (F. Muzzio et al., 2003; F. J. Muzzio et al., 1997).

Table 5.1 Comparison of the methods of the investigation of the mixing and segregation in granular mixers

Method		**Reference**	**Advantages**	**Limitations**
Optical techniques	Online photography, Particle image velocimetry (PIV)	(Arndt, Siegmann-Hegerfeld, Fiedor, Ottino, & Lueptow, 2005; Cho et al., 2012; Daumann, Fath, Anlauf, & Nirschl, 2009; Fiedor,	- Non-intrusive - High spatial resolution (~ 0.1 mm) - Very good temporal resolution (Chaouki, Larachi, & Duduković, 1997)	- only observe the surface of the flow

Table 5.1 Comparison of the methods of the investigation of the mixing and segregation in granular mixers (cont'd)

Method		Reference	Advantages	Limitations
		Umbanhowar, & Ottino, 2007; Gosselin, Duchesne, & Rodrigue, 2008; A.-N. Huang, Liu, & Kuo, 2013; Juarez, Lueptow, & Ottino, 2010; Xiaoyan Liu, Zhang, & Zhan, 2015; Vanarase, Osorio, & Muzzio, 2013)		
	Laser doppler velocimetry (LDV)	(Longo & Lamberti, 2002)		
	Image analysis on solidified beds	(Brone, Alexander, & Muzzio, 1998; Kuo, Shih, & Hsu, 2006; Santomaso, Olivi, &		

Table 5.1 Comparison of the methods of the investigation of the mixing and segregation in granular mixers (cont'd)

Method		Reference	Advantages	Limitations
		Canu, 2004; Wightman, Mort, Muzzio, Riman, & Gleason, 1995; Wightman & Muzzio, 1998a, 1998b; Wightman, Muzzio, & Wilder, 1996)		
Direct sampling	Thief sampling	(Alizadeh, Hajhashemi, Bertrand, & Chaouki, 2013; Mendez, de Carli, & Garcia, 2010; F. Muzzio et al., 2003; F. J. Muzzio et al., 1997; Susana, Canu, &	- Inexpensive - Less need for special instruments - Safe - Accurate	- Low spatiotemporal resolution - Cumbersome - Intrusive -Sample contamination

Table 5.1 Comparison of the methods of the investigation of the mixing and segregation in granular mixers (cont'd)

Method			Reference	Advantages	Limitations
			Santomaso, 2011)		
	Solidified bed sampling		Present study		- Intrusive - Cumbersome
Spectroscopy	Near-infrared (NIR)	Online	(Bellamy, Nordon, & Littlejohn, 2008; Berntsson, Danielsson, Lagerholm, & Folestad, 2002; El-Hagrasy, D'Amico, & Drennen, 2006; El Hagrasy, Chang, & Kiang, 2006; Hailey, Doherty, Tapsell, Oliver, & Aldridge, 1996; Scheibelhofer, Balak, Koller, &	- Non-intrusive - Low cost - Fast	- Limited to materials containing C-H, N-H and O-H bonds

Table 5.1 Comparison of the methods of the investigation of the mixing and segregation in granular mixers (cont'd)

Method			Reference	Advantages	Limitations
			Khinast, 2013; Sekulic, Wakeman, Doherty, & Hailey, 1998; Ufret & Morris, 2001; Vanarase, Alcalà, Rozo, Muzzio, & Romañach, 2010; Vanarase, Järvinen, Paaso, & Muzzio, 2013)		
		Offline	(Arratia, Duong, Muzzio, Godbole, Lange, et al., 2006; Duong et al., 2003; Mehrotra & Muzzio, 2009)		

Table 5.1 Comparison of the methods of the investigation of the mixing and segregation in granular mixers (cont'd)

Method		Reference	Advantages	Limitations
Tomography	Computed tomography (CT)	(Chester et al., 1999)	- Non-intrusive - Good spatial resolution (~1 mm) - Medium temporal resolution	- Limited to materials with the high X-ray attenuation coefficient
	Electrical capacitance tomography (ECT)	(Zhang, Wang, Yang, & Wang, 2014)	- No radiation - Lower cost than CT - Withstanding high temperature and pressure(A.-N. Huang & Kuo, 2014)	- Capacitance sensor electrodes are in contact with the material -Limited to dielectric materials
	MRI	(K. Hill, A. Caprihan, & J. Kakalios, 1997; K. M. Hill, A. Caprihan, & J. Kakalios, 1997; Metcalfe, Graham, Zhou, & Liffman, 1999; Metcalfe & Shattuck, 1996; Nakagawa, Altobelli, Caprihan,	- Non-intrusive - Excellent spatial resolution (~0.1 mm) - Medium temporal resolution(Chaouki et al., 1997)	- Limited to materials containing carbon and hydrogen bonds - The superconductor magnetic field limits the monitored system

Table 5.1 Comparison of the methods of the investigation of the mixing and segregation in granular mixers (cont'd)

Method		Reference	Advantages	Limitations
		Fukushima, & Jeong, 1993; Nguyễn, Sederman, Mantle, & Gladden, 2011; Ristow & Nakagawa, 1999)		
Particle tracking	Positron emission particle tracking (PEPT) & Positron emission imaging (PEI)	(Jones, Parker, & Bridgwater, 2007; Kuo, Knight, Parker, & Seville, 2005; Marigo et al., 2013; Martin, Seville, & Parker, 2007; Portillo et al., 2010; Rafiee, Simmons,	- Non-intrusive - Good spatial resolution (~ 5 mm)(Chaouki et al., 1997)	- weak temporal resolution - Not suited for large systems

Table 5.1 Comparison of the methods of the investigation of the mixing and segregation in granular mixers (cont'd)

Method		Reference	Advantages	Limitations
		Ingram, & Stitt, 2013)		
	Multiple-positron emission particle tracking (MUPEPT)	(Z. Yang, Parker, Fryer, Bakalis, & Fan, 2006)	- Non-intrusive - Applicable to cylindrical particles	
	Radioactive particle tracking (RPT)	(Alizadeh et al., 2014a; Alizadeh, Dubé, Bertrand, & Chaouki, 2013; Cassanello, Larachi, Marie, Guy, & Chaouki, 1995; Doucet, Bertrand, & Chaouki, 2007; Jocelyn Doucet, François Bertrand, & Jamal Chaouki, 2008; Dubé,	- Non-intrusive - Good spatial resolution (~ 5 mm)(Chaouki et al., 1997) - Good temporal resolution(Chaouki et al., 1997) - Less expensive	- Not suited for systems with irregular moving boundaries

Table 5.1 Comparison of the methods of the investigation of the mixing and segregation in granular mixers (cont'd)

Method		Reference	Advantages	Limitations
		Alizadeh, Chaouki, & Bertrand, 2013; Larachi, Chaouki, & Kennedy, 1995; Sherritt, Chaouki, Mehrotra, & Behie, 2003)		
	Multiple radioactive particle tracking (MRPT)	(Rasouli, Bertrand, & Chaouki, 2015; Rasouli, Dubé, Bertrand, & Chaouki, 2016)	- Non-intrusive - Applicable to cylindrical particles	

In this study, we are investigating the size segregation of spherical beads in a rotating drum operated in the rolling mode using bed solidification experimental methods and DEM modelling. Binary mixtures of size ratios 0.1 to 0.9 are specifically studied. This vast range of size ratio in binary mixtures with bigger size in the order of 1 cm has not been studied before and is important to realize the segregation behaviour of our ball-mill rotary-kiln reactor. In the experimental section, we are presenting a novel methodology for the characterization of solid mixtures, which is a

combination of bed solidification and direct sampling with a special sampler. This method is applicable for quantitative characterization of the mixing of any granular material bed that can be solidified by impregnating a soft binder. Comparison of the experimental results with DEM modelling shows an acceptable agreement between the two methods.

5.3 Materials and methods

5.3.1 Solidified bed sampling

The effect of size ratio on the mixing and segregation of binary mixtures of glass beads in a partially filled horizontal cylinder is studied in a custom-designed mixing setup, with a 90 v, 1750 rpm, 0.5 HP, 4.8 A direct current industrial motor (Blador Electric Co.) coupled through a 50:1 Blador gearbox to a cylinder made of plexiglass with the dimensions of L= 36 cm, D= 24 cm (Figure 5.1). The control of the rotation speed between 0.5 – 11 rpm was possible by a control panel (MTech solutions Inc.) capable of delivering varying voltage. However, for the homogeneity of the experiments and staying in rolling mode operation, the rotation speed was always set to 5.5 rpm. Glass beads of different sizes from 1 mm to 10 mm were supplied from Glen Mills Inc. (220 Delawanna Avenue, Clifton, NJ 07014). These beads are made from regular lead-free soda-lime glass with a specific gravity of 2.5. Each experiment started from a completely segregated state of one size on the top of the other. Details of the experiments are summarized in Table 5.2.

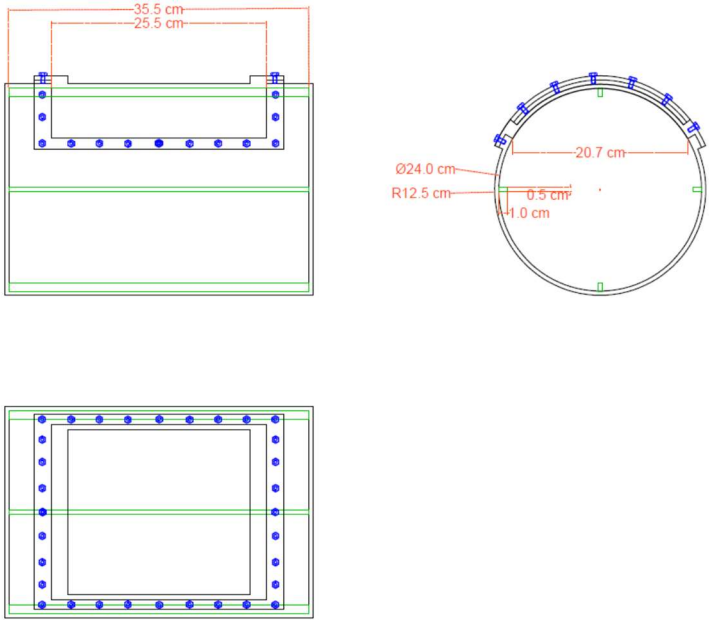

Figure 5.1 Isometric plan of the rotating drum (with removable lifters) used for the experiments

Granular-mixture-bed solidification using polymer solution has already been applied before as an undisturbed sampling method, however the samples were studied by image analysis on the surface (F. J. Muzzio et al., 1997). In this method they added the polymer solution to the granular mixture to penetrate the bed of particles and fill voids by displacing air. The solution solidified the bed upon evaporation of the solvent. They cut the solidified bed and studied the surface by image analysis. However, in our method we analyse the whole cut samples by re-separating the particles.

Within the initial few rotations in each experiment, a steady configuration forms in radial and axial directions. This number of rotations is higher for higher size ratios (near unity), although it does not exceed 100 rotations in any case. Therefore a 20-min time was always maintained before stopping the mixer and starting the solidification process.

Table 5.2. Conditions of the experiments performed in this study

Experiment	**Bead size ratio (mm/mm)**	**Number of beads in each sample (n)**	**Rotation rate (rpm)**	**Results**
A1	6/10	12035		

A2	4/10	4211		
A3	3/10	610		
A4	2.65/10	469	5.5	Fig.3
A5	1.7/10	273		
A6	1/10	83		
B1	1/8	12748		
B2	1.7/8	4439	5.5	Fig. 4
B3	2.65/8	653		

After each experiment is completed, the mixer is stopped, and the repose angle is measured. Then the drum is slowly turned inversely to the amount of the repose angle (α), in a way that does not disturb the configuration of the bed, to make the bed surface parallel to the horizon. This way, the amount of solidifying material is minimized, and the solidified bed will be easier to manipulate (Figure 5.2).

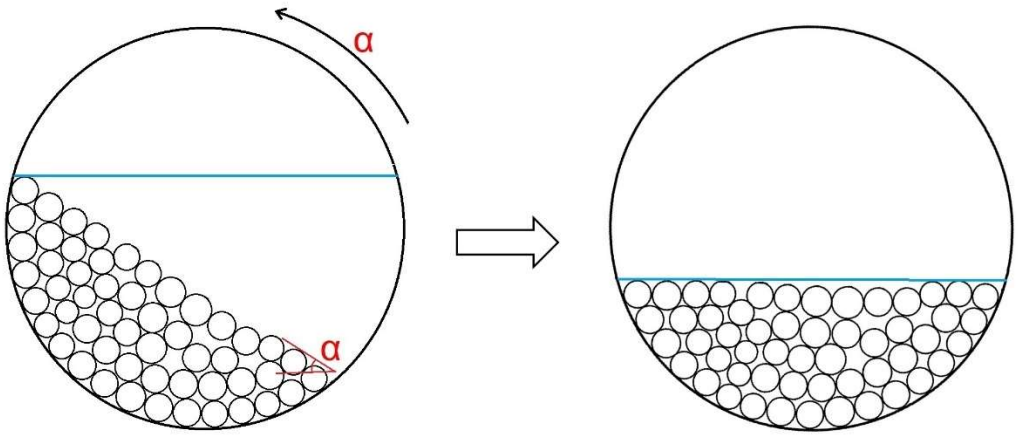

Figure 5.2 Inverse turning of the bed to make the bed surface parallel to the horizon

After that, we prepared a 1.5 % agar solution in boiling water and added it to our bed mixture at around 90 ℃ to fill in the space between the beads and cover the bed. Agar powder was supplied from Bio Basic Inc. (20 Konrad Cres. Markham Ontario L3R 8T4 Canada) as a solidifying agent. It was delivered as a white cream powder with 80/100 mesh size with 11 % moisture. The 1.5 % aqueous solution gives a gel with 750-1100 g/cm^2 strength (Nikan) at temperatures lower than 40 ℃ that can be easily cut. Using this approach, the whole system can be preserved with no disturbance, and the real composition of any spatial position can be measured by dividing the cross-section into several samples using a special sampling tool. The advantages of choosing this solidifying agent were: (1) It is an inexpensive, abundant biodegradable material. (2) It melts in a safe temperature range that does not damage our cylinder and can be reused several times. (3) It is solid at room temperature with a proper consistency to be easily moulded without disturbing the fixed configuration. (4) It percolates easily along the bed. (5) Complete solidification and cooling to room temperature take 6 hours (in our drum scale).

A special sampling tool was designed and inexpensively fabricated from Plexiglass to tailor the cross-section of our rotary drum and take several samples from the whole cross-section of any axial position of the drum (Figure 5.3). To access the cross-section of the solidified bed, we cut a section of the bed with a length of 15 cm and evacuated from the cylinder to provide enough space for the special tool for sampling. After placing the sampling tool in the evacuated space and applying a horizontal force, the cross-section becomes divided into 26 squares and semi-squares (in the borders). There is a small hole at the bottom of each sampling room to let out the entrapped air. The rooms of the sampler were coded as 1A to 1H for the first row, 2A to 2H for the second row, 3B to 3G for the third row and from 4C to 4F for the fourth row (see Figure 5.3). The samples from each room were extracted to a plastic container with the same code using a small spatula. The mixtures of the small and big particles and the accompanying gel were microwaved for two minutes to liquify the gel and washed with hot water to remove the remaining gel. Each sample was drained and dried with a heat gun before the separation of particles using the proper sieve. The separated particles were weighed accordingly and gave the concentration of smaller particle in each cube of the corresponding cross-section.

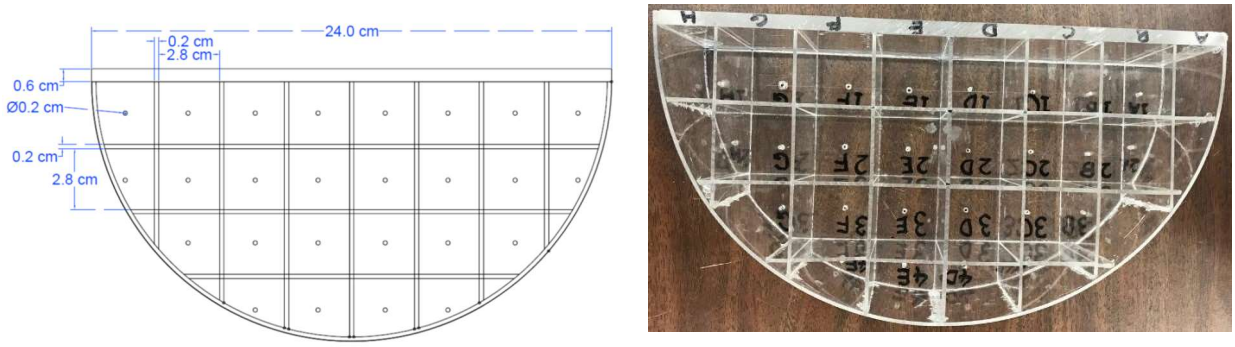

Figure 5.3 Special tool designed and fabricated for the sampling of the solidified bed of the rotating drum in this study

5.3.2 DEM simulation

The DEM is a Lagrangian time-driven simulation method that has been widely used in predicting the flow pattern of granular matter in different processes like mixing, tumbling, conveying, drying, calcining and solid-solid, gas-solid and liquid-solid reactions. In this method, Newton's second law of motion is integrated with respect to time to determine the temporal evolution of the physical properties of each particle, including its position and linear and angular velocities. The particle-particle and particle-wall collisions are detected by allowing them to overlap at the boundaries according to a contact model, and the imposed forces are calculated based on a spring-and-dashpot model. This force and the gravity are assumed as the total forces acting on every particle and determine their motion. Drag and buoyancy forces in our system were neglected because the fluid phase was air. All other interparticle forces were also negligible, as the particle size range was in the order of millimetres. The contact force between two spherical particles or a spherical particle and the blender wall is composed of normal and tangential components, and each component has a repulsion part (f_{el}) and a dissipative part (f_{dis}). The repulsion part depends on how hard the collision is, that is indicated by the overlap at the boundaries (δ), and the dissipative part is a result of the energy dissipation in the collision. Therefore, the contact force between two particles or between a particle and the wall was calculated using the general following equation (Blais, Vidal, Bertrand, Patience, & Chaouki, 2019):

$$f_{c,ij} = k_{n,ij}\left\|\delta_{n,ij}\right\|^{a}\delta_{n,ij} + \gamma_{n,ij}\left\|\delta_{n,ij}\right\|^{b}\dot{\delta}_{n,ij} + k_{t,ij}\left\|\delta_{n,ij}\right\|^{c}\delta_{t,ij} + \gamma_{t,ij}\left\|\delta_{n,ij}\right\|^{d}\dot{\delta}_{t,ij} \quad (5.1)$$

where $k_{n,ij}$ and $k_{t,ij}$ are the normal and tangential stiffness coefficients, $\gamma_{n,ij}$ and $\gamma_{t,ij}$ the normal and tangential damping coefficients, $\delta_{n,ij}$ and $\delta_{t,ij}$ the normal and tangential particle overlaps, $\dot{\delta}_{n,ij}$ and $\dot{\delta}_{t,ij}$ their derivatives with respect to time, and a, b, c, and d are positive constants.

In our case, since a Hertz model was used, the exponents a, b, c and d are equal to ½, ¼, ½ and ¼ respectively. The coefficients are defined in Table 5.3 and were chosen based on glass beads properties.

Here, we simulated our experiments described in the previous section with the same geometry and conditions through the open-source code of LIGGGHTS to compute the DEM part. The diameter of particles, the number of particles and the time step used for each simulation are defined in Table 5.4. The time step was chosen like 10% of the Rayleigh time (t_R) defined in the next equation.

$$t_R = \frac{\pi R}{0.8766 + 0.163\nu}\sqrt{\frac{\rho}{E/2(1+\nu)}} \quad (5.2)$$

Table 5.3 Physical and mechanical particle properties used for DEM simulations (cont'd)

Properties	Symbol	Value
Density (g/cm3)	ρ	2500
Young's modulus (MPa)	E	1e7
Poisson's ratio	ν	0.2
Coefficient of restitution	e	0.7
Coefficient of friction	μ	0.4

Table 5.3 Physical and mechanical particle properties used for DEM simulations (cont'd)

Coefficient of rolling friction	μ_r	0.7
Normal stiffness coefficient	$k_{n,ij}$	$\frac{4}{3}E^*\sqrt{R^*}$
Tangential stiffness coefficient	$k_{t,ij}$	$8G^*\sqrt{R^*}$
Normal damping coefficient	$\gamma_{n,ij}$	$-2\sqrt{\frac{5}{6}}\beta\sqrt{2E^*(R^*)^{1/2}m^*}$
Tangential damping coefficient	$\gamma_{t,ij}$	$-2\sqrt{\frac{5}{6}}\beta\sqrt{8G^*(R^*)^{1/2}m^*}$
Reduced radius	R^*	$\frac{1}{R^*}=\frac{1}{R_1}+\frac{1}{R_2}$
Reduced mass	m^*	$\frac{1}{m^*}=\frac{1}{m_1}+\frac{1}{m_2}$
Reduced Young modulus	E^*	$\frac{1}{E^*}=\frac{(1-\nu_1^2)}{E_1}+\frac{(1-\nu_1^2)}{E_1}$
Reduced shear modulus	G^*	$\frac{1}{G^*}=\frac{2(2-\nu_1)(1+\nu_1)}{E_1}+\frac{2(2-\nu_2)(1+\nu_2)}{E_2}$
Beta	β	$\frac{\ln(e)}{\sqrt{ln^2(e)+\pi^2}}$

The DEM simulations were performed in parallel using 4 cores of 2.1 GHz processors of Intel E5-2683 v4 Broadwell of the Graham cluster managed by Compute Canada.

Table 5.4 Characteristics of the DEM simulations (cont'd)

Case	Simulation	Number of small particles	Number of large particles	Time step (loading) (s)	Time step (rolling) (s)
1	7 % 1mm/10mm	63504	762	6.00E-06	6.00E-06
2	20% 2mm/10mm	23814	762	1.69E-05	1.69E-05
3	20% 3mm/10mm	7056	762	1.30E-05	1.30E-05
4	20% 4mm/10mm	2977	762	2.50E-05	1.30E-05
5	20% 5mm/10mm	1524	762	4.23E-05	4.23E-05
6	20% 6mm/10mm	882	762	5.08E-05	5.08E-05
7	20% 7mm/10mm	555	762	5.92E-05	5.92E-05
8	20% 8mm/10mm	372	762	6.77E-05	6.77E-05
9	20% 9mm/10mm	261	762	7.62E-05	7.62E-05

5.4 Results and discussion

5.4.1 Solidified bed sampling method results

In the first part of this section, the effect of size ratio on the radial mixing and segregation of binary mixtures in a rotating drum is investigated by bed solidification experiments. The combinations of the binary sizes are shown in Table 5.2.

Variability in the composition of a granular mixture is an intrinsic characteristic of such systems that comes from their discrete nature. The number of particles in a sample from a granular mixture is much smaller than that from a molecular solid, liquid or even gas mixture. Therefore, the quality

of mixing of a granular system cannot be judged with a single sample or several samples at a certain point in the drum. A reasonable assessment of the degree of mixing in these mixtures is to compare this intrinsic variability with the variability of the same system when it is randomly mixed, which is the best achievable mixing for that system. For a binary granular mixture which is composed of granules with two different sizes, the relative standard deviation (RSD) of the blend and the relative standard deviation of the randomly mixed blend (RSD_r) are defined as (Lacey, 1954; Paul, Atiemo-Obeng, & Kresta, 2004):

$$RSD = \frac{\sigma}{\bar{x}} = \frac{Standard\ deviation\ of\ the\ current\ mixture}{Average\ composition} \tag{5.3}$$

$$RSD_r = \frac{\sigma_r}{\bar{x}} = \frac{Standard\ deviation\ of\ the\ random\ mixture}{Average\ composition} \tag{5.4}$$

The standard deviations of the blend and randomly mixed blend are the square roots of the corresponding variances:

$$\sigma = \sqrt{\frac{\sum_{i=1}^{N}(x_i - \bar{x})^2}{N-1}} \tag{5.5}$$

$$\sigma_r = \sqrt{\frac{\bar{x}(1-\bar{x})}{n}} \tag{5.6}$$

where x_i is the composition of each sample, N is the number of samples, and n is the number of granules in each sample, which is specific to each size ratio and composition, and is determined experimentally. For instance, for a bidisperse mixture, the number of total particles in one sample was calculated by dividing the weight of each particle type (the smaller or the bigger) to the average weight of the individual particle of that type and adding the two numbers.

For each size ratio, after loading the granules of the two sizes with top-bottom configuration, mixing started with 5.5 rpm corresponding to minimum speed for the rolling regime. After 20 min (110 rotations), the mixing stopped, and sampling and characterization were performed. Convection and to a lower extent dispersion are the most significant mechanisms that lead to this

final steady mixture in a low number of revolutions. Shear mixing mechanism is not effective here as it happens in more cohesive mixtures. The results of the size ratios ranging from 0.1 to 0.6 with the larger particle size equal to 10 mm (set A) and 8 mm (set B) are shown in Figure 5.4. The RSD vs. size ratio (SR=$\frac{d}{D}$) may be modelled via the following polynomials with the coefficient of determination (R^2) of 0.87 for experiment set A (A1 to A6).

$$RSD = -796.21\left(\frac{d}{D}\right)^3 + 900.64\left(\frac{d}{D}\right)^2 - 272.04\left(\frac{d}{D}\right) + 38.703 \qquad (5.7)$$

After deriving the RSD model from experiment set A, experiment set B was performed to verify the same critical behaviour, especially at lower size ratios that were of interest for the application in the BaMRoK. The local minimum RSD in the experiments A1 to A6 happens at 0.21 size ratio. However, the closest RSD to the corresponding RSD_r of the random mixtures is at slightly higher size ratio of 0.26. These two critical size ratios for the experiments B1 to B3 are 0.2 and 0.24 respectively, which is in good agreement with the model for set A. Also, the size ratio corresponding to the local maximum RSD for the experiment set A is at 0.54, while the furthest RSD from the corresponding RSD_r of the random mixtures is at slightly lower size ratio of 0.47. The segregation behaviour of the system changes in these transition size ratios that will be explained in the next section.

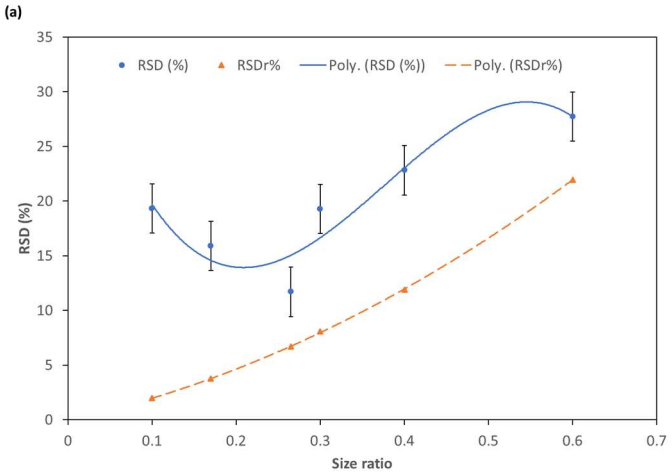

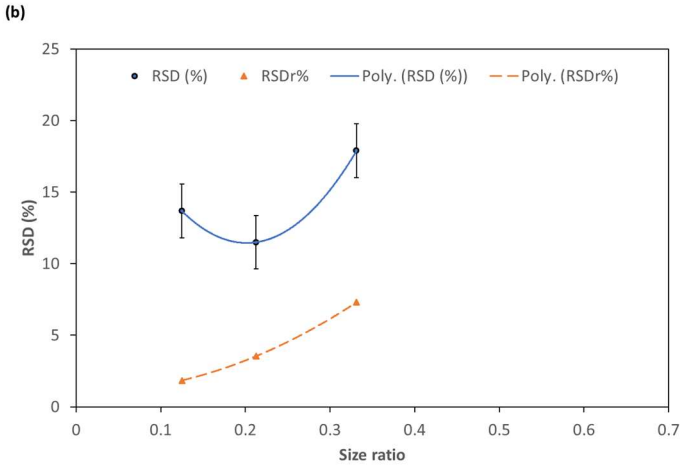

Figure 5.4 Final RSD of binary mixtures versus size ratio after 110 revolutions (continuous line) compared to RSD of corresponding random mixtures (dashed line), (a) Experiments A1 to A6, (b) Experiments B1 to B3

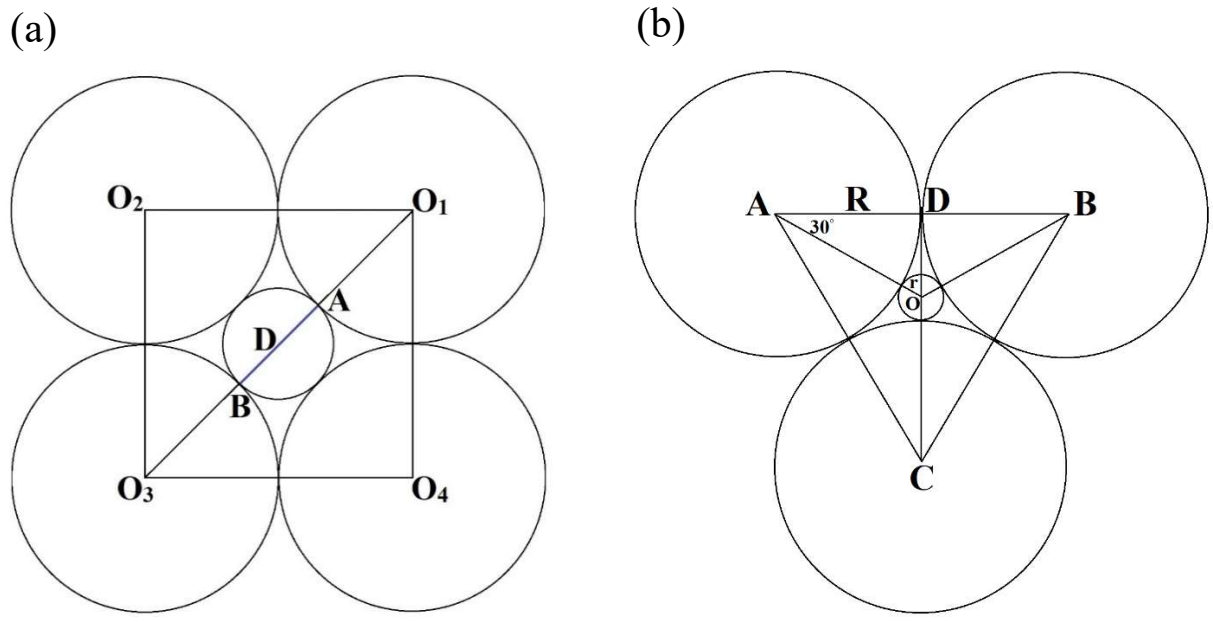

Figure 5.5 Planar sections of adjacent spheres in binary spherical mixtures. (a) non-compact $r_a \cong 0.41R$, (b) compact configurations $r_b \cong 0.15R$ (r_a and r_b are the radii of inscribed spheres and R is the radius of circumscribed spheres)

Geometrically, in a close-packed structure like hexagonal close-packed (hcp), the inscribed sphere between 3 spheres has a size ratio of 0.15 relative to circumscribed spheres. This size ratio for the inscribed sphere between 4 coplanar spheres in a less compact arrangement is 0.41 (Figure 5.5). These ratios can give an interpretation of the transitional size ratios derived from RSD curves in Figure 5.4.

For the size ratios larger than 0.41 (0.47 or 0.54 in the RSD curves of Figure 5.4) the only mixing mechanism is convection, as there is no diffusive mixing, while the mechanisms acting for segregation are the trajectory and the sifting mechanisms without kinetic sieving. Under these conditions, the smaller particles avalanche to the bottom of the active layer without diffusing to the lower layers and consequently accumulate in the middle of the bed by convection. For size ratios smaller than 0.41 diffusive mixing becomes significant and decrease the RSD. As the size ratio approaches to the unity, final segregation decreases because of more uniformity in sizes. At the size ratios less than 0.41, the diffusive mixing mechanism becomes significant and as the size ratio further decreases, diffusive mixing increases until final RSD reaches its minimum or closest point to the RSD_r at a critical size ratio (0.26 or 0.24 in the RSD curves of Figure 5.4). By further decreasing of the size ratio, kinetic sieving becomes the dominant segregation mechanism and segregation increases.

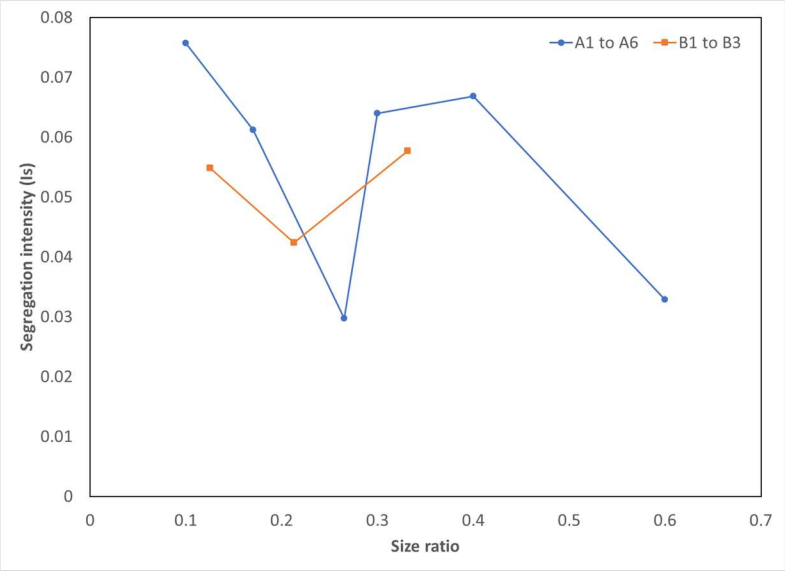

Figure 5.6 Final segregation intensity of binary mixtures versus size ratio after 110 revolutions

Therefore, in a free-flowing spherical binary system like our experiment, particles with size ratios smaller than 0.15 will end up in a totally segregated state at the bottom of the passive layer. This is what we can also see from our segregation intensity (I_s) versus size ratio graph in Figure 5.6. I_s is one of the most common criteria to assess the segregation state of a granular mixture and is, by definition, the ratio of the change in concentration variance to the largest possible change. As this method lacks sensitivity, it may not well reveal small changes in segregation state (Rhodes, 2008). Therefore, the modified form of segregation intensity, which is more sensitive to changes, is used (Alizadeh, Hajhashemi, et al., 2013; Paul et al., 2004):

$$I_s = \frac{\sigma - \sigma_r}{\sigma_0 - \sigma_r} \tag{5.8}$$

in which, σ and σ_r can be obtained from Equations 5.5 and 5.6, and $\sigma_0 = \sqrt{\bar{x}(1-\bar{x})}$ is the variance of the most segregated state (Lacey, 1954).

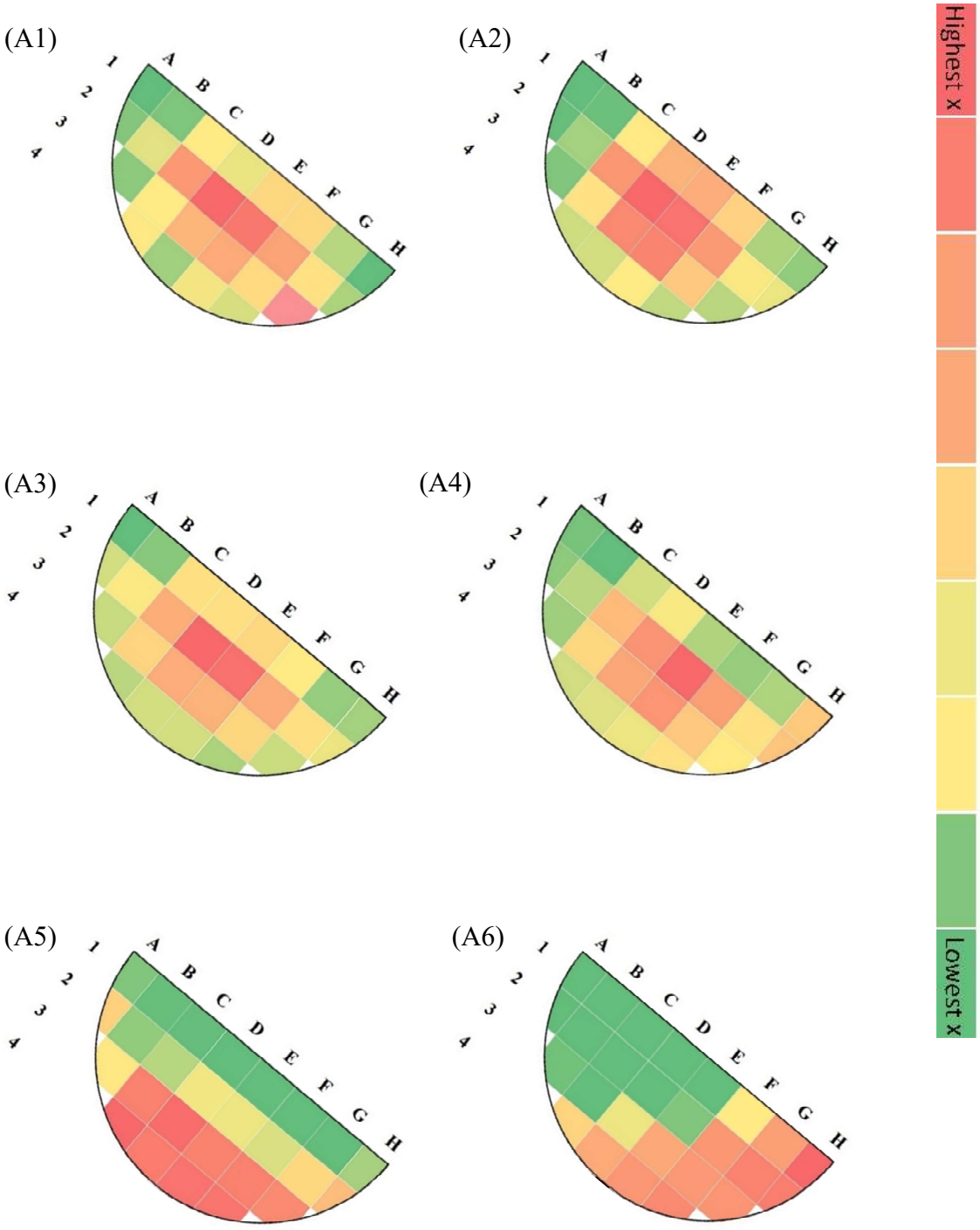

Figure 5.7 Final occupancy plots of binary mixtures in experiments A1 to A6 (Table 5.2) after 110 revolutions. Green is the lowest and red is the highest x (concentration of smaller beads)

The transitional size ratios at 0.2 and 0.5 are also seen here. The local minimum segregation intensity is also at the same size ratio for the two sets of the experiments. At the higher end of the size ratios, the segregation intensity approaches zero because the system changes gradually from bidisperse to monodisperse. As the size ratio approaches zero, the segregation intensity approaches its maximum mainly due to the kinetic sieving mechanism mostly in the active layer and to some extent in the passive layer. This was especially the case because of the low cohesive nature of our free-flowing mixture and was more evident at lower size ratios. A local maximum in segregation intensity happens in higher size ratios (around 0.4 in set A), in which smaller particles accumulate in the core region of the material bed near the rotation axis. This phenomenon has been reported in previous studies (F Cantelaube & Bideau, 1995; Rapaport, 2007; Thomas, 2000; Wightman & Muzzio, 1998b).

Sifting and trajectory mechanisms are the most significant mechanisms responsible for this core-shell segregation. This segregation almost completely happens in the active layer and takes place after a few revolutions.

These results from RSD and I_s curves are graphically depicted by the occupancy plots drawn from the concentration data obtained from 26 samples of the radial cross-section of the material bed in the rotating drum (Figure 5.7). A1 and A2 in these figures show a clear accumulation of smaller beads (6 mm and 4 mm) in the middle of the bed (red and orange areas) in contrast with the bigger beads (10 mm) distributed more in surrounding areas, especially on the top of the active zone (green areas in Figure 5.7A1 and 5.7A2). A3 and A4 show a smaller core of smaller beads (3 mm and 2.65 mm) corresponding to the size ratios 0.3 and 0.265. However, there are less pure green and pure red areas and more yellow areas corresponding to a more uniform distribution of smaller beads in the bigger ones. A5 and A6 show evident complete segregation of smaller beads (1.7 mm and 1 mm equivalent to size ratios 0.17 and 0.1) in the bottom from the larger beads (10 mm) on the top. The smaller beads are more drawn to the downstream of the active layer in A6, due to the two mechanisms discussed before.

5.4.2 DEM results

The DEM-based model described in section 5.3.2 was used to study the size segregation behaviour and the critical size ratios in a bidisperse mixing in a rotating drum as in our ball-mill rotary kiln reactor. The DEM results are compared to our bed-solidification experimental results to check their validity and are extended to other size ratios that were not studied experimentally and also used to find the temporal evolution of the RSD for different size ratios. The geometry and the physical properties of the granules and the rotating drum were chosen same as the experiments.

Figure 5.8 shows the RSD changes by time (revolutions) for different size ratios. For all size ratios, the time needed to reach the final RSD increases by size ratio. For the size ratios of 0.1, 0.2, 0.3, 0.4, 0.5 and 0.6 the RSD decreases from the most segregated state (top-bottom configuration) and reaches its final value in less than 30 seconds or 3 cycles of rotation. For the size ratios 0.7 and 0.8, this time is less than 2 minutes or 11 rotations and for the size ratio 0.9, it is around 3 minutes (17 rotations). Therefore, the 20 minutes rotation time before solidification and sampling in experiments has been enough.

Based on the RSD curves obtained from DEM simulations, the final RSD after the initial 4-min period for all cases were averaged and plotted versus size ratio in Figure 5.9. This figure compares the final RSD from the experimental section (solidified bed sampling) with the corresponding DEM results in size ratios 0.1 to 0.6. As it is depicted, the DEM results are in good agreement with the experimental RSD measurements.

Also, the proposed model from experimental data (Equation 5.7) is in acceptable accordance with DEM results in low size ratios. The minimum and maximum RSD obtained from the DEM model are also at almost the same critical size ratios that were observed in the bed solidification sampling experiments (0.2 and 0.5).

Similar observations to the experimental occupancy plots were made with final occupancy plots obtained from DEM simulations (Figure 5.10). It can be seen from these plots that the small granules are accumulated in the middle of the bed (near the rotation axis) in size ratios 0.3, 0.4, 0.5, and 0.6. However, at size ratio 0.2, they have been distributed around this area, causing the minimum RSD seen in RSD curves. At the size ratio 0.1, the percolation or kinetic sieving

mechanism has caused a complete segregated state of the small granules at the bottom near the shell of the rotating drum.

Extending the DEM simulation to the larger size ratios (0.6 – 0.9) that were not experimentally studied, revealed the gradual decrease in the RSD and the disappearance of the core-shell segregation near the unit size ratio. Also, the DEM simulations showed that at the size ratios with least segregation (0.26 and 0.9) the time needed to reach the final RSD is longer than other size ratios and this time decreases as the segregation increases.

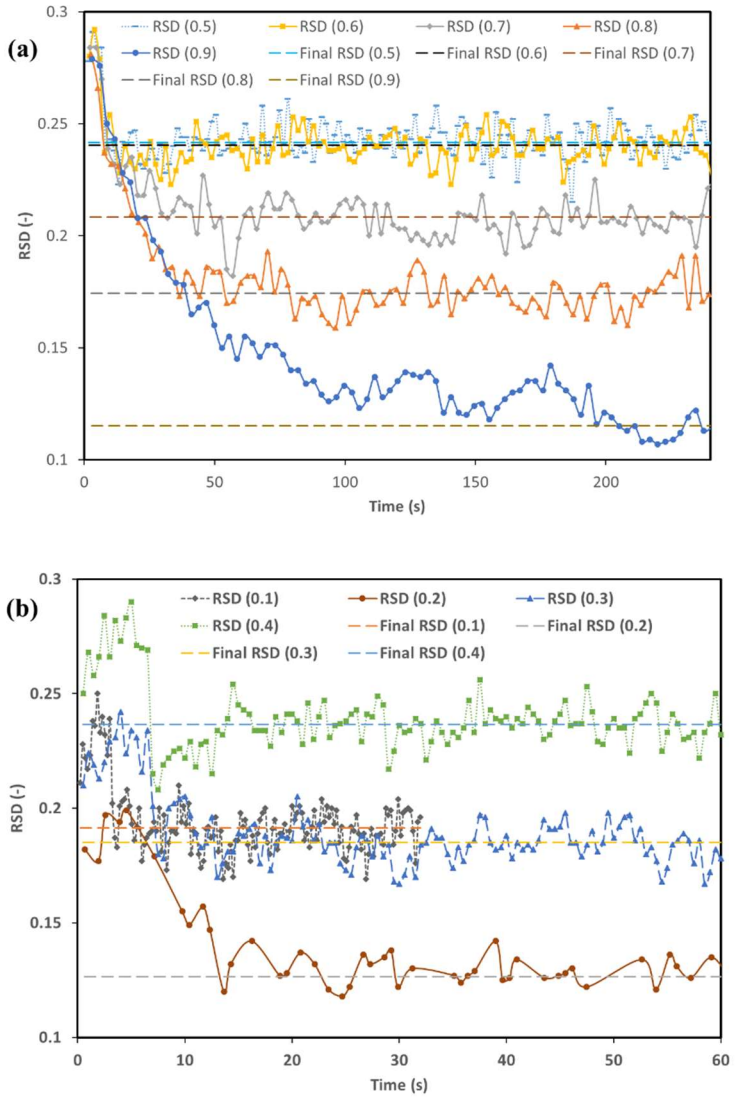

Figure 5.8 The temporal evolution of the RSD of the binary spherical mixtures from completely segregated situation (top-bottom), simulated by DEM, (a) size ratios 0.5, 0.6, 0.7, 0.8, 0.9 and (b) size ratios 0.1, 0.2, 0.3, 0.4

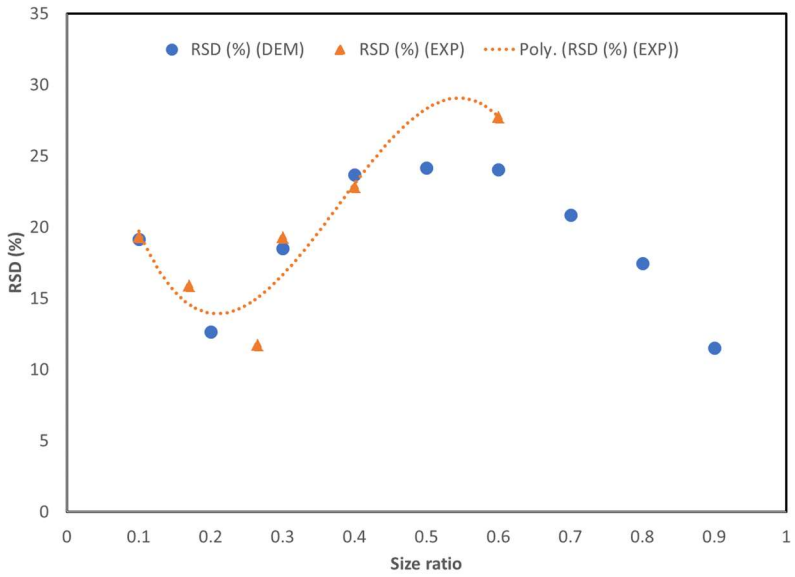

Figure 5.9 Comparison of the RSD data obtained from DEM simulations and solidified-bed sampling method and the model obtained therefrom for different size ratios

5.5 Conclusion

Solidified-bed sampling with the designed matrix sampler, despite other direct sampling methods, can be used to provide a non-intruded complete profile of the rotating drums for non-cohesive non-soluble granular mixtures. The results obtained with this method, along with the complementary DEM simulations, revealed the effect of size ratio on the quantity and the quality of segregation in bidisperse spherical mixtures in a rotating drum at rolling regime. Two critical size ratios at around 0.2 and o.5 corresponding to the local minimum and maximum segregation were discovered. The local maximum segregation at the size ratio of 0.5 forms a core shell structure by accumulating the smaller granules at the core as a result of the sifting and trajectory segregation mechanisms. For size ratios less than 0.2, kinetic sieving (percolation) segregation mechanism becomes more dominant and smaller granules percolate to the bottom of the bed at the vicinity of the internal surface of the drum wall. This can be used as a criterion for the selection of the ball size in a BaMRoK reactor, in case the vicinity of the reacting powder material to the internal surface of the drum is more favorable for the heating through the drum wall.

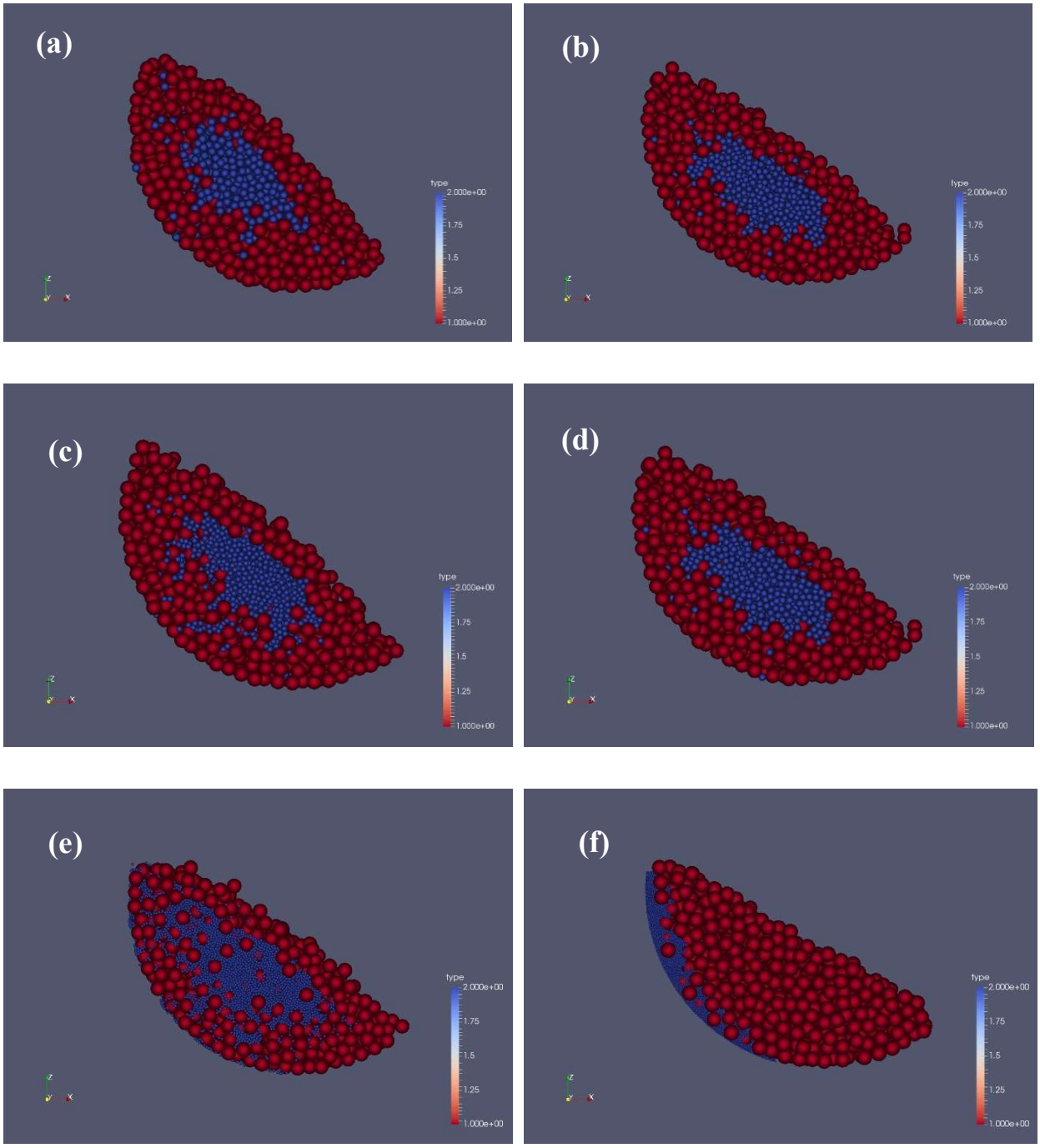

Figure 5.10 DEM simulation of final occupancy plots of binary mixtures with different size ratios: (a) 6 mm/10 mm, (b) 5 mm/10 mm, (c) 4 mm/10 mm, (d) 3 mm/10 mm, (e) 2 mm/10 mm, (f) 1 mm/10 mm, after 110 revolutions

Based on the obtained results for a solid-state reaction like calcination and dehydration of fine powders in a BaMRoK with grinding media more than 5 times bigger than the particles, intensive segregation happens by kinetic sieving (percolation) mechanism, and the reactive material accumulates at the bottom of the bed at the vicinity of the internal surface of the kiln wall. For an electrical indirect heated rotary kiln, the material is exposed to the highest temperature inside the kiln instead of the lower temperature of the media. For grinding purposes in a ball mill, the best efficiency of the mill would be in the size ratio of the media to the particle at around 0.25 and the least efficiency may correspond to the size ratios around 0.5 or less than 0.2, with particles segregated in the core for the former and next to the wall for the latter.

Acknowledgements

The authors would like to acknowledge the technical support of the staff of the department of chemical engineering of Polytechnique Montreal, Dr. David Vidal, Mr. Sylvain Simard Fleury and Mr. Yanik Landry-Ducharme. The financial support of the Natural Sciences and Engineering Research Council of Canada (NSERC) and the Canada Foundation for Innovation (CFI) through the Automotive Partnership Canada program is gratefully acknowledged. The authors are also appreciative for the financial and technical support from industrial partner Johnson Matthey Battery Materials. All simulations were made possible thanks to the computational resources of Compute Canada.

5.6 References

1. Boateng, A.A., *Rotary kilns: transport phenomena and transport processes*. 2015: Butterworth-Heinemann.
2. Barker, G.C. and A. Mehta, *Size segregation in powders.* Nature, 1993. **361**: p. 308.
3. Barker, G.C. and A. Mehta, *Size segregation mechanisms.* Nature, 1993. **364**: p. 486.
4. Choi, J., et al. *Separation of metallic particles by vertical vibration for solid waste treatment*. in *Environmentally Conscious Design and Inverse Manufacturing, 1999. Proceedings. EcoDesign'99: First International Symposium On*. 1999. IEEE.

5. Habib, M., et al., *Separation of dry particulate mixtures by controlled vertical vibration.* Particulate Science and Technology, 2013. **31**(6): p. 555-560.

6. Wang, S., et al., *Separation Process of Fine Coals by Ultrasonic Vibration Gas-Solid Fluidized Bed.* International Journal of Analytical Chemistry, 2017. **2017**.

7. Cleary, P.W., *Predicting charge motion, power draw, segregation and wear in ball mills using discrete element methods.* Minerals Engineering, 1998. **11**(11): p. 1061-1080.

8. Cleary, P.W., *Ball motion, axial segregation and power consumption in a full scale two chamber cement mill.* Minerals Engineering, 2009. **22**(9): p. 809-820.

9. Bridgwater, J., *Fundamental powder mixing mechanisms.* Powder Technology, 1976. **15**(2): p. 215-236.

10. Bridgwater, J., W. Foo, and D. Stephens, *Particle mixing and segregation in failure zones—theory and experiment.* Powder technology, 1985. **41**(2): p. 147-158.

11. Savage, S.B., *Granular flows down rough inclines-review and extension*, in *Studies in Applied Mechanics*. 1983, Elsevier. p. 261-282.

12. Donald, M.B., et al., *Mixing and demixing of solid particles. I. Mechanisms in a horizontal drum mixer.* Br. Chem. Eng., 1962. **7**: p. 749-53.

13. Rogers, A. and J. Clements, *The examination of segregation of granular materials in a tumbling mixer.* Powder Technology, 1972. **5**(3): p. 167-178.

14. Pollard, B. and H. Henein, *Kinetics of radial segregation of different sized irregular particles in rotary cylinders.* Canadian Metallurgical Quarterly, 1989. **28**(1): p. 29-40.

15. Wightman, C. and F.J. Muzzio, *Mixing of granular material in a drum mixer undergoing rotational and rocking motions II. Segregating particles.* Powder Technology, 1998. **98**(2): p. 125-134.

16. Finger, T., M. Schröter, and R. Stannarius, *The mechanism of long-term coarsening of granular mixtures in rotating drums.* New Journal of Physics, 2015. **17**(9): p. 093023.

17. Hill, K. and J. Kakalios, *Reversible axial segregation of rotating granular media.* Physical Review E, 1995. **52**(4): p. 4393.

18. Nityanand, N., B. Manley, and H. Henein, *An analysis of radial segregation for different sized spherical solids in rotary cylinders.* Metallurgical transactions B, 1986. **17**(2): p. 247-257.

19. Savage, S. and C. Lun, *Particle size segregation in inclined chute flow of dry cohesionless granular solids.* Journal of Fluid Mechanics, 1988. **189**: p. 311-335.

20. Boateng, A. and P. Barr, *Modelling of particle mixing and segregation in the transverse plane of a rotary kiln.* Chemical Engineering Science, 1996. **51**(17): p. 4167-4181.

21. Cantelaube, F., D. Bideau, and S. Roux, *Kinetics of segregation of granular media in a two-dimensional rotating drum.* Powder technology, 1997. **93**(1): p. 1-11.

22. Gupta, S.D., D. Khakhar, and S. Bhatia, *Axial segregation of particles in a horizontal rotating cylinder.* Chemical engineering science, 1991. **46**(5-6): p. 1513-1517.

23. Nakagawa, M., *Axial segregation of granular flows in a horizontal rotating cylinder.* Chemical Engineering Science, 1994. **49**(15): p. 2540-2544.

24. Aranson, I., L. Tsimring, and V. Vinokur, *Continuum theory of axial segregation in a long rotating drum.* Physical Review E, 1999. **60**(2): p. 1975.

25. Aranson, I. and L.S. Tsimring, *Dynamics of axial separation in long rotating drums.* Physical review letters, 1999. **82**(23): p. 4643.

26. Levitan, B., *Segregation and coarsening of granular mixture in a rotating tube.* Physica A: Statistical Mechanics and its Applications, 1998. **249**(1-4): p. 386-390.

27. Puri, S. and H. Hayakawa, *Dynamical behavior of rotated granular mixtures.* Physica A: Statistical Mechanics and its Applications, 1999. **270**(1-2): p. 115-124.

28. Arntz, M., et al., *Segregation of granular particles by mass, radius, and density in a horizontal rotating drum.* AIChE journal, 2014. **60**(1): p. 50-59.

29. Arntz, M., et al., *The influence of end walls on the segregation pattern in a horizontal rotating drum.* Granular matter, 2013. **15**(1): p. 25-38.

30. Doucet, J., F. Bertrand, and J. Chaouki, *A measure of mixing from Lagrangian tracking and its application to granular and fluid flow systems.* Chemical Engineering Research and Design, 2008. **86**(12): p. 1313-1321.

31. Doucet, J., et al., *Modeling of the mixing of monodisperse particles using a stationary DEM-based Markov process.* Computers & Chemical Engineering, 2008. **32**(6): p. 1334-1341.

32. Alizadeh, E., F. Bertrand, and J. Chaouki, *Comparison of DEM results and Lagrangian experimental data for the flow and mixing of granules in a rotating drum.* AIChE Journal, 2014. **60**(1): p. 60-75.

33. Alizadeh, E., F. Bertrand, and J. Chaouki, *Discrete element simulation of particle mixing and segregation in a tetrapodal blender.* Computers & Chemical Engineering, 2014. **64**: p. 1-12.

34. Lemieux, M., et al., *Large-scale numerical investigation of solids mixing in a V-blender using the discrete element method.* Powder Technology, 2008. **181**(2): p. 205-216.

35. Radeke, C.A., B.J. Glasser, and J.G. Khinast, *Large-scale powder mixer simulations using massively parallel GPUarchitectures.* Chemical Engineering Science, 2010. **65**(24): p. 6435-6442.

36. Xu, J., et al., *Quasi-real-time simulation of rotating drum using discrete element method with parallel GPU computing.* Particuology, 2011. **9**(4): p. 446-450.

37. Arndt, T., et al., *Dynamics of granular band formation: Long-term behavior in slurries, parameter space, and tilted cylinders.* Physical Review E, 2005. **71**(1): p. 011306.

38. Fiedor, S.J., P. Umbanhowar, and J.M. Ottino, *Effects of fluid viscosity on band segregation dynamics in bidisperse granular slurries.* Physical Review E, 2007. **76**(4): p. 041303.

39. Juarez, G., R.M. Lueptow, and J.M. Ottino, *Granular coarsening: Phase space and evolution analogies.* Physical Review E, 2010. **81**(1): p. 012301.

40. Huang, A.-N., L.-C. Liu, and H.-P. Kuo, *The role of end wall shearing in the drum segregation band formation.* Powder technology, 2013. **239**: p. 98-104.

41. Vanarase, A.U., J.G. Osorio, and F.J. Muzzio, *Effects of powder flow properties and shear environment on the performance of continuous mixing of pharmaceutical powders.* Powder technology, 2013. **246**: p. 63-72.

42. Daumann, B., et al., *Determination of the mixing time in a discontinuous powder mixer by using image analysis.* Chemical Engineering Science, 2009. **64**(10): p. 2320-2331.

43. Cho, J., et al., *Solving granular segregation problems using a biaxial rotary mixer.* Chemical Engineering and Processing: Process Intensification, 2012. **57**: p. 42-50.

44. Liu, X., C. Zhang, and J. Zhan, *Quantitative comparison of image analysis methods for particle mixing in rotary drums.* Powder Technology, 2015. **282**: p. 32-36.

45. Gosselin, R., C. Duchesne, and D. Rodrigue, *On the characterization of polymer powders mixing dynamics by texture analysis.* Powder Technology, 2008. **183**(2): p. 177-188.

46. Chaouki, J., F. Larachi, and M.P. Duduković, *Noninvasive tomographic and velocimetric monitoring of multiphase flows.* Industrial & engineering chemistry research, 1997. **36**(11): p. 4476-4503.

47. Longo, S. and A. Lamberti, *Grain shear flow in a rotating drum.* Experiments in fluids, 2002. **32**(3): p. 313-325.

48. Kuo, H., P. Shih, and R. Hsu, *Coupled axial–radial segregation in rotating drums with high fill levels.* AIChE journal, 2006. **52**(7): p. 2422-2427.

49. Wightman, C. and F.J. Muzzio, *Mixing of granular material in a drum mixer undergoing rotational and rocking motions I. Uniform particles.* Powder Technology, 1998. **98**(2): p. 113-124.

50. Wightman, C., et al., *The structure of mixtures of particles generated by time-dependent flows.* Powder technology, 1995. **84**(3): p. 231-240.

51. Wightman, C., F.J. Muzzio, and J. Wilder, *A quantitative image analysis method for characterizing mixtures of granular materials.* Powder Technology, 1996. **89**(2): p. 165-176.

52. Santomaso, A., M. Olivi, and P. Canu, *Mechanisms of mixing of granular materials in drum mixers under rolling regime.* Chemical Engineering Science, 2004. **59**(16): p. 3269-3280.

53. Brone, D., A. Alexander, and F. Muzzio, *Quantitative characterization of mixing of dry powders in V-blenders.* AIChE journal, 1998. **44**(2): p. 271-278.

54. Susana, L., P. Canu, and A. Santomaso, *Development and characterization of a new thief sampling device for cohesive powders.* International journal of pharmaceutics, 2011. **416**(1): p. 260-267.

55. Mendez, A.S., G. de Carli, and C.V. Garcia, *Evaluation of powder mixing operation during batch production: application to operational qualification procedure in the pharmaceutical industry.* Powder Technology, 2010. **198**(2): p. 310-313.

56. Alizadeh, E., et al., *Experimental investigation of solid mixing and segregation in a tetrapodal blender.* Chemical Engineering Science, 2013. **97**: p. 354-365.

57. Muzzio, F., et al., *Sampling and characterization of pharmaceutical powders and granular blends.* International journal of pharmaceutics, 2003. **250**(1): p. 51-64.

58. Muzzio, F.J., et al., *Sampling practices in powder blending.* International journal of pharmaceutics, 1997. **155**(2): p. 153-178.

59. Vanarase, A.U., et al., *Development of a methodology to estimate error in the on-line measurements of blend uniformity in a continuous powder mixing process.* Powder technology, 2013. **241**: p. 263-271.

60. Hailey, P., et al., *Automated system for the on-line monitoring of powder blending processes using near-infrared spectroscopy part I. System development and control.* Journal of Pharmaceutical and Biomedical Analysis, 1996. **14**(5): p. 551-559.

61. Sekulic, S.S., et al., *Automated system for the on-line monitoring of powder blending processes using near-infrared spectroscopy: Part II. Qualitative approaches to blend evaluation.* Journal of pharmaceutical and biomedical analysis, 1998. **17**(8): p. 1285-1309.

62. El-Hagrasy, A.S., F. D'Amico, and J.K. Drennen, *A Process Analytical Technology approach to near-infrared process control of pharmaceutical powder blending. Part I: D-optimal design for characterization of powder mixing and preliminary spectral data evaluation.* Journal of pharmaceutical sciences, 2006. **95**(2): p. 392-406.

63. El Hagrasy, A.S., S.-Y. Chang, and S. Kiang, *Evaluation of risk and benefit in the implementation of near-infrared spectroscopy for monitoring of lubricant mixing.* Pharmaceutical development and technology, 2006. **11**(3): p. 303-312.

64. Berntsson, O., et al., *Quantitative in-line monitoring of powder blending by near infrared reflection spectroscopy.* Powder Technology, 2002. **123**(2-3): p. 185-193.

65. Scheibelhofer, O., et al., *Spatially resolved monitoring of powder mixing processes via multiple NIR-probes.* Powder technology, 2013. **243**: p. 161-170.

66. Ufret, C. and K. Morris, *Modeling of powder blending using on-line near-infrared measurements.* Drug development and industrial pharmacy, 2001. **27**(7): p. 719-729.

67. Bellamy, L.J., A. Nordon, and D. Littlejohn, *Real-time monitoring of powder mixing in a convective blender using non-invasive reflectance NIR spectrometry.* Analyst, 2008. **133**(1): p. 58-64.

68. Vanarase, A.U., et al., *Real-time monitoring of drug concentration in a continuous powder mixing process using NIR spectroscopy.* Chemical Engineering Science, 2010. **65**(21): p. 5728-5733.

69. Arratia, P., et al., *Characterizing mixing and lubrication in the Bohle Bin blender.* Powder Technology, 2006. **161**(3): p. 202-208.

70. Duong, N.-H., et al., *A homogeneity study using NIR spectroscopy: tracking magnesium stearate in Bohle bin-blender.* Drug development and industrial pharmacy, 2003. **29**(6): p. 679-687.

71. Mehrotra, A. and F.J. Muzzio, *Comparing mixing performance of uniaxial and biaxial bin blenders.* Powder Technology, 2009. **196**(1): p. 1-7.

72. Chester, A.W., et al., *Mixing dynamics in catalyst impregnation in double-cone blenders.* Powder Technology, 1999. **102**(1): p. 85-94.

73. Zhang, W., et al., *Application of electrical capacitance tomography in particulate process measurement–A review.* Advanced Powder Technology, 2014. **25**(1): p. 174-188.

74. Huang, A.-N. and H.-P. Kuo, *Developments in the tools for the investigation of mixing in particulate systems–a review.* Advanced Powder Technology, 2014. **25**(1): p. 163-173.

75. Nakagawa, M., et al., *Non-invasive measurements of granular flows by magnetic resonance imaging.* Experiments in fluids, 1993. **16**(1): p. 54-60.

76. Hill, K., A. Caprihan, and J. Kakalios, *Axial segregation of granular media rotated in a drum mixer: Pattern evolution.* Physical Review E, 1997. **56**(4): p. 4386.

77. Hill, K.M., A. Caprihan, and J. Kakalios, *Bulk segregation in rotated granular material measured by magnetic resonance imaging.* Physical Review Letters, 1997. **78**(1): p. 50.

78. Metcalfe, G., et al., *Measurement of particle motions within tumbling granular flows.* Chaos: An Interdisciplinary Journal of Nonlinear Science, 1999. **9**(3): p. 581-593.

79. Ristow, G.H. and M. Nakagawa, *Shape dynamics of interfacial front in rotating cylinders.* Physical Review E, 1999. **59**(2): p. 2044.

80. Metcalfe, G. and M. Shattuck, *Pattern formation during mixing and segregation of flowing granular materials.* Physica A: Statistical Mechanics and its Applications, 1996. **233**(3-4): p. 709-717.

81. Nguyễn, T.T., et al., *Segregation in horizontal rotating cylinders using magnetic resonance imaging.* Physical Review E, 2011. **84**(1): p. 011304.

82. Jones, J., D. Parker, and J. Bridgwater, *Axial mixing in a ploughshare mixer.* Powder technology, 2007. **178**(2): p. 73-86.

83. Kuo, H., et al., *Solids circulation and axial dispersion of cohesionless particles in a V-mixer.* Powder Technology, 2005. **152**(1-3): p. 133-140.

84. Martin, T., J. Seville, and D. Parker, *A general method for quantifying dispersion in multiscale systems using trajectory analysis.* Chemical engineering science, 2007. **62**(13): p. 3419-3428.

85. Rafiee, M., et al., *Development of positron emission particle tracking for studying laminar mixing in Kenics static mixer.* Chemical Engineering Research and Design, 2013. **91**(11): p. 2106-2113.

86. Marigo, M., et al., *Application of Positron Emission Particle Tracking (PEPT) to validate a Discrete Element Method (DEM) model of granular flow and mixing in the Turbula mixer.* International journal of pharmaceutics, 2013. **446**(1-2): p. 46-58.

87. Portillo, P.M., et al., *Investigation of the effect of impeller rotation rate, powder flow rate, and cohesion on powder flow behavior in a continuous blender using PEPT.* Chemical Engineering Science, 2010. **65**(21): p. 5658-5668.

88. Yang, Z., et al., *Multiple-particle tracking—an improvement for positron particle tracking.* Nuclear Instruments and Methods in Physics Research Section A: Accelerators, Spectrometers, Detectors and Associated Equipment, 2006. **564**(1): p. 332-338.

89. Larachi, F., J. Chaouki, and G. Kennedy, *3-d mapping of solids flow fields in multiphase reactors with rpt.* AIChE Journal, 1995. **41**(2): p. 439-443.

90. Cassanello, M., et al., *Experimental characterization of the solid phase chaotic dynamics in three-phase fluidization.* Industrial & engineering chemistry research, 1995. **34**(9): p. 2971-2980.

91. Alizadeh, E., et al., *Characterization of mixing and size segregation in a rotating drum by a particle tracking method.* AIChE Journal, 2013. **59**(6): p. 1894-1905.

92. Dubé, O., et al., *Dynamics of non-spherical particles in a rotating drum.* Chemical Engineering Science, 2013. **101**: p. 486-502.

93. Sherritt, R.G., et al., *Axial dispersion in the three-dimensional mixing of particles in a rotating drum reactor.* Chemical Engineering Science, 2003. **58**(2): p. 401-415.

94. Doucet, J., F. Bertrand, and J. Chaouki. *Flow Structure Mapping Of Segregating Granular Mixtures Using Radioactive Particle Tracking*. in *The 2007 Annual Meeting*. 2007.

95. Doucet, J., F. Bertrand, and J. Chaouki, *An extended radioactive particle tracking method for systems with irregular moving boundaries.* Powder Technology, 2008. **181**(2): p. 195-204.

96. Rasouli, M., F. Bertrand, and J. Chaouki, *A multiple radioactive particle tracking technique to investigate particulate flows.* AIChE Journal, 2015. **61**(2): p. 384-394.

97. Rasouli, M., et al., *Investigating the dynamics of cylindrical particles in a rotating drum using multiple radioactive particle tracking.* AIChE Journal, 2016. **62**(8): p. 2622-2634.

98. Nakagawa, M., et al., *NMRI study: asial migration of radially segregated core of granular mixtures in a horizontal rotating cylinder.* Chemical Engineering Science, 1997. **52**(23): p. 4423-4428.

99. Cantelaube, F. and D. Bideau, *Radial segregation in a 2d drum: an experimental analysis.* EPL (Europhysics Letters), 1995. **30**(3): p. 133.

100. Rapaport, D., *Radial and axial segregation of granular matter in a rotating cylinder: A simulation study.* Physical Review E, 2007. **75**(3): p. 031301.

101. Thomas, N., *Reverse and intermediate segregation of large beads in dry granular media.* Physical Review E, 2000. **62**(1): p. 961.

CHAPTER 6 ARTICLE 3: DEHYDRATION OF LITHIUM DIHYDROGENPHOSPHATE IN A BALL-MILL ROTARY-KILN REACTOR

Bahman Yari, Pierre Sauriol, Jamal Chaouki[3]

Department of Chemical Engineering, Polytechnique Montreal, C.P. 6079, Succ. Centre-Ville, Montreal, Quebec H3C 3A7, Canada

Submitted to AICHE journal

6.1 Abstract

Lithium dihydrogenphosphate (LHP) needs to be dehydrated in order to be safely applied for the melt casting process to produce lithium iron phosphate (LFP). The dehydration reaction consists of several consecutive melting, oligomerization and crystallization steps resulting in a solid product stuck to the reaction vessel at around 400 °C. Here we applied an electrical shell-heated rotary kiln containing grinding media (ball-mill rotary-kiln, BaMRoK) to dehydrate LHP at 400 °C and recover the ground product without needing any extra processing. The bulk convective heat transfer coefficient of the kiln has been calculated in the presence of the grinding media, and the temperature profile has been modelled using COMSOL Multiphysics. Kinetic model of the reaction from thermogravimetric analysis (TGA) and the thermal profile suggest that the dehydration reaction mostly happens on the internal surface of the rotary kiln wall.

Keywords: LiH_2PO_4, $LiPO_3$, thermal decomposition, dehydration, ball-mill-rotary-kiln, heat transfer

[3] Corresponding author: jamal.chaouki@polymtl.ca; +1-514-340-4711 x4034

6.2 Introduction

The lithium-ion batteries' global market has experienced dramatic growth from 3 billion dollars in 2000 to over 20 billion dollars in 2017 (Pillot, 2012; Workman, 2019). This is in part due to the introduction of such batteries in plug-in hybrid and electric vehicles since 2009 (Pillot, 2012). This new market gives rise to the demand for safe lithium-ion batteries (LIBs) with high specific energy and long life-span but requires that the safety of this type of battery improve and its production costs can be reduced. Lithium iron phosphate ($LiFePO_4$, LFP) is one of the cathode materials used in the LIBs for the automotive industry. Battery producers like BYD, CATL, and Lishen use LFP as the cathode material for the batteries manufactured for electric vehicles (EVs) and plug-in EVs (PHEVs) like BYD and Geely (Pelegov & Pontes, 2018). Studies show that LFP has a much smaller (<0.1%) self-heating rate compared to other common oxide type cathode material (Kvasha et al., 2018; Xuan Liu et al., 2016) resulting in safer LIBs.

During the two decades after its first introduction as cathode material by Padhi et al. in 1997 (A. K. Padhi, K. Nanjundaswamy, & J. Goodenough, 1997), LFP has been synthesized by different methods in industrial as well as laboratory scale (Arnold et al., 2003; J. Chen & Whittingham, 2006; L. Gauthier et al., 2009b; M. Gauthier et al., 2010; Jugović & Uskoković, 2009; MacNeil et al., 2010; Nan, Lu, Chen, Peng, & Li, 2011; C. Xu, Lee, & Teja, 2008; S. Yang, Zavalij, & Whittingham, 2001). The melt casting method for the production of LFP reacts sources of lithium, iron, and phosphate from a wide range of reactants in the molten phase under inert/reducing atmosphere to produce high purity LFP. The application of commodity-grade reactants and the lack of aqueous phase in the process can decrease the production cost of LFP in comparison with other methods. However, most of the reactants considered for this method release large amounts of gases upon fast decomposition reactions at the reaction temperature (around 1000 °C) in molten phase. This is an issue for the scale-up of the process, especially for continuous production.

Dehydration of lithium dihydrogenphosphate (LHP) was studied as a typical degassing reaction of the reactants of the melt casting process for LFP production. The product of this dehydration reaction, lithium metaphosphate (LPO or $LiPO_3$), can be used as a precursor for the melt casting of LFP as it produces no gas during the process and it is a denser source of lithium and phosphorus increasing the bulk density of the reactant mixture and lowering the total mass and volume required

for the synthesis, e.g., more LFP can be produced for a given batch volume (Equations 6.1 and 6.2). Successful application of $LiPO_3$ for the synthesis of LFP through melt casting has been reported previously (M Talebi-Esfandarani et al., 2016).

$$2\ LiH_2PO_4 + Fe_2O_3 + C \longrightarrow 2\ LiFePO_4 + 2\ H_2O\ (g) + CO\ (g) \quad (6.1)$$

$$2\ LiPO_3 + Fe_2O_3 + C \longrightarrow 2\ LiFePO_4 + CO\ (g) \quad (6.2)$$

$LiPO_3$ is also finding new applications for the production of the next generation of LIBs with solid electrolytes (Hockicko et al., 2014; Kartini et al., 2010; Muñoz et al., 2008). This phosphate glass, as like as other types of glasses, namely oxides, doped oxides, sulphides, fluorides, and quenched glasses, have long been known as potential solid electrolytes for high energy density batteries (Ravaine, 1980). Due to the lack of grain boundaries, weak electronic contribution to the conductivity, plasticity, and possibility of manufacturing them in thin-film configuration, they can serve as the ideal replacement for traditional non-aqueous liquid electrolytes adding the advantage of nonflammability and miniaturization. However, it wasn't until recent years that the first successful lab-scale implementation of glass electrolytes in LIBs was announced by Braga et al. in the research team headed by John Goodenough (M. H. Braga et al., 2017; Maria Helena Braga et al., 2018). Fast charging LIBs (in the order of a few minutes), with long life (more than 20,000 cycles of charge and discharge), high energy density and capacity have been achieved using glass electrolytes. Other applications of $LiPO_3$ includes low-temperature glass to metal seals (Chambers et al., 1989; Peng & Day, 1991; Wei et al., 2001).

6.2.1 Dehydration mechanism

Differential scanning calorimetry (DSC) and thermogravimetric (TG) analyses in the kinetic study of this reaction have shown that the reaction starts with oligomerization at slow kinetics on the surface of solid particles at temperatures below melting point (< 210 °C) and speeds up upon melting at 210 °C (Equation 6.3).

$$y\ LiH_2PO_4\ (s,l) \rightleftarrows\ Li_yH_2P_yO_{3y+1}\ (s) + (y\text{-}1)\ H_2O\ (g) \quad (6.3)$$

The kinetics of this reaction was modelled in our previous study using model-free isoconversional method and model fitting with MATLAB and the results are shown in Table 6.1 (Yari, Sauriol, & Chaouki, 2019). A stable intermediate has been isolated via isothermal TGA at 220 °C for six hours at conversions around 0.6, which is equivalent to an oligomer with y = 2.5 ($Li_5H_4P_5O_{17}$). According to the same kinetic study, this intermediate starts to further oligomerize at higher temperatures and speeds up at around 300 °C upon melting. Finally, the oligomers decompose to $LiPO_3$ and nucleation and crystallization of the solid product results in increasing of the viscosity until it completely solidifies (Equation 6.4).

$$Li_yH_2P_yO_{3y+1}\ (s,l) \rightleftarrows\ y\ LiPO_3\ (s) +\ H_2O\ (g) \qquad (6.4)$$

The reaction steps considered for the kinetic modelling are as follows:

$$LHP(surf,s) \rightarrow 2/5\ L2.5(s) + 3/5\ H2O(g) \qquad (R1a)$$

$$LHP(surf,l) \rightarrow 2/5\ L2.5(s) + 3/5\ H2O(g) \qquad (R1b)$$

$$LHP(bulk) \rightarrow 2/5\ L2.5(s) + 3/5\ H2O(g) \qquad (R2)$$

$$L2.5(s) \rightarrow 5/6\ L3(s) + 1/6\ H2O(g) \qquad (R3)$$

$$L3(s) \rightarrow 3/4\ L4(s) + 1/4\ H2O(g) \qquad (R4)$$

$$L4(s) \rightarrow 4\ LPO(s) + H2O(g) \qquad (R5)$$

Table 6.1 summary of the optimum parameters as fitted (cont'd)

Reaction step	Optimal Ea/R (K)	A (min^{-1})	Reaction model	$\bar{T}_i$ (K)
1a	27 727	9.252×10^{23}	$\frac{-1}{\ln(1-\alpha)}$	460.7
1b	41 168	1.481×10^{35}	$\frac{3(1-\alpha)^{2/3}}{2[1-(1-\alpha)^{2/3}]}$	489.8

Table 6.1 summary of the optimum parameters as fitted (cont'd)

2	22 856	1.943×10^{18}	$(1-\alpha)^2$	534.6
3	37 710	3.243×10^{26}	$\frac{3}{2\left[(1-\alpha)^{-1/3}-1\right]}$	571.4
4	19 452	7.228×10^{13}	$(1-\alpha)^2$	599.3
5	6400	623.2	$\frac{3}{2\left[(1-\alpha)^{-1/3}-1\right]}$	661.6

Same molten phases appear during dehydration of other alkali metal dihydrogenphosphates (Gallagher, 1976). After completion of the dehydration, the product is a hard solid, severely stuck to the surface of the reaction vessel. One way to collect the product is to heat it up to its melting point and quench the melt on an appropriate surface (Money & Hariharan, 2007). This method is an energy-intensive process that dehydrates the dihydrogenphosphate in a furnace with temperatures more than the melting point of the product, followed by rapid quenching of the melt. An extra step of crushing and milling of the product in a separate unit is usually required in this method.

Rotary kiln is a proper choice as a reactor for the dehydration of dihydrogenphosphates, for the following reasons:

- Versatility of accepting various feedstocks from granular solids with different particle sizes to slurries with different solid and liquid parts
- Possibility of providing high temperatures directly from the shell or indirectly through a hot gas.
- Possibility of uniformization of the temperature in the bed by mixing through rotation.

Despite these advantages, formation of the sticky intermediates during the dehydration reaction of dihydrogenphosphates, as described in the previous section, deters the application of rotary kiln for the process of the dehydration of dihydrogenphosphates, because of the issues of mass transfer and the collection of the final product. Here, we propose a new reactor setup for the dehydration of lithium dihydrogenphosphate, named "Ball-mill Rotary-kiln" (BaMRoK), that combines the

processes of heating, mixing and grinding in a single vessel. The advantage of this reactor for the dehydration of LHP (and possibly other dihydrogenphosphates) are as follows:

- Comminution of the primary material, for better mass transfer and more surface reaction (Reactions R1a and R1b)
- Increasing the mass transfer in reactions R2 to R5 by spreading the molten phase on the internal surface of the reactor
- Detachment of the stuck solid product from the internal surface of the reactor without needing to extra heating to the melting point of the product
- Grinding the product to the desired particle size at the same reactor

This dehydration/comminution reactor consists of a regular rotary kiln with or without lifters that is filled to a certain level with proper size grinding media (stainless-steel balls). The role of these balls here is basically to break and disperse the sticky solid product from the internal surface of the kiln. Furthermore, spreading the molten phase and grinding the solid mixture of high-level oligomers before their complete dehydration to $LiPO_3$ decrease the processing time by reducing the mass transfer resistance against the release of water vapour. The resulting product particle size can be as low as 10 micrometres, despite its high Bond ball mill work index (BWI) of 21.6 kWh/t and hardness percentile of 96%.

6.2.2 High-temperature ball milling

Application of high-temperature ball milling as a mechanochemical synthesis method had already been reported for other purposes (El-Eskandarany, 2015; Geng, Geng, & Zhai, 2017; L. Jia, Shao, Lü, Tian, & Han, 2014; Tian, Li, Shao, & Shen, 2018). Consecutive ball milling and solid-state synthesis of $Li_4Ti_5O_{12}$ (LTO) with multi-walled carbon nanotube (MWCNT) have resulted in nanosized anode materials for LIBs with improved electrochemical performance. (Jhan & Duh, 2012) Jia et al. have reported that high-temperature ball milling can significantly reduce the process temperature and time for solid-state reactions because it provides mechanical energy and heat at the same time to the reactants. Ball milling during calcination prevented the problematic aggregation which was common in traditional synthesis, eliminating the need for a long time

grinding that destroyed the crystal lattice of the product (L. Jia et al., 2014). Cathode and anode materials for LIBs have been prepared by high-temperature ball milling of the solid precursors at reduced temperatures and in less time compared to corresponding traditional solid-state syntheses (Geng et al., 2017; Tian et al., 2018). Table 6.2 shows the advantages of the application of ball milling in a variety of processes from solid-state syntheses to mechanical alloying and refining of metals from their ore.

Table 6.2 Applications of ball milling in chemical processes and their advantages over corresponding traditional processes (cont'd)

Process	**Product**	**Reference**	**Temperature and/or time**		**Other advantages**
			Traditional method	**Mechanochemical method**	
Solid-state synthesis	(Y,Gd)BO3:Eu 3+ phosphor	(L. Jia et al., 2014)	Solid-state synthesis, 1000 °C, for 4-5 hours	High-temperature ball milling, 600 °C, for 2 hours	The better crystal lattice of the product
	Lithium manganese oxide (cathode material for LIBs)	(Geng et al., 2017)	Solid-state synthesis, 800 °C, for 24 hours	High-temperature ball milling, 600 °C, for 2 hours	Nano-sized product, better electrochemical performance
	lithium titanate (anode material for LIBs)	(P. Jia, Shao, & Liu, 2014; L. Wang, Zhang, Liang,	Solid-state synthesis, 800 °C, for 6 hours	High-temperature ball milling,	Micron-sized powder with high electrochemic

Table 6.2 Applications of ball milling in chemical processes and their advantages over corresponding traditional processes (cont'd)

Process	Product	Reference	Temperature and/or time		Other advantages
			Traditional method	Mechanochemical method	
		Ou, & Xu, 2012)		750 °C, for 3.5 hours	al performance
	Lithium nickel manganese cobalt oxide (cathode material for LIBs)	(Bang, Mumm, Park, & Song, 2012; Dou & Wang, 2011; Tian et al., 2018)	Solid-state synthesis, 900 °C, for 12 hours 800 °C, for 40 hours	High-temperature ball milling, 750 °C, for 12 hours	Micron-sized powder with high electrochemical performance
Alloying	Metallic alloys, e.g., INCONEL alloy MA 6000	(J. Benjamin, 1976; J. S. Benjamin, 1990)	Melting, Typically, more than the melting point of metals (e.g., Nickel: 1455 °C)	Mechanical alloying, Ambient temperature (typically, 25 °C) ball milling	Possibility of alloying far apart melting point metals

Table 6.2 Applications of ball milling in chemical processes and their advantages over corresponding traditional processes (cont'd)

Process	Product	Reference	Temperature and/or time		Other advantages
			Traditional method	Mechanochemical method	
Non-equilibrium alloying	metastable superalloys	(Froes, Suryanarayana, Taylor, Ward-Close, & Goodwin, 1996; Suryanarayana, 2001)	Energizing to molten or vapour form and rapid quenching, Typically, more than the melting point of metals	Mechanical alloying (ambient temperature ball milling) 25 °C	No need for super rapid cooling in the order of 10^5 – 10^8 K/s
Metal refining by solid-state reduction	Metallic copper, from copper oxide (CuO) and calcium	(McCormick, 1995)	Typically, more than the melting point of metals (e.g., copper: 1085 °C)	Ambient temperature ball milling 25 °C	

The hydrodynamics of the balls and the reaction material in the BaMRoK reactor was investigated in our previous study (The article submitted to the Powder Technology) for the purpose of ball size selection. Based on this study, particles smaller than a quarter of the ball diameter (like LHP powder), become segregated at the vicinity of the internal surface of the reactor wall, where they experience higher temperature. On the other hand, particles bigger than this size ratio (like LPO chunks that are detached from the wall) become segregated at the core region of the bed of the balls. Particles around this size ratio or near the ball size, become less segregated and appear more uniformly between the balls.

In this paper, we present the BaMRoK reactor for the dehydration process of LHP in a reduced temperature than the common melt quenching method. The heat transfer in this reactor is studied to obtain the temperature profiles of the balls and the internal surface of the reactor by direct temperature measurements, modelling by COMSOL Multiphysics and optimization by MATLAB. These temperature profiles were used in our kinetic model to calculate the reaction rate and the results were compared to the experimental data for the dehydration of LHP in the BaMRoK reactor. The quantitative recovery and the chemical and physical quality of the product was also analyzed by XRD, RAMAN and PSD.

6.3 Materials and methods

Industrial battery-grade LHP with 99.5 % purity and general particle size distribution of 250 to 350 µm, supplied in 30 kg hermetic bags, (Sichuan Tianqi Lithium Industries Inc., China) was used as the primary material. Liquid nitrogen, by MEGS Specialty Gases, Inc., Canada, was used to supply the carrier gas with less than 0.5 ppm oxygen and less than 0.5 ppm water content. STTR-1200C-8-30 rotary kiln equipped with high-temperature metallic heating elements, type-K thermocouple at the outer surface of the cylinder, and Yudian temperature controller was supplied by Sentro Tech Corp., Strongsville OH, USA (Figure 6.1a).

Another K-type thermocouple was added to the exit point of the carrier gas (shown as T in Figure 6.2) that could register the gas temperature every second using Labjack U3-LV analog to digital converter and Labview software. This 12-kW rotary kiln with a cylindrical furnace of 20 cm

diameter and 75 cm heating zone length, could heat up to a maximum temperature of 1200 °C with a maximum heating rate of 8 °C/min and could rotate with a maximum rate of 32 rpm after modification of the gearbox.

Another modification to the rotary kiln was done by the installation of 4 lifter bars of 75 cm × 2.5 cm dimensions, all along the heating zone, 90° spaced from each other (Figure 6.1b), adjusted in a way to maintain the rolling regime in the operating rotation rate. The grinding media used in the rotary kiln were AISI 52100 Chrome steel balls with 2.54 cm diameter, provided by Glen Mills Inc., Clifton NJ, USA. The ball size was selected to ensure that material would be in greater contact with the rotary-kiln wall based on the results of our segregation studies in rotating drums (The article submitted to the Powder Technology). EI1050 digital temperature/humidity probe that was used for monitoring the outlet carrier gas humidity and the temperature was supplied by Labjack corporation, Lakewood CO, USA.

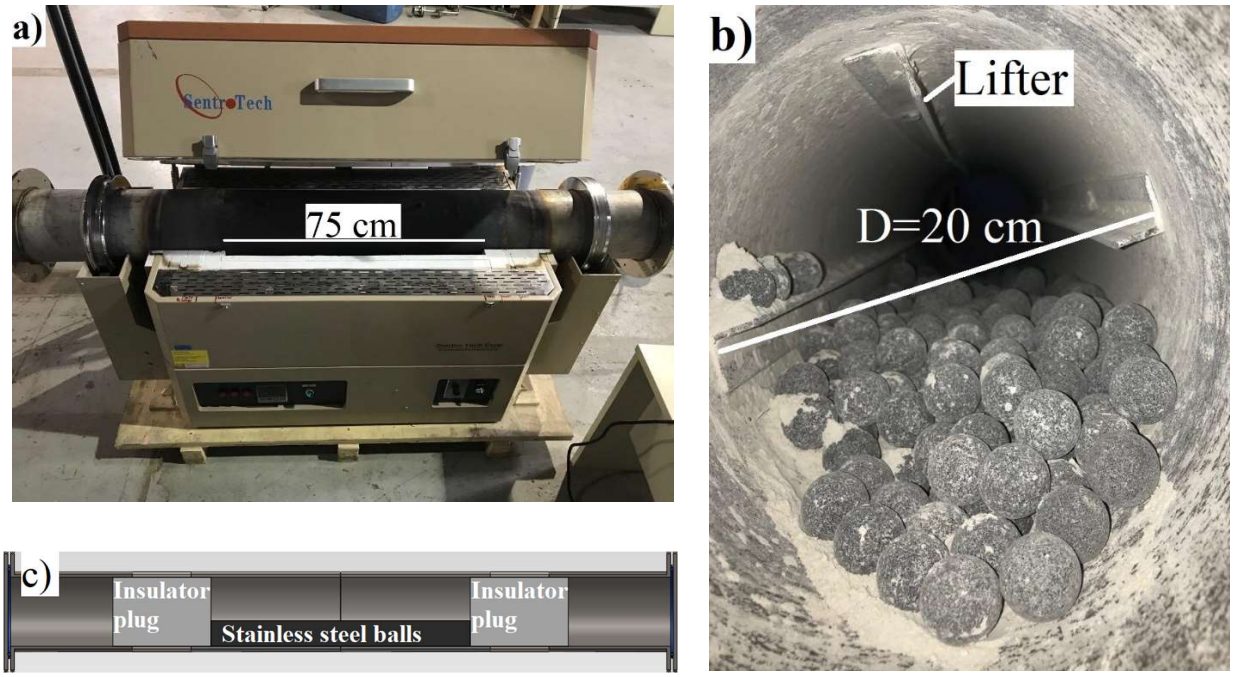

Figure 6.1 Pictorial and graphic views of the BaMRoK used in the experiments. (a) Side view, (b) Internal view of the cylindrical kiln, showing stainless steel balls with 2.5 cm diameter and the white powder product (dehydrated LHP), and (c) Graphic axial cross section

For heat transfer studies, different strategies including direct measurement at steady-state and during heating, and modeling using COMSOL Multiphysics were applied to have an estimate of the temperature difference between the set/measured temperature on the outer surface of the cylinder, the temperature of the internal surface of the cylinder, and that of the balls. The experimental setup used for these studies is schematically shown in Figure 6.2.

For the dehydration process, 0.2 kg of LHP was loaded to the ball mill-rotary kiln explained in this section. The temperature was raised with 5 °C/min to 500 °C and set for an isothermal for 1 h with carrier gas flow of 30 SLPM and rotation rate of 13 rpm. 45 kg of 2.5-cm stainless steel balls were also charged to the kiln to fill 35% of the operating volume.

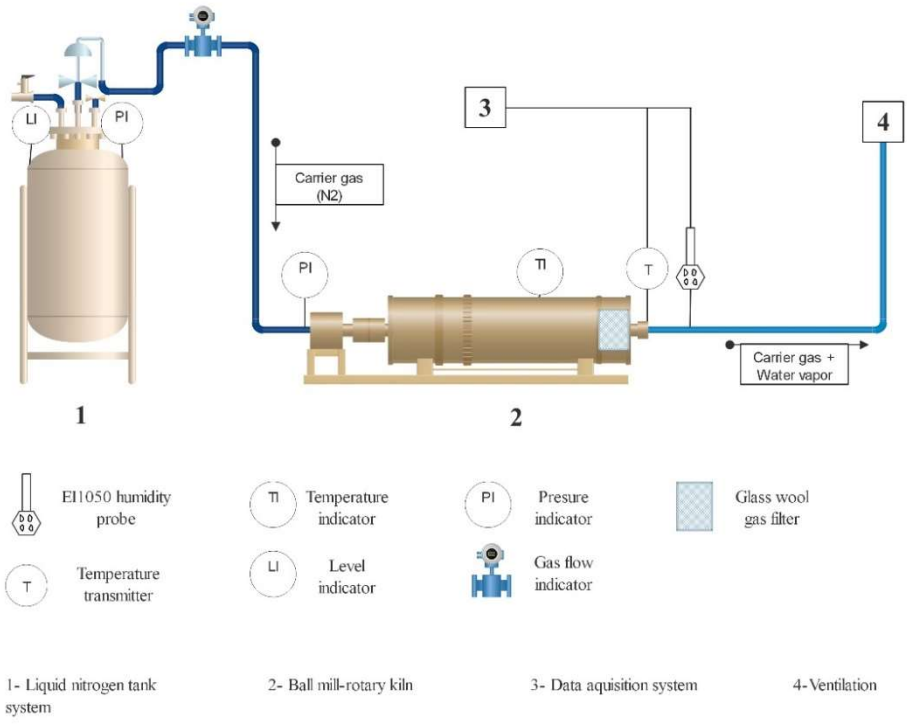

Figure 6.2 Schematic diagram of the experimental setup

The final product was characterized by X-ray diffraction (XRD). The XRD was performed with a Philips X'Pert diffractometer (Now Panalytical B.V., The Netherlands) with Cu Kα radiation

(0.154 nm) at a generator voltage of 50 kV and a current of 40 mA. The scanning rate was 0.02°/s, with a resolution of 0.02°.

For Raman characterization, we used a WITec alpha300 access confocal Raman microscope equipped with a motorized stage, CCD detector, and 1800 grooves/mm optical grating. The light source was a 532 nm Cobolt laser with 25 mW power. The spectra were obtained at 514 nm excitation wavelength, with 50x collecting lens, and 10 seconds for signal integration time.

The TGA tests were performed using a TA Instruments Q-5000, under a 40 mL/min nitrogen flow, with approx. 15 mg of the sample at 400 °C to measure the residual water in the product.

The particle size distribution of the produced $LiPO_3$ from ball mill-rotary kiln was measured using MicroBrook EyeTech laser obstruction analyzer with ACM-112 dry-powder free fall measurement cell and A-100 laser channel lens. Measurements were performed in three cycles of 60 s in 25 °C.

6.4 Results and discussion

In this section, direct measurements and computer modelling results are presented to estimate the radial temperature gradient at steady-state and constant rate heating period (unsteady state) of BaMRoK reactor without reaction. The effect of reaction heat was negligible compared to the total heat transfer. The temperature of the balls was uniform in the radial direction and in axial direction except for the extremities (near the end plugs). Therefore, three temperatures were considered as the temperature gradient in the radial direction as the rotary kiln temperature-controller set point (based on the thermocouple near the outer surface of the rotary kiln), the temperature of the internal surface of the rotary kiln and the temperature of the surface of the stainless-steel balls.

6.4.1 Temperature profile at steady state

Two procedures were used to measure and verify the temperature of the internal surface of the kiln and the balls at four steady-state isotherms.

Procedure 1: In 4 different cases, the external surface temperature of the cylinder was set to 260 °C, 270 °C, 450 °C, and 470 °C, with 1 h holding time, after filling it to 35% of the volume with 2.5 cm balls. The internal surface of the cylinder and surface temperature of the balls were

measured remotely using an infrared thermometer and by contacting the thermocouple tip to the targeted surfaces. For these measurements, we stopped the rotation, opened the plugs of the cylinder temporarily and measured the temperature rapidly, with the whole stopping time of less than 1.5 min. These temperatures were selected because firstly they were in the range of the dehydration process, we were aiming to perform, and secondly, they were just around the melting point of the materials that we were going to use in the next procedure to evaluate the temperature inside the balls.

Procedure 2: To verify the measured temperature of the balls, 2 sets of 5 balls of diameter 2.5 cm, were diagonally drilled with a 3.175-mm drill bit (Figure 6.3), filled with tin filings (m.p. 232 °C) (in the first set of balls) and zinc filings (m.p. 419.5 °C) (in the second set of balls) and sealed with LOCTITE EA 3463 metallic putty. Then the balls of the first set were used in the experiments of the first procedure at temperatures 260 °C and 270 °C and those of the second set at temperatures 450 °C and 470 °C.

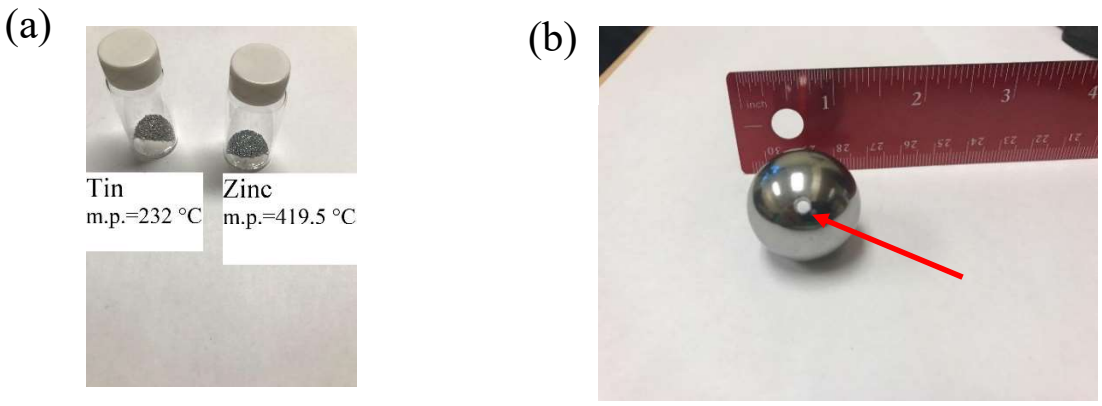

Figure 6.3 (a) Tin and zinc filings and (b) drilled ball used for temperature verification with procedure 2

Table 6.3 Results of the direct measurements of the temperatures of the internal surface of the cylinder and the surface of the stainless-steel balls based on procedures 1 and 2

Rotary kiln temperature-controller set point (°C)	**The temperature of the internal surface of the rotary kiln (°C)**	**The temperature of the surface of the stainless-steel balls (°C)**	**Metal filing used inside the balls for verification**	**The physical condition of the metal filing**
260	239	228	Tin	Sintered
270	248	238	Tin	Molten
450	420	405	Zinc	Sintered
470	438	422	Zinc	Molten

After cooling, the balls were re-drilled to see if the material inside them has melted verifying that the temperature of the balls has passed the melting point of the material.

The results of these measurements are shown in Table 6.3. The melting of the filings inside the balls at measured ball surface temperatures of 238 °C and 422 °C and the sintering at 228 °C and 405 °C, ensured the uniformity of the balls' temperature throughout the bed.

6.4.2 Direct measuring and modelling of the temperature profile at the unsteady state

With a 35% bulk volumetric load of balls (without reactive material), the kiln was heated with a 5 °C/min on the external surface while rotating at 13 rpm. Then the rotation was interrupted every 6 min during the heating, for direct measurement of the temperature on the surface of the internal wall and the balls at the central part of the kiln using an infrared thermometer and by contacting the K-type thermocouple to the surface for 1 min. The two methods of measurements were in good agreement at temperatures above 200 °C with around 2% offset. An effective bulk convective heat

transfer coefficient ($h_{eff.}$) between the internal surface of the kiln and the balls in contact was estimated. This approach lumps the radiative heat transfer and losses contribution within this unique h_{eff}.

By general assumption of the equality of the convective heat transfer from the internal surface of the wall to the balls ($dQ/dt = hA(T_{wall\_in} - T_{balls})$) with the heat that increases the temperature of the balls ($dQ/dt = m_{balls}C_{p_{balls}}\, dT_{balls}/dt$), the instantaneous and average h_{eff} (effective bulk convective heat transfer coefficient) was calculated by plotting the time derivative of the temperature of the balls (dT_{balls}/dt) versus the temperature difference between the internal wall and the balls ($T_{wall\_in} - T_{ball}$), using the surface temperatures of the internal wall and the balls that were measured by time.

A 2D model for the temperature profile was created via COMSOL Multiphysics using the calculated h_{eff}, and by optimization of other significant heat-transfer parameters affecting the model in MATLAB. These parameters are as follows:

1. Convective heat transfer coefficient from the external wall
2. Radiation heat transfer (emissivity) of the external wall
3. Convective heat transfer coefficient from the internal wall to the balls (based on the surface in contact with the bulk)
4. Radiation heat transfer (emissivity) of the balls
5. Heat loss from the external wall (assuming a 20-cm-long fin in COMSOL to simulate)
6. Heat loss from the balls (assuming a 20-cm long fin in COMSOL to simulate)

After finding the h, it was used with 5 other estimated parameters in COMSOL to produce the first temperature profiles. The standard errors of these profiles were calculated and fed to the MATLAB for optimization (minimization of the error). Then the new parameters were used in COMSOL to produce the new temperature profile. This process was iterated to obtain a temperature profile with minimum standard error. The final modelled temperature profile is shown in Figure 6.4, and the optimized parameters are presented in Table 6.4.

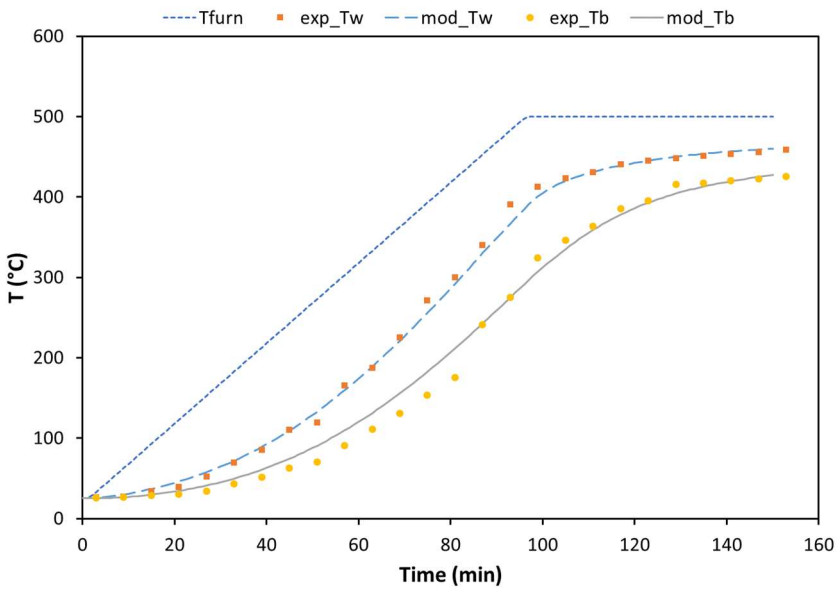

Figure 6.4 Set and measured temperature profiles of external and internal surfaces of the rotary-kiln wall and surface of the balls, and the optimized COMSOL models

Table 6.4 Optimized modelling parameters for heat transfer in the BaMRoK (cont'd)

Parameter	**Definition**	**Optimal value (range)**
h_{out}	Convective heat transfer coefficient from the external wall	5.51 W/m^{2}K (4.94 – 5.99)
ε_{out}	Radiation heat transfer (emissivity) of the external wall	0.87 (0.836 – 0.898)
h_{in}	Convective heat transfer coefficient from the internal wall to the balls (based on the surface in contact with the bulk)	137 W/m^{2}K (129 – 147)
ε_{in}	Radiation heat transfer (emissivity) of the balls	0.64 (0.638 – 0.670)

Table 6.4 Optimized modelling parameters for heat transfer in the BaMRoK (cont'd)

Parameter	Definition	Optimal value (range)
h_{loss_wall}	Heat loss from the external wall	12.8 W/m^{2}K (7.70 – 15.2)
h_{loss_balls}	Heat loss from the balls	11.6 W/m^{2}K (10.6 – 14.6)

Table 6.5 Convective heat transfer coefficient between the wall and the solids in the rotary kiln for different applications

Application	Reference	Material	Particle size	h_{in}
Indirect heating of carbohydrates (potato starch) in a rotary kiln	(G. W. J. Wes, A. A. H. Drinkenburg, & S. Stemerding, 1976)	Potato starch	0.015 -0.1 mm	6989.18 W/m^{2}K
The calcining of sodium bicarbonate in a rotary kiln	(Wachters, 1964.)	Sodium bicarbonate (Soda lime)	0.137 mm	5447.8 W/m^{2}K
Direct heating of minerals in rotary kiln	(Tscheng, 1978)	Ottawa sand, Lime stone	0.51 -1.26 mm	11442.62 W/m^{2}K
Indirectly heated pilot scale rotary kiln	(Njeng, Vitu, Clausse, Dirion, & Debacq, 2018)	Sand	0.550 mm	800 W/m^{2}K

Comparison of the calculated convective heat transfer coefficient from the internal wall to the balls (h_{in}) in the BaMRoK with the same parameter in other applications of rotary kiln in the literature showed a difference of more than one degree of magnitude in most cases (Table 6.5).

The compared cases in Table 6.5 were operated in rolling regime, however the material and their particle size were different with our study that makes such discrepancy between our results and the results presented in those references. The most important factor causing such bigger convective heat transfer coefficient between the kiln wall and the solid material in the references cited in Table 6.5 is the number of contacts between the wall and the particles. To have an idea of the effect of the particle size, the fraction of the solid particles with three different arrangements (square, triangular and hexagonal) was theoretically calculated. At a boundary layer of the order of 1-2 mm and 25 mm spheres as filling material, a fraction of solid in the boundary layer of the order of 6 to 12% was calculated. In comparison, the fine particles treated by the authors of references in Table 6.5 with a typical particle diameter of the order of 100 μm (D / h of 0.1 to 0.05) the theoretical fraction of solids varies between 52 and 74% depending on the arrangement. There is therefore potentially a ratio between the two applications up to an order of magnitude of fraction of solids in the thermal boundary layer that can partially justify the difference between our results and the literature.

6.4.3 The reaction rate of the dehydration of LiH_2PO_4 in the BaMRoK

To monitor the dehydration reaction rate in the BaMRoK, we analyzed the gaseous by-product (water vapour) as the relative humidity (RH) in the carrier gas, downstream of the process. The starting amount of the LiH_2PO_4 and the carrier gas flow for this test was controlled in order to avoid any vapour condensation before and in the RH sensor. Also, the temperature at the RH sensor was monitored to allow conversion of the RH to the equivalent water vapour composition.

The reaction rate was represented as the change in water vapour composition per unit of time. Figure 6.5 shows the comparison of the reaction rate versus time curve obtained from RH measurement to the curves corresponding to the predicted reaction rates obtained from the kinetic

model (Yari et al., 2019) using the modelled temperatures of the internal surface of the kiln (T_{wall}) and the stainless steel balls (T_{balls}) from the previous section.

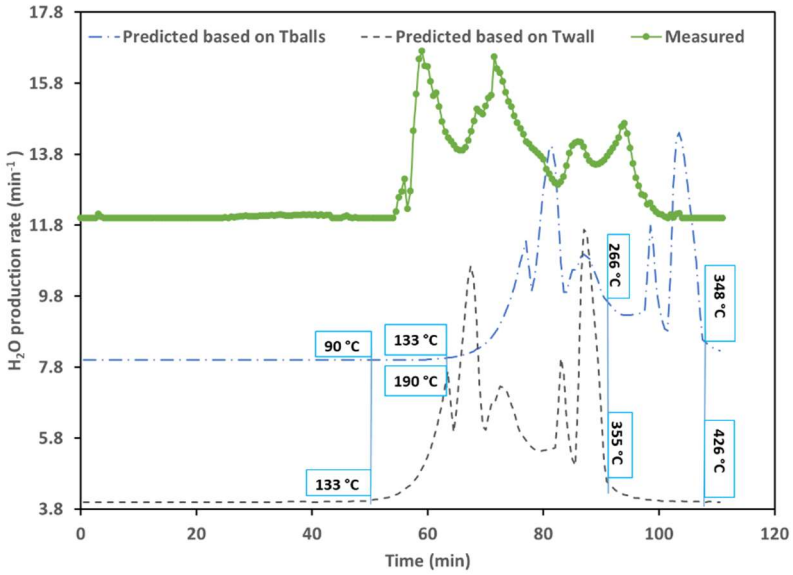

Figure 6.5 Comparison of the measured reaction rate with the predicted reaction rates based on the kinetic model with the modelled temperature profiles (T_{wall} and T_{balls})

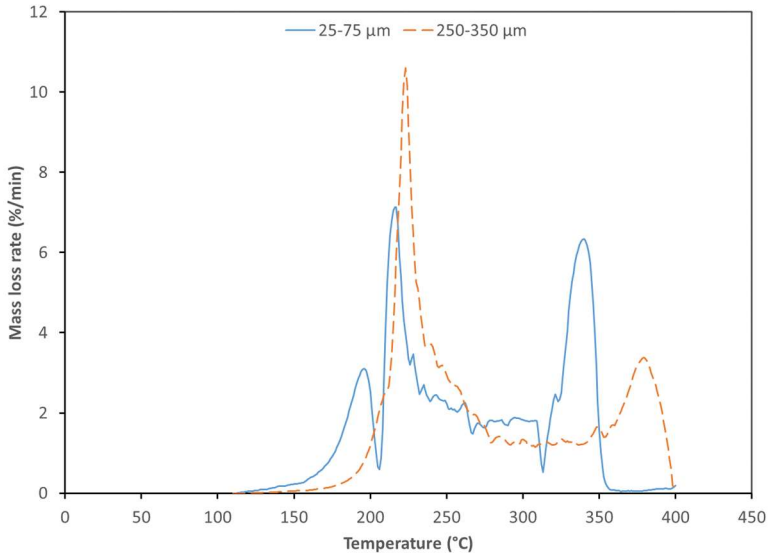

Figure 6.6 Differential thermogravimetric analysis (DTG) of LHP at 5 °C/min with two ranges of particle size (Yari et al., 2019)

The number of peaks in the measured reaction rate is in accordance with the kinetic model predictions. However, the places of the peaks follow closer to the prediction of the kinetic model with the temperature of the internal wall of the rotary kiln. The onset time of the first peak in the measured H_2O production rate (52 min) mostly coincides with that (50 min) of the predicted production rate with the temperature of the kiln-wall internal surface (T_{wall}). The minor discrepancy between these two times (~ 2 min) is because the carrier gas started with 2 min delay, causing an abrupt onset. The temperature of the first peak between 60-62 min (190 °C) is closer to that corresponding to the DTG curve with 25-75 micron particles in figure 6.6. This can be because of the grinding of LHP in the BaMRoK before the start of the reaction.

To better compare the measured reaction rate with predicted reaction rates, the rate curves were translated to the conversion and plotted versus time in figure 6.7. To do so, we calculated the overall released vapour by integrating the reaction rate in time and normalization by dividing to the total final released vapour. Based on these observations, LHP particles experience the temperature of the internal surface of the kiln rather than the temperature of the balls or the temperature of the external surface of the wall. This is also in accordance with the hydrodynamic observations (The

article submitted to the Powder Technology) approving the percolation of the particles to the bottom of the balls.

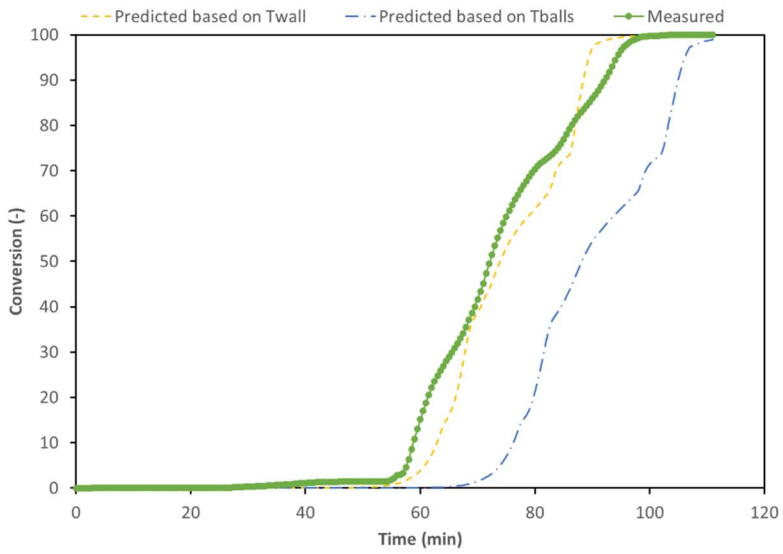

Figure 6.7 Comparison of the measured conversion versus time with the predicted conversions based on measured and modelled temperature profiles

6.4.4 Recovery and characterization of the product

The dehydration of 200 g, 500 g, and 1 kg LHP was performed in three experiments with constant-rate heating to 500 °C (for the 200-g and 500-g cases) and 450 °C (for the 1-kg case) with final isothermal heating and grinding. After cooling the media and the product, the mixture was unloaded and sieved. The isothermal time for the 200-g and 500-g cases was 1 h and the recovered product was 131 g and 334 g respectively (around 80 % recovery). The isothermal time for the 1-kg case was 3 h and the recovered product was 493 g (around 60 % recovery). The unrecovered product was mostly due to the layer of the product that coats the grinding balls, especially for the 1-kg case in which the balls were brand new. In the other two cases, the coated layer remains constant, so the recovery is more than the 1-kg case. Repeating the batch production or continuous production may reduce this source of loss in recovery. The other source of loss is the carryover of the product dust with the carrier gas despite the filter that was used at the exit point. Therefore, using higher efficiency powder filters or cyclonic dust collectors can be considered for reducing this type of loss.

The particle size of the product from the 500-g case was analyzed and had a uniform particle size distribution (PSD) ranging from 5 to 15 µm with a peak at 10 µm (Figure 6.8). This PSD is enough for the application of LFP melt casting and can be adjusted by the grinding time for other purposes.

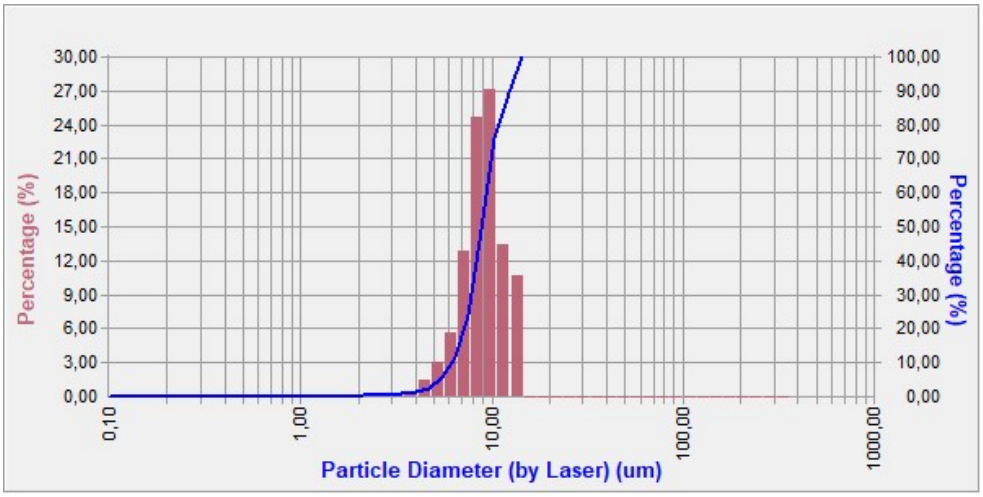

Figure 6.8 Particle size distribution (PSD) analysis results for the LPO produced in the BaMRoK reactor after 1 h grinding with 13 rpm at 500 °C

The peaks in the relative humidity curve in Figure 6.5 show the steps determined in the mechanism of the reaction (Yari et al., 2019). TGA analysis of the product showed no mass loss until the melting point. The average particle size corresponding to this isothermal time with 13 rpm is 10 microns.

The XRD pattern of this product is shown in Figure 6.9 and compared to the XRD of the LPO obtained in a smaller scale for the kinetic study (Yari et al., 2019). The LPO sample shows characteristic peaks at 2θ angles of 16.5°, 18.5°, 25°, 27.5°, which is in agreement with the LPO obtained in a smaller scale in a muffle furnace. The structure is monoclinic with lattice parameters of a = 13.074 Å, b = 5.4068 Å, c = 16.452 Å, with Z = 20, and space group of P2/m (Murashova & Chudinova, 2001). The characteristic peaks of LHP at 17°, 22.5°, and 35° are absent that confirms the complete conversion of LHP.

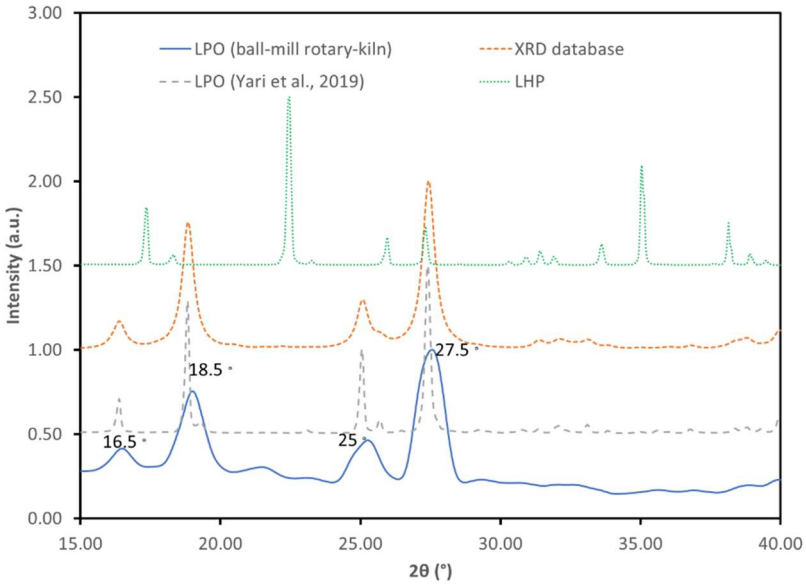

Figure 6.9 Measured and calculated X-ray diffractograms of the product of the dehydration of LHP (LPO) in the BaMRoK

Raman spectra of the product (LPO) and the primary material (LHP) used, were measured at room temperature in the wavenumber range of 100 to 2000 cm^{-1} (Figure 6.10). For LPO, the peaks around 300 cm^{-1}, 700 cm^{-1}, and 1200 cm^{-1} are similar to the peaks of LPO measured at 293 K by Kartini et al. (Kartini et al., 2010). For LHP we have signals related to vibrational modes in the low range (under 500 cm^{-1}) and high range (700 to 1200 cm^{-1}). The low vibrational modes under 300 cm^{-1} correspond to the external vibrational modes of the PO_4 tetrahedra and LiO_4 tetrahedra. However, the internal modes of LiO_4 tetrahedra showed up around 390 to 500 cm^{-1}. The peaks around 900 and 1080 cm^{-1} correspond to the internal vibrational modes of PO_4 tetrahedra (K.-S. Lee, Ko, et al., 2008a). The Raman band at 1390 cm^{-1} is due to the symmetric phosphoryl stretch, (P=O) sym, the band at 640 cm^{-1} is due to the symmetric stretch of the bridging oxygen that link neighbouring tetrahedra, (POP) sym, the bands at 810 cm^{-1} and 910 cm^{-1} are due to asymmetric bridging oxygen stretch, (POP) asym, and the band at 190 cm^{-1} is due to a P-O-P bending mode (Kartini et al., 2010; K.-S. Lee, Ko, Moon, Lee, & Jeon, 2008b; Muñoz-Senovilla & Muñoz, 2014).

6.5 Conclusion

The dehydration of lithium dihydrogenphosphates phosphate in a BaMRoK with material temperatures of 400 °C was successfully performed, and the chemical and physical quality of the product was verified by TGA, XRD, Raman and PSA. The advantage of this process to the conventional melting and quenching process is its lower temperature and combination of the milling stage in the reactor. The recovery of the product can be improved by increasing the scale and further optimization of the process.

Heat transfer in the presence of the balls was also studied by experimental measurements and modelling with COMSOL Multiphysics. Application of the kinetic model to the measured data revealed the segregation of material in the balls which is advantageous for heat transfer however after completion of the reaction the product is broken from the surface of the kiln in bigger chunks that are no more segregated and grinds to the acceptable particle size 10 micron after 3 h of grinding.

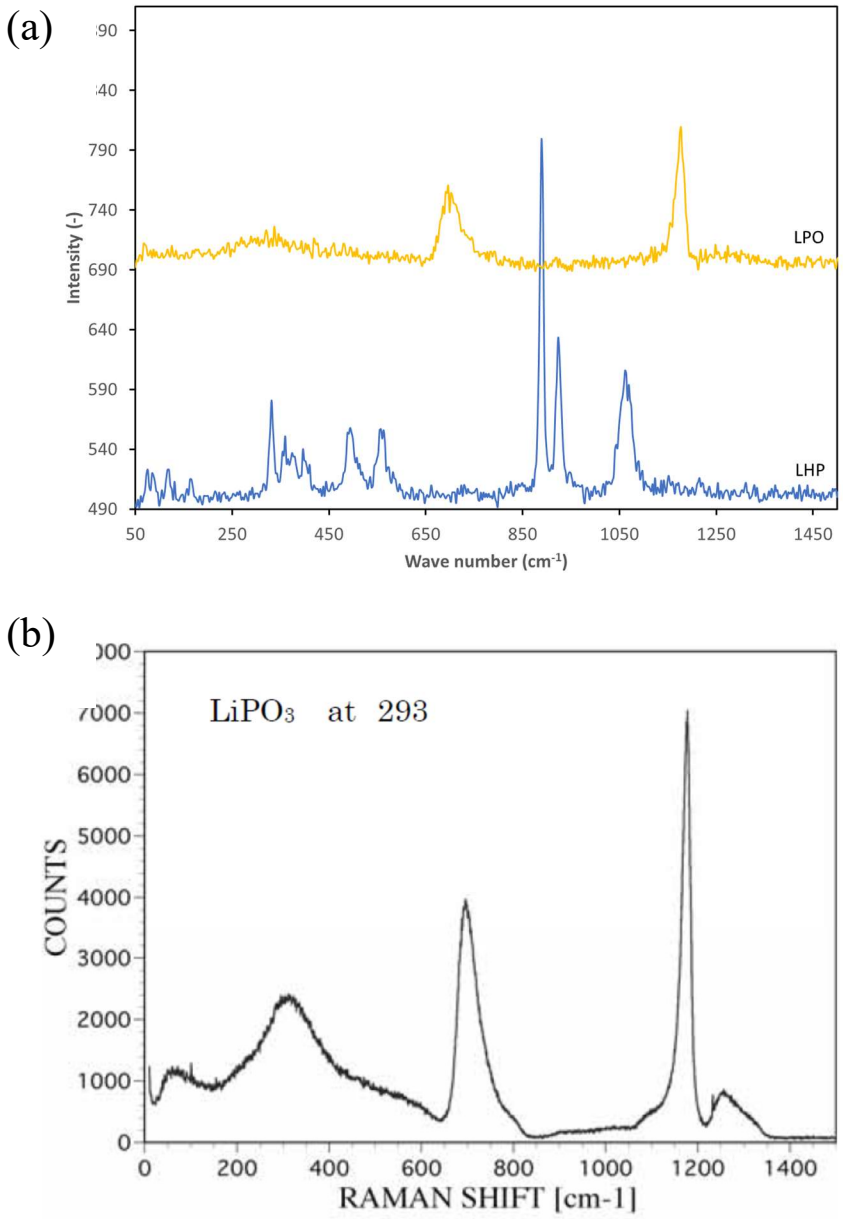

Figure 10 (a) Raman spectra of LHP and its dehydration product (LPO) (b) Raman spectrum of LPO at 293 K from (Kartini et al., 2010)

Acknowledgements

The authors would like to acknowledge the technical support of the staff of the department of chemical engineering of Polytechnique Montreal, Mr. Sylvain Simard Fleury, Mr. Yanik Landry-

Ducharme and Mr. Maxime Beaudoin. The financial support of the Natural Sciences and Engineering Research Council of Canada (NSERC) and the Canada Foundation for Innovation (CFI) through the Automotive Partnership Canada program is gratefully acknowledged. The authors are also appreciative for the financial and technical support from industrial partner Johnson Matthey Battery Materials.

6.6 References

1. Pillot, C., *The worldwide battery market 2011-2025*. 2012, Batteries.
2. Workman, D., *Lithium-Ion Batteries Exports by Country.* http://www.worldstopexports.com/lithium-ion-batteries-exports-by-country/, 2019.
3. Pelegov, D. and J. Pontes, *Main Drivers of Battery Industry Changes: Electric Vehicles—A Market Overview.* Batteries, 2018. **4**(4): p. 65.
4. Kvasha, A., et al., *A comparative study of thermal runaway of commercial lithium-ion cells.* Energy, 2018. **159**: p. 547-557.
5. Liu, X., et al., *Heat release during thermally-induced failure of a lithium-ion battery: impact of cathode composition.* Fire Safety Journal, 2016. **85**: p. 10-22.
6. Padhi, A.K., K. Nanjundaswamy, and J. Goodenough, *Phospho-olivines as positive-electrode materials for rechargeable lithium batteries.* Journal of the electrochemical society, 1997. **144**(4): p. 1188-1194.
7. Arnold, G., et al., *Fine-particle lithium iron phosphate LiFePO 4 synthesized by a new low-cost aqueous precipitation technique.* Journal of Power Sources, 2003. **119**: p. 247-251.
8. Chen, J. and M.S. Whittingham, *Hydrothermal synthesis of lithium iron phosphate.* Electrochemistry Communications, 2006. **8**(5): p. 855-858.
9. Jugović, D. and D. Uskoković, *A review of recent developments in the synthesis procedures of lithium iron phosphate powders.* Journal of Power Sources, 2009. **190**(2): p. 538-544.
10. Nan, C., et al., *Solvothermal synthesis of lithium iron phosphate nanoplates.* Journal of Materials Chemistry, 2011. **21**(27): p. 9994-9996.
11. Xu, C., J. Lee, and A.S. Teja, *Continuous hydrothermal synthesis of lithium iron phosphate particles in subcritical and supercritical water.* The Journal of Supercritical Fluids, 2008. **44**(1): p. 92-97.
12. Yang, S., P.Y. Zavalij, and M.S. Whittingham, *Hydrothermal synthesis of lithium iron phosphate cathodes.* Electrochemistry Communications, 2001. **3**(9): p. 505-508.
13. Gauthier, L., et al., *Process for preparing electroactive insertion compounds and electrode materials obtained therefrom*. 2009, Google Patents.

14. Gauthier, M., et al., *Melt casting LiFePO4 I. Synthesis and characterization.* Journal of the Electrochemical Society, 2010. **157**(4): p. A453-A462.

15. MacNeil, D., et al., *Melt Casting LiFePO4 II. Particle Size Reduction and Electrochemical Evaluation.* Journal of The Electrochemical Society, 2010. **157**(4): p. A463-A468.

16. Talebi-Esfandarani, M., et al., *LiFePO4 synthesized via melt synthesis using low-cost iron precursors.* Journal of Solid State Electrochemistry, 2016. **20**(7): p. 1821-1829.

17. Hockicko, P., et al. *Electrical properties of LiPO 3 glasses*. in *2014 ELEKTRO*. 2014. IEEE.

18. Kartini, E., et al., *Recent studies on lithium solid electrolytes (LiI) x (LiPO3) 1-x for secondary battery.* Journal of the Physical Society of Japan, 2010. **79**(Suppl. A): p. 54-58.

19. Muñoz, F., et al., *Increased electrical conductivity of LiPON glasses produced by ammonolysis.* Solid State Ionics, 2008. **179**(15-16): p. 574-579.

20. Ravaine, D., *Glasses as solid electrolytes.* Journal of Non-Crystalline Solids, 1980. **38**: p. 353-358.

21. Braga, M., et al., *Alternative strategy for a safe rechargeable battery.* Energy & Environmental Science, 2017. **10**(1): p. 331-336.

22. Braga, M.H., et al., *Nontraditional, safe, high voltage rechargeable cells of long cycle life.* Journal of the American Chemical Society, 2018. **140**(20): p. 6343-6352.

23. Chambers, R., F.P. Gerstle Jr, and S. Monroe, *Viscoelastic Effects in a Phosphate Glass-Metal Seal.* Journal of the American Ceramic Society, 1989. **72**(6): p. 929-932.

24. Peng, Y.B. and D.E. Day, *High thermal expansion phosphate glasses. Part 1.* Glass Technology, 1991. **32**(5): p. 8.

25. Wei, T.Y., Y. Hu, and L.G. Hwa, *Structure and elastic properties of low-temperature sealing phosphate glasses.* Journal of Non-Crystalline Solids, 2001. **288**(1): p. 140-147.

26. Gallagher, P., *A study of the thermal decomposition of some alkali metal dihydrogen phosphates and arsenates.* Thermochimica Acta, 1976. **14**(1): p. 131-139.

27. Money, B.K. and K. Hariharan, *Lithium-ion conduction in lithium metaphosphate based systems.* Applied Physics A, 2007. **88**(4): p. 647-652.

28. Geng, S., S. Geng, and Y. Zhai, *Synthesis of LiMn2O4 via high-temperature ball milling process.* Materials and Manufacturing Processes, 2017. **32**(16): p. 1856-1860.

29. Tian, M., et al., *Influence of Temperature on the Performance of LiNi1/3Co1/3Mn1/3O2 Prepared by High-Temperature Ball-Milling Method.* Advances in Materials Science and Engineering, 2018. **2018**: p. 6.

30. El-Eskandarany, M.S., *3 - Controlling the powder milling process*, in *Mechanical Alloying (Second Edition)*, M.S. El-Eskandarany, Editor. 2015, William Andrew Publishing: Oxford. p. 48-83.

31. Jia, L., et al., *Preparation of red-emitting phosphor (Y,Gd)BO3:Eu3+ by high-temperature ball milling.* Ceramics International, 2014. **40**(1, Part A): p. 739-743.

32. Jhan, Y.R. and J.G. Duh, *Synthesis of entanglement structure in nanosized Li4Ti5O12/multi-walled carbon nanotubes composite anode material for Li-ion batteries by ball-milling-assisted solid-state reaction.* Journal of Power Sources, 2012. **198**: p. 294-297.

33. Jia, P., Z. Shao, and K. Liu, *Synthesis and electrochemical performance of Li4Ti5O12 by high-temperature ball milling method.* Materials Letters, 2014. **125**: p. 218-220.

34. Wang, L., et al., *Synthesis and electrochemical performance of Li4Ti5O12/C composite by a starch sol assisted method.* Powder Technology, 2012. **215**: p. 79-84.

35. Dou, S. and W. Wang, *Synthesis and electrochemical properties of layered LiNi0.5 − xMn0.5 − xCo2xO2 for lithium-ion battery from nickel manganese cobalt oxide precursor.* Journal of Solid State Electrochemistry, 2011. **15**(2): p. 399-404.

36. Bang, E.Y., et al., *Lithium nickel cobalt oxides synthesized from Li2CO3, NiO and Co3O4 by the solid-state reaction method.* Ceramics International, 2012. **38**(5): p. 3635-3641.

37. Benjamin, J., *Mechanical alloying.* Scientific American, 1976. **234**(5): p. 40-49.

38. Benjamin, J.S., *Mechanical alloying — A perspective.* Metal Powder Report, 1990. **45**(2): p. 122-127.

39. Suryanarayana, C., *Mechanical alloying and milling.* Progress in materials science, 2001. **46**(1-2): p. 1-184.

40. Froes, F.H., et al., *Synthesis of Advanced Lightweight Metals by Powder Metallurgy Techniques.* Powder Metallurgy, 1996. **39**(1): p. 63-65.

41. McCormick, P., *Application of mechanical alloying to chemical refining (overview).* materials Transactions, JIM, 1995. **36**(2): p. 161-169.

42. Yari, B., P. Sauriol, and J. Chaouki, *Kinetics of the Dehydration of Lithium Dihydrogenphosphate.* The Canadian Journal of Chemical Engineering.

43. Murashova, E. and N. Chudinova, *Synthesis and crystal structures of lithium polyphosphates, LiPO 3, Li 4 H (PO 3) 5, and LiMn (PO 3) 3.* Crystallography Reports, 2001. **46**(6): p. 942-947.

44. Lee, K.-S., et al., *Raman spectroscopic study of.* Solid State Communications, 2008. **145**(9): p. 487-492.

45. Lee, K.-S., et al., *Raman spectroscopic study of LiH2PO4.* Solid State Communications, 2008. **145**(9-10): p. 487-492.

46. Muñoz-Senovilla, L. and F. Muñoz, *Behavior of viscosity in metaphosphate glasses.* Journal of Non-Crystalline Solids, 2014. **385**: p. 9-16.

CHAPTER 7 GENERAL DISCUSSION

Production of safer lithium-ion batteries (LIBs) with less environmental impacts is important for different applications, especially in the automotive industry. Fire or explosion of the battery in cell phones, laptops and even electric vehicles is a familiar story that we may have heard every now and then the media or read in the press. The thermal runaway in LIBs is a serious detrimental issue against their development, which has been addressed in the scientific literature (Kvasha et al., 2018; Xuan Liu et al., 2016). Most of the thermal runaway accidents start from the cathode material and propagate through the organic liquid electrolyte. Lithium iron phosphate (lithium ferrophosphate, $LiFePO_4$, or LFP) is one of the safest cathode materials used in LIBs. It is also more environmentally benign compared to other cathode materials like lithium cobalt oxide ($LiCoO_2$, LCO), lithium nickel manganese cobalt oxide ($Li(Ni_{0,33}Mn_{0,33}Co_{0,33})O_2$, NMC), lithium manganese oxide ($LiMn_2O_4$, LMO), and lithium nickel cobalt aluminium oxide ($Li(Ni_{0,8}Co_{0,15}Al_{0,05})O_2$, NCA), as the iron contamination is less destructive to the environment than nickel, cobalt, manganese and aluminum contamination (Egorova & Ananikov, 2017). Also, iron is more abundant than other metals as the primary material for the cathode production that can potentially reduce the LFP cathode cost as compared to the others.

Production of LFP through melt casting is done by batch or continuous melting of the sources of iron, lithium and phosphate. This method can use primary materials of different grades and particle sizes and produce a high purity LFP product. As compared to other methods of LFP production in industrial scale, this method has the advantage of lower capital and operating costs, as it does not require water or wastewater treatment. However, the problem of sudden gas release during the addition of the solid material to the other molten material is an issue for its scale-up. Therefore, the degassing of the reactants is necessary before adding them to the molten mixture at high temperature (1000 – 1100 °C).

Lithium metaphosphate ($LiPO_3$, LPO) is the product of the degassing (dehydration) of lithium dihydrogenphosphate (LiH_2PO_4, LHP) which is a simultaneous source of lithium and phosphate with a 1:1 ratio like in LFP. The dehydration of LHP can be done in different steps at temperatures between 200 – 400 °C passing a molten phase, which gradually solidifies as the reaction completes. Thus, the final product (LPO) becomes stuck to the surface of the reactor, making it difficult to collect.

Heating the LPO to its melting point (~ 670 °C) and subsequent quenching and grinding it for collection, spend unnecessary energy and cost while breaking and grinding the stuck product in the reaction vessel avoid such waste of energy. Being inspired by the ball milling process and rotary kiln calcination process, the original idea of combining these two processes in one reactor was the motivation of this research. A new type of reactor that we call it Ball-mill rotary-kiln (BaMRoK) was designed built and used for the production of LPO at 400 °C. Operating parameters like the temperature profile, the ball size and the residence time were determined based on the kinetic and hydrodynamic study of this reactor.

In the kinetic study, it was found that the reaction starts on the surface of LHP solid particles upon sintering and then accelerates in the bulk of the material at melting point. The first intermediate was separated at an isotherm of 220 °C to be a solid material at that temperature with a composition equivalent to an oligomer with a degree of 2.5 (L2.5). A second intermediate was separated at 350 °C which was mostly non-crystallized LPO and the remaining of the oligomers which were all condensed to LPO by the elimination of H_2O at 400 °C.

Based on these results, holding the temperature at 220 °C and grinding, avoids the formation of the viscous mixture of different oligomers in the molten monomer and keeps the rolling regime in the BaMRoK. This can result in better product recovery, which was discussed in chapter 6.

The findings in the hydrodynamic study of the BaMRoK revealed the segregation behaviour of the binary system in a range of size ratios. Two significant segregation mechanisms resulting in different segregated states were identified. These mechanisms were separated with a transition size ratio in which the most uniform distribution was found. The methods used for the hydrodynamic study were in good agreement.

The heat transfer in the presence of the grinding media (balls) was studied and by comparing the reaction rate to the kinetic model with the temperature profile of the BaMRoK, it was verified that the LHP particles were segregated on the internal surface of the kiln. The produced LPO in the BaMRoK in this study was characterized by XRD and RAMAN and compared to the product of the small scale LPO production in laboratory-scale, showing good conformity of the product.

The results obtained in the three objectives of this research (1. Kinetics of the dehydration of LHP, 2. Hydrodynamics of the material in the reactor and 3. Heat transfer within the bed of such reactor), can substantially facilitate the scale-up of the process of the dehydration of LHP in the BaMRoK

reactor. The scale-up procedure should be step by step to minimize the risk of large investments (Euzen, Trambouze, & Wauquier, 1993).

The scale of the process in this research can be considered as bench or laboratory scale in which the concept of the technology is proved with a production rate of up to 0.5 kg/h. Next step for scale up would be Pilot scale that may consider continuous production of LPO with a rate of up to 100 kg/h. After that, the demonstration scale can be considered with a production rate of up to 1000 kg/h in which the process flowsheet resembles commercial scale operation.

Scale-up of a process is not linear. The design of the larger scales is controlled by the following rates: kinetics, mass and heat transfer, blending, addition rate. There are some similarities in the scale-up of the BaMRoK reactor. The dynamic similarity or dimensionless number of Fr should be maintained that determines the balls and particles flow regime. The geometry ratios, velocity profiles, heating rate and heating area should be considered for the scale-up (Belwal, Revanth, Dinesh, Reddy, & Bhagvanth, 2016).

CHAPTER 8 CONCLUSION AND RECOMMENDATIONS

The production and recovery of LPO from LHP in a novel BaMRoK reactor at the temperature of the formation of the solid product as the main objective of this research was achieved. Production of LPO is important not only for its application as a degassed reactant for LFP melt casting but also for its new applications as a solid electrolyte for safer and more efficient LIBs. Also, the original idea of the BaMRoK reactor introduced in this research can be used for other similar dehydration processes like the production of Sodium hexametaphosphate (SHMP, Calgon) and other calcination and solid-state reactions to reduce the reaction temperature.

The kinetic, hydrodynamic and heat-transfer study on BaMRoK reactor that was presented in this research along with other future complementary studies can be used for the scale-up of this type of reactor.

The kinetic and mechanism study of the dehydration reaction of LHP shed light on different steps of this reaction, namely solid and liquid surface dehydration steps and the intermediate oligomer with the 2.5 degree of oligomerization. The activation energies calculated by model-free isoconversional method and other fitted kinetic parameters resulted in a kinetic model that can be used for the operation and design purposes. However, future work on the decomposition of the LHP to LPO will need to address the issues related to the starting particle size and sample amounts, which add mass transfer limitations. Also, as the larger-scale production of LPO based on the decomposition of LHP would lend itself to the direct heating of the material with flue gas, the effect of the gas moisture content on the reversibility of the decomposition steps will need to be examined and the models updated. Similar kinetic studies are also recommended for other alkali metal dihydrogenphosphate salts like sodium and potassium.

The solidified-bed matrix sampling method was introduced as a non-expensive granular mixing assessment tool and successfully applied for direct sampling without the common problem of changing the bed configuration (intrusion). Based on the segregation study that was implemented by this tool and verified by DEM modelling, size segregation of binary granular mixtures was studied in tumbling cylinders showing two significant types of segregation depending on the granules' size ratio. However, the solidified-bed matrix sampling method is limited to the less

compact beds and does not work for cohesive and compact particulate mixtures in which the solidifying gel can not penetrate, or the bed that are sensitive to the temperature or may react to or dissolve in aqueous solutions like agar gel solution.

Future studies on BaMRoK reactor which has the benefits of reducing the temperature for solid-state reactions and mechanochemical syntheses, increasing the yield and energy efficiency and combining multiple process stages, are recommended as follows:

Production of LFP in a BaMRoK reactor. This process can be in series with the preliminary degassing (dehydration) reaction in the same reactor.

Application of BaMRoK reactor for waste rubber and plastic pyrolysis that can improve the heat transfer in these processes.

Study the impacts of direct heating through the flame or hot gas currents like cement kilns on operating conditions. In such cases, controlling the dust formation and the carryover of the particles is a future study recommendation.

Another study that is recommended for future is to study the effect of operating conditions like initial particle size distribution, the filling ratio, rotation rate and carrier gas flow on the heat transfer and the final product particle size.

Application of binary-sized grinding media based on the size segregation study in this research is also recommended, especially in grinding stage, to improve the milling efficiency by inducing the uniform distribution of the material in the bed.

REFERENCES

Abdel-Kader, A., Ammar, A., & Saleh, S. (1990). High-temperature phase transition in potassium dihydrogen phosphate crystals. *Thermochimica Acta, 167*(2), 225-233.

Adams, T. N. Lime kilns principles and operations. *Technical consultant, Seattle WA.*

Ajaal, T., Smith, R., & Yen, W. (2002). The development and characterization of a ball mill for mechanical alloying. *Canadian metallurgical quarterly, 41*(1), 7-14.

Alexander, A., Muzzio, F., & Shinbrot, T. (2004). Effects of scale and inertia on granular banding segregation. *Granular Matter, 5*(4), 171-175.

Alizadeh, E. (2013). *Numerical and Experimental Investigation of Solid Mixing and Segregation in Tumbling Blenders.* École Polytechnique de Montréal.

Alizadeh, E., Bertrand, F., & Chaouki, J. (2014a). Comparison of DEM results and Lagrangian experimental data for the flow and mixing of granules in a rotating drum. *AIChE Journal, 60*(1), 60-75.

Alizadeh, E., Bertrand, F., & Chaouki, J. (2014b). Discrete element simulation of particle mixing and segregation in a tetrapodal blender. *Computers & Chemical Engineering, 64*, 1-12.

Alizadeh, E., Dubé, O., Bertrand, F., & Chaouki, J. (2013). Characterization of mixing and size segregation in a rotating drum by a particle tracking method. *AIChE Journal, 59*(6), 1894-1905.

Alizadeh, E., Hajhashemi, H., Bertrand, F., & Chaouki, J. (2013). Experimental investigation of solid mixing and segregation in a tetrapodal blender. *Chemical Engineering Science, 97*, 354-365.

Allen, M. P., & Tildesley, D. J. (1989). *Computer simulation of liquids*: Oxford university press.

Allen, T. (2013). *Particle size measurement*: Springer.

Alphonse L. (1968). US 3414375.

Angaiah E. A. (2003). US 6656441 B2.

Angaiah, S., Thiagarajan, V., Ramaiyer, G., & Meenakshisundaram, R. (2003). Process for the preparation of lithium metaphosphate: Google Patents.

Aoki, K. M., & Akiyama, T. (1995). Simulation studies of pressure and density wave propagations in vertically vibrated beds of granules. *Physical Review E, 52*(3), 3288.

Aranson, I., Tsimring, L., & Vinokur, V. (1999). Continuum theory of axial segregation in a long rotating drum. *Physical Review E, 60*(2), 1975.

Aranson, I., & Tsimring, L. S. (1999). Dynamics of axial separation in long rotating drums. *PHYSICAL REVIEW LETTERS, 82*(23), 4643.

Arndt, T., Siegmann-Hegerfeld, T., Fiedor, S. J., Ottino, J. M., & Lueptow, R. M. (2005). Dynamics of granular band formation: Long-term behavior in slurries, parameter space, and tilted cylinders. *Physical Review E, 71*(1), 011306.

Arnold, G., Garche, J., Hemmer, R., Ströbele, S., Vogler, C., & Wohlfahrt-Mehrens, M. (2003). Fine-particle lithium iron phosphate LiFePO 4 synthesized by a new low-cost aqueous precipitation technique. *Journal of Power Sources, 119*, 247-251.

Arntz, M., Beeftink, H., Otter, W., Briels, W. J., & Boom, R. (2014). Segregation of granular particles by mass, radius, and density in a horizontal rotating drum. *AIChE Journal, 60*(1), 50-59.

Arntz, M., den Otter, W. K., Beeftink, H., Boom, R., & Briels, W. J. (2013). The influence of end walls on the segregation pattern in a horizontal rotating drum. *Granular Matter, 15*(1), 25-38.

Arratia, P., Duong, N.-h., Muzzio, F., Godbole, P., Lange, A., & Reynolds, S. (2006). Characterizing mixing and lubrication in the Bohle Bin blender. *Powder Technology, 161*(3), 202-208.

Arratia, P., Duong, N.-h., Muzzio, F., Godbole, P., & Reynolds, S. (2006). A study of the mixing and segregation mechanisms in the Bohle Tote blender via DEM simulations. *Powder Technology, 164*(1), 50-57.

Bagryantseva, I., & Ponomareva, V. (2016). Proton conductivity and phase composition of mixed salts in the systems MH2PO4–CsHSO4 (M= Cs, K). *Physics of the Solid State, 58*(8), 1651-1658.

Bang, E. Y., Mumm, D. R., Park, H. R., & Song, M. Y. (2012). Lithium nickel cobalt oxides synthesized from Li2CO3, NiO and Co3O4 by the solid-state reaction method. *Ceramics International, 38*(5), 3635-3641. doi:https://doi.org/10.1016/j.ceramint.2012.01.002

Barker, G. C., & Mehta, A. (1993). Size segregation in powders. *Nature, 361*, 308. doi:10.1038/361308a0

Barker, G. C., & Mehta, A. (1993). Size segregation mechanisms. *Nature, 364*, 486. doi:10.1038/364486a0

Bellamy, L. J., Nordon, A., & Littlejohn, D. (2008). Real-time monitoring of powder mixing in a convective blender using non-invasive reflectance NIR spectrometry. *Analyst, 133*(1), 58-64.

Belwal, S., Revanth, V., Dinesh, K., Reddy, B., & Bhagvanth, M. (2016). Development and scale up of a chemical process in pharmaceutical industry: a case study. *Int. J. Eng. Res. Appl, 6*(7), 81-88.

Benjamin, J. (1976). Mechanical alloying. *Scientific American, 234*(5), 40-49.

Benjamin, J. S. (1990). Mechanical alloying — A perspective. *Metal Powder Report, 45*(2), 122-127. doi:https://doi.org/10.1016/S0026-0657(10)80124-9

Benkhoucha, R., & Wunderlich, B. (1978). Crystallization during polymerization of Lithium Dihydrogen Phosphate. I. Nucleation of the Macromolecular Crystal from the Oligomer Melt. *Zeitschrift für anorganische und allgemeine Chemie, 444*(1), 256-266.

Berntsson, O., Danielsson, L.-G., Lagerholm, B., & Folestad, S. (2002). Quantitative in-line monitoring of powder blending by near infrared reflection spectroscopy. *Powder Technology, 123*(2-3), 185-193.

Bertrand, F., Leclaire, L.-A., & Levecque, G. (2005). DEM-based models for the mixing of granular materials. *Chemical Engineering Science, 60*(8), 2517-2531.

Bird, R. B., Stewart, W. E., & Lightfoot, E. N. (1960). Transport phenomena. 1960. *Madison, USA*.

Bitar, M., & Knowles, J. (2005). Soluble phosphate glass fibres for repair of bone-ligament interface. *Journal of Materials Science: Materials in Medicine 16 (12)*, 1131-1136.

Blais, B., Vidal, D., Bertrand, F., Patience, G. S., & Chaouki, J. (2019). Experimental Methods in Chemical Engineering: Discrete Element Method---DEM. *The Canadian Journal of Chemical Engineering*.

Blezard R. G. (1998). *Reflections of the History of the Chemistry of Cement*. UK: Society of Chemical Industry (SCI).

Blinc, R., O'Reilly, D., Peterson, E., & Williams, J. M. (1969). High-Temperature Phase Transition in RbH2PO4. *The Journal of Chemical Physics, 50*(12), 5408-5411.

Boateng, A. (1998). Boundary layer modeling of granular flow in the transverse plane of a partially filled rotating cylinder. *International Journal of Multiphase Flow, 24*(3), 499-521.

Boateng, A., & Barr, P. (1996). Modelling of particle mixing and segregation in the transverse plane of a rotary kiln. *Chemical Engineering Science, 51*(17), 4167-4181.

Boateng, A. A. (2011). *Rotary kilns: transport phenomena and transport processes*: Butterworth-Heinemann.

Boateng, A. A. (2015). *Rotary kilns: transport phenomena and transport processes*: Butterworth-Heinemann.

Braga, M. H., Grundish, N., Murchison, A., & Goodenough, J. (2017). Alternative strategy for a safe rechargeable battery. *Energy & Environmental Science, 10*(1), 331-336.

Braga, M. H., M Subramaniyam, C., Murchison, A. J., & Goodenough, J. B. (2018). Nontraditional, safe, high voltage rechargeable cells of long cycle life. *Journal of the American Chemical Society, 140*(20), 6343-6352.

Bridgwater, J. (1976). Fundamental powder mixing mechanisms. *Powder Technology, 15*(2), 215-236.

Bridgwater, J., Foo, W., & Stephens, D. (1985). Particle mixing and segregation in failure zones—theory and experiment. *Powder Technology, 41*(2), 147-158.

Brilliantov, N. V., Spahn, F., Hertzsch, J.-M., & Pöschel, T. (1996). Model for collisions in granular gases. *Physical Review E, 53*(5), 5382.

Brone, D., Alexander, A., & Muzzio, F. (1998). Quantitative characterization of mixing of dry powders in V-blenders. *AIChE Journal, 44*(2), 271-278.

Brone, D., Wightman, C., Connor, K., Alexander, A., Muzzio, F., & Robinson, P. (1997). Using flow perturbations to enhance mixing of dry powders in V-blenders. *Powder Technology, 91*(3), 165-172.

Brown, M., Dollimore, D., & Galwey, A. (1980). Reactions in the Solid State, vol. 22 of Comprehensive Chemical Kinetics, Bamford, CH and Tipper, CFH, Eds: Amsterdam: Elsevier.

Brown, M., Maciejewski, M., Vyazovkin, S., Nomen, R., Sempere, J., Burnham, A. a., . . . Kemmler, A. (2000). Computational aspects of kinetic analysis: part A: the ICTAC kinetics project-data, methods and results. *Thermochimica Acta, 355*(1), 125-143.

Brown, M. E. (2005). Stocktaking in the kinetics cupboard. *Journal of thermal analysis and calorimetry, 82*(3), 665-669.

Burnham, A. K. (2000). Computational aspects of kinetic analysis.: Part D: The ICTAC kinetics project—multi-thermal–history model-fitting methods and their relation to isoconversional methods. *Thermochimica Acta, 355*(1), 165-170.

C., B. F. (961). Crushing and Grinding Calculations. Part II. *British Chemical Engineering, 6*(8), 543-548.

C., B. F. (1961). Crushing and Grinding Calculations. Part I. *British Chemical Engineering, 6*(6), 378-385.

Cantelaube, F., & Bideau, D. (1995). Radial segregation in a 2d drum: an experimental analysis. *EPL (Europhysics Letters), 30*(3), 133.

Cantelaube, F., Bideau, D., & Roux, S. (1997). Kinetics of segregation of granular media in a two-dimensional rotating drum. *Powder Technology, 93*(1), 1-11.

Cassanello, M., Larachi, F., Marie, M.-N., Guy, C., & Chaouki, J. (1995). Experimental characterization of the solid phase chaotic dynamics in three-phase fluidization. *Industrial & engineering chemistry research, 34*(9), 2971-2980.

Chambers, R., Gerstle Jr, F. P., & Monroe, S. (1989). Viscoelastic Effects in a Phosphate Glass-Metal Seal. *Journal of the American Ceramic Society, 72*(6), 929-932.

Chaouki, J., Larachi, F., & Duduković, M. P. (1997). Noninvasive tomographic and velocimetric monitoring of multiphase flows. *Industrial & engineering chemistry research, 36*(11), 4476-4503.

Chen, J., & Whittingham, M. S. (2006). Hydrothermal synthesis of lithium iron phosphate. *Electrochemistry Communications, 8*(5), 855-858.

Chen, M., Yan, Y., & Liu, W.-m. (2015). Room-temperature fabrication of flexible thin-film lithium batteries based on solid electrolytes and polyimide substrates. *Applied Mechanics and Materials , 723*, 664-669.

Chen, P., Ottino, J. M., & Lueptow, R. M. (2010). Onset mechanism for granular axial band formation in rotating tumblers. *PHYSICAL REVIEW LETTERS, 104*(18), 188002.

Chester, A. W., Kowalski, J. A., Coles, M. E., Muegge, E. L., Muzzio, F. J., & Brone, D. (1999). Mixing dynamics in catalyst impregnation in double-cone blenders. *Powder Technology, 102*(1), 85-94.

Cho, J., Zhu, Y., Lewkowicz, K., Lee, S., Bergman, T., & Chaudhuri, B. (2012). Solving granular segregation problems using a biaxial rotary mixer. *Chemical Engineering and Processing: Process Intensification, 57*, 42-50.

Choi, J., Hayashi, T., Endoh, S., & Sakamoto, H. (1999). *Separation of metallic particles by vertical vibration for solid waste treatment.* Paper presented at the Environmentally

Conscious Design and Inverse Manufacturing, 1999. Proceedings. EcoDesign'99: First International Symposium On.

Choo, K., Baker, M. W., Molteno, T., & Morris, S. W. (1998). Dynamics of granular segregation patterns in a long drum mixer. *Physical Review E, 58*(5), 6115.

Chung Y. S. (1962). Trimetaphosphate processes. *US 3314750 A*.

Cleary, P. W. (1998). Predicting charge motion, power draw, segregation and wear in ball mills using discrete element methods. *Minerals engineering, 11*(11), 1061-1080.

Cleary, P. W. (2009). Ball motion, axial segregation and power consumption in a full scale two chamber cement mill. *Minerals engineering, 22*(9), 809-820.

Cundall, P. A., & Strack, O. D. (1979). A discrete numerical model for granular assemblies. *Geotechnique, 29*(1), 47-65.

Daumann, B., Fath, A., Anlauf, H., & Nirschl, H. (2009). Determination of the mixing time in a discontinuous powder mixer by using image analysis. *Chemical Engineering Science, 64*(10), 2320-2331.

de Haro, M. L., & Cohen, E. (1984). The Enskog theory for multicomponent mixtures. III. Transport properties of dense binary mixtures with one tracer component. *The Journal of Chemical Physics, 80*(1), 408-415.

de Haro, M. L., Cohen, E., & Kincaid, J. (1983). The Enskog theory for multicomponent mixtures. I. Linear transport theory. *The Journal of Chemical Physics, 78*(5), 2746-2759.

Deniz, V. (2003). A study on the specific rate of breakage of cement materials in a laboratory ball mill. *Cement and concrete research, 33*(3), 439-445.

Di Renzo, A., & Di Maio, F. P. (2005). An improved integral non-linear model for the contact of particles in distinct element simulations. *Chemical Engineering Science, 60*(5), 1303-1312.

Donald, M. B., Roseman, B., imprimée, -. R., & (microfilms)., M.-F. v.-v. n.-A. (1962). Mixing and demixing of solid particles. I. Mechanisms in a horizontal drum mixer. *Br. Chem. Eng., 7*, 749-753.

Dou, S., & Wang, W. (2011). Synthesis and electrochemical properties of layered LiNi0.5 − xMn0.5 − xCo2xO2 for lithium-ion battery from nickel manganese cobalt oxide precursor. *Journal of Solid State Electrochemistry, 15*(2), 399-404. doi:10.1007/s10008-010-1101-1

Doucet, J., Bertrand, F., & Chaouki, J. (2007). *Flow Structure Mapping Of Segregating Granular Mixtures Using Radioactive Particle Tracking.* Paper presented at the The 2007 Annual Meeting.

Doucet, J., Bertrand, F., & Chaouki, J. (2008). An extended radioactive particle tracking method for systems with irregular moving boundaries. *Powder Technology, 181*(2), 195-204.

Doucet, J., Bertrand, F., & Chaouki, J. (2008). A measure of mixing from Lagrangian tracking and its application to granular and fluid flow systems. *Chemical Engineering Research and Design, 86*(12), 1313-1321.

Doucet, J., Hudon, N., Bertrand, F., & Chaouki, J. (2008). Modeling of the mixing of monodisperse particles using a stationary DEM-based Markov process. *Computers & Chemical Engineering, 32*(6), 1334-1341.

Dubé, O., Ackley, M., Celik, C., Chaouki, J., & Bertrand, F. (2014). Discrete element simulation of the dynamics of adsorbents in a radial flow reactor used for gas prepurification. *Adsorption, 20*(1), 91-107. doi:10.1007/s10450-013-9552-1

Dubé, O., Alizadeh, E., Chaouki, J., & Bertrand, F. (2013). Dynamics of non-spherical particles in a rotating drum. *Chemical Engineering Science, 101*, 486-502.

Duong, N.-H., Arratia, P., Muzzio, F., Lange, A., Timmermans, J., & Reynolds, S. (2003). A homogeneity study using NIR spectroscopy: tracking magnesium stearate in Bohle bin-blender. *Drug Development and Industrial Pharmacy, 29*(6), 679-687.

Ebert, D. S., Musgrave, F. K., Peachey, D., Perlin, K., & Worley, S. (2003). *Texturing & modeling: a procedural approach*: Morgan Kaufmann.

Egorova, K. S., & Ananikov, V. P. (2017). Toxicity of metal compounds: knowledge and myths. *Organometallics, 36*(21), 4071-4090.

El-Eskandarany, M. S. (2015). 3 - Controlling the powder milling process. In M. S. El-Eskandarany (Ed.), *Mechanical Alloying (Second Edition)* (pp. 48-83). Oxford: William Andrew Publishing.

El-Hagrasy, A. S., D'Amico, F., & Drennen, J. K. (2006). A Process Analytical Technology approach to near-infrared process control of pharmaceutical powder blending. Part I: D-optimal design for characterization of powder mixing and preliminary spectral data evaluation. *Journal of pharmaceutical sciences, 95*(2), 392-406.

El Hagrasy, A. S., Chang, S.-Y., & Kiang, S. (2006). Evaluation of risk and benefit in the implementation of near-infrared spectroscopy for monitoring of lubricant mixing. *Pharmaceutical development and technology, 11*(3), 303-312.

Erdem, A., & Ergun, S. (2009). The effect of ball size on breakage rate parameter in a pilot scale. *Ball Mill Minerals Engineering, 22*, 7-8.

Euzen, J.-P., Trambouze, P., & Wauquier, J.-P. (1993). *Scale-up methodology for chemical processes*: Editions Technip.

Fiedor, S. J., Umbanhowar, P., & Ottino, J. M. (2007). Effects of fluid viscosity on band segregation dynamics in bidisperse granular slurries. *Physical Review E, 76*(4), 041303.

Finger, T., Schröter, M., & Stannarius, R. (2015). The mechanism of long-term coarsening of granular mixtures in rotating drums. *New Journal of Physics, 17*(9), 093023.

Froes, F. H., Suryanarayana, C., Taylor, P. R., Ward-Close, C. M., & Goodwin, P. (1996). Synthesis of Advanced Lightweight Metals by Powder Metallurgy Techniques. *Powder Metallurgy, 39*(1), 63-65. doi:10.1179/pom.1996.39.1.63

Fuerstenau, D., Lutch, J., & De, A. (1999). The effect of ball size on the energy efficiency of hybrid high-pressure roll mill/ball mill grinding. *Powder Technology, 105*(1), 199-204.

Gallagher, P. (1976). A study of the thermal decomposition of some alkali metal dihydrogen phosphates and arsenates. *Thermochimica Acta, 14*(1), 131-139.

Gao, M.-W., & Forssberg, E. (1993). A study on the effect of parameters in stirred ball milling. *International Journal of Mineral Processing, 37*(1), 45-59.

Gao, M., & Forssberg, E. (1992). Increasing the specific surface area of dolomite by stirred ball milling. *Kawatra, SK, Comminution–Theory and Practice, S. Komar Kawatra, 2*, 153-170.

Gauthier, L., Gauthier, M., Lavoie, D., Michot, C., & Ravet, N. (2009a). Lithiated transition metal oxyanion-based lithium-ion reversible electrode material formed by heating precursor, melting, and cooling: Google Patents.

Gauthier, L., Gauthier, M., Lavoie, D., Michot, C., & Ravet, N. (2009b). Process for preparing electroactive insertion compounds and electrode materials obtained therefrom: Google Patents.

Gauthier, L., Gauthier, M., Lavoie, D., Michot, C., & Ravet, N. (2011). Process for preparing electroactive insertion compounds and electrode materials obtained therefrom: Google Patents.

Gauthier, M., Michot, C., Ravet, N., Duchesneau, M., Dufour, J., Liang, G., . . . MacNeil, D. (2010). Melt casting LiFePO4 I. Synthesis and characterization. *Journal of the Electrochemical Society, 157*(4), A453-A462.

Geng, S., Geng, S., & Zhai, Y. (2017). Synthesis of LiMn2O4 via high-temperature ball milling process. *Materials and Manufacturing Processes, 32*(16), 1856-1860. doi:10.1080/10426914.2017.1317797

Gosselin, R., Duchesne, C., & Rodrigue, D. (2008). On the characterization of polymer powders mixing dynamics by texture analysis. *Powder Technology, 183*(2), 177-188.

Gupta, A., & Yan, D. S. (2006). *Mineral processing design and operation: an introduction*: Elsevier.

Gupta, S. D., Khakhar, D., & Bhatia, S. (1991a). Axial segregation of particles in a horizontal rotating cylinder. *Chemical Engineering Science, 46*(5-6), 1513-1517.

Gupta, S. D., Khakhar, D., & Bhatia, S. (1991b). Axial transport of granular solids in horizontal rotating cylinders. Part 1: Theory. *Powder Technology, 67*(2), 145-151.

Habib, M., Miles, N. J., Habib, U., & Hall, P. (2013). Separation of dry particulate mixtures by controlled vertical vibration. *Particulate Science and Technology, 31*(6), 555-560.

Hailey, P., Doherty, P., Tapsell, P., Oliver, T., & Aldridge, P. (1996). Automated system for the on-line monitoring of powder blending processes using near-infrared spectroscopy part I. System development and control. *Journal of Pharmaceutical and Biomedical Analysis, 14*(5), 551-559.

Hawkesworth, M., Parker, D., Fowles, P., Crilly, J., Jefferies, N., & Jonkers, G. (1991). Nonmedical applications of a positron camera. *Nuclear Instruments and Methods in Physics Research Section A: Accelerators, Spectrometers, Detectors and Associated Equipment, 310*(1), 423-434.

HEKO. (2016). http://www.heko.com/index.php?id=234.

Henein, H. (1980). *Bed behaviour in rotary cylinders with applications to rotary kilns.* University of British Columbia.

Hill, K., Caprihan, A., & Kakalios, J. (1997). Axial segregation of granular media rotated in a drum mixer: Pattern evolution. *Physical Review E, 56*(4), 4386.

Hill, K., & Kakalios, J. (1995). Reversible axial segregation of rotating granular media. *Physical Review E, 52*(4), 4393.

Hill, K. M., Caprihan, A., & Kakalios, J. (1997). Bulk segregation in rotated granular material measured by magnetic resonance imaging. *PHYSICAL REVIEW LETTERS, 78*(1), 50.

Hirschfelder, J. O., Curtiss, C. F., Bird, R. B., & Mayer, M. G. (1954). *Molecular theory of gases and liquids* (Vol. 26): Wiley New York.

Hockicko, P., Kúdelčík, J., Muñoz, F., & Muñoz-Senovilla, L. (2014). *Electrical properties of LiPO 3 glasses.* Paper presented at the 2014 ELEKTRO.

Huang, A.-N., & Kuo, H.-P. (2014). Developments in the tools for the investigation of mixing in particulate systems–a review. *Advanced Powder Technology, 25*(1), 163-173.

Huang, A.-N., Liu, L.-C., & Kuo, H.-P. (2013). The role of end wall shearing in the drum segregation band formation. *Powder Technology, 239*, 98-104.

Huang, A., & Kuo, H. (2012). A study of the three-dimensional particle size segregation structure in a rotating drum. *AIChE Journal, 58*(4), 1076-1083.

Jenkins, J., & Mancini, F. (1989). Kinetic theory for binary mixtures of smooth, nearly elastic spheres. *Physics of Fluids A: Fluid Dynamics (1989-1993), 1*(12), 2050-2057.

Jhan, Y. R., & Duh, J. G. (2012). Synthesis of entanglement structure in nanosized Li4Ti5O12/multi-walled carbon nanotubes composite anode material for Li-ion batteries by ball-milling-assisted solid-state reaction. *Journal of Power Sources, 198*, 294-297. doi:https://doi.org/10.1016/j.jpowsour.2011.09.063

Ji, S., & Shen, H. H. (2006). Effect of contact force models on granular flow dynamics. *Journal of engineering mechanics, 132*(11), 1252-1259.

Jia, L., Shao, Z., Lü, Q., Tian, Y., & Han, J. (2014). Preparation of red-emitting phosphor (Y,Gd)BO3:Eu3+ by high temperature ball milling. *Ceramics International, 40*(1, Part A), 739-743. doi:https://doi.org/10.1016/j.ceramint.2013.06.063

Jia, P., Shao, Z., & Liu, K. (2014). Synthesis and electrochemical performance of Li4Ti5O12 by high temperature ball milling method. *Materials Letters, 125*, 218-220. doi:https://doi.org/10.1016/j.matlet.2014.03.153

Jones, J., Parker, D., & Bridgwater, J. (2007). Axial mixing in a ploughshare mixer. *Powder Technology, 178*(2), 73-86.

Juarez, G., Lueptow, R. M., & Ottino, J. M. (2010). Granular coarsening: Phase space and evolution analogies. *Physical Review E, 81*(1), 012301.

Jugović, D., & Uskoković, D. (2009). A review of recent developments in the synthesis procedures of lithium iron phosphate powders. *Journal of Power Sources, 190*(2), 538-544.

Karabulut, M. (2001). Mechanical and structural properties of phosphate glasses. *Journal of Non-Crystalline Solids 288*, 8-17.

Kartini, E., YS Panca Putra, T., Kuntoro, I., Sakuma, T., Basar, K., Kamishima, O., & Kawamura, J. (2010). Recent studies on lithium solid electrolytes (LiI) x (LiPO3) 1-x for secondary battery. *Journal of the Physical Society of Japan, 79*(Suppl. A), 54-58.

Khakhar, D., McCarthy, J., Shinbrot, T., & Ottino, J. (1997). Transverse flow and mixing of granular materials in a rotating cylinder. *Physics of Fluids (1994-present), 9*(1), 31-43.

Khawam, A., & Flanagan, D. R. (2006). Solid-state kinetic models: basics and mathematical fundamentals. *The journal of physical chemistry B, 110*(35), 17315-17328.

Kincaid, J., Cohen, E., & de Haro, M. L. (1987). The Enskog theory for multicomponent mixtures. IV. Thermal diffusion. *The Journal of Chemical Physics, 86*(2), 963-975.

Kincaid, J., de Haro, M. L., & Cohen, E. (1983). The Enskog theory for multicomponent mixtures. II. Mutual diffusion. *The Journal of Chemical Physics, 79*(9), 4509-4521.

Kissinger, H. E. (1957). Reaction kinetics in differential thermal analysis. *Analytical chemistry, 29*(11), 1702-1706.

Klaewkla, R., Arend, M., & Hoelderich, W. F. (2011). A review of mass transfer controlling the reaction rate in heterogeneous catalytic systems *Mass Transfer-Advanced Aspects*: InTech.

Koga, N. (2013). Ozawa's kinetic method for analyzing thermoanalytical curves. *Journal of thermal analysis and calorimetry, 113*(3), 1527-1541.

Kotake, N., Daibo, K., Yamamoto, T., & Kanda, Y. (2004). Experimental investigation on a grinding rate constant of solid materials by a ball mill—effect of ball diameter and feed size. *Powder Technology, 143*, 196-203.

Kotake, N., Kuboki, M., Kiya, S., & Kanda, Y. (2011). Influence of dry and wet grinding conditions on fineness and shape of particle size distribution of product in a ball mill. *Advanced Powder Technology, 22*(1), 86-92.

Kowalska, E., & Kowalski, W. (1962). Influence of temperature on the rate of formation of NaH pyrophosphate from monosodinm orthophosphate. *Przem. Chem., 41*(No. 2), 73-74.

Kowalska, E., Kowalski, W., & Truszkowski, A. (1963). Influence of temperature on the formation rate of Na metaphosphate from Na dihydrogen pyrophosphate. *Przem. Chem., 42*(4-5), 212-214.

Kowalski, Z., Boron, K., Gajos, W., Trefler, U., Bunikowska, B., & Wantuch, M. (1987). PL142169B1.

Kuo, H., Knight, P., Parker, D., & Seville, J. (2005). Solids circulation and axial dispersion of cohesionless particles in a V-mixer. *Powder Technology, 152*(1-3), 133-140.

Kuo, H., Shih, P., & Hsu, R. (2006). Coupled axial–radial segregation in rotating drums with high fill levels. *AIChE Journal, 52*(7), 2422-2427.

Kuwabara, G., & Kono, K. (1987). Restitution coefficient in a collision between two spheres. *Japanese journal of applied physics, 26*(8R), 1230.

Kvasha, A., Gutiérrez, C., Osa, U., de Meatza, I., Blazquez, J. A., Macicior, H., & Urdampilleta, I. (2018). A comparative study of thermal runaway of commercial lithium ion cells. *Energy, 159*, 547-557.

Lacey, P. M. C. (1954). Developments in the theory of particle mixing. *Journal of applied chemistry, 4*(5), 257-268.

Langston, P., Tüzün, U., & Heyes, D. (1994). Continuous potential discrete particle simulations of stress and velocity fields in hoppers: transition from fluid to granular flow. *Chemical Engineering Science, 49*(8), 1259-1275.

Larachi, F., Chaouki, J., & Kennedy, G. (1995). 3-d mapping of solids flow fields in multiphase reactors with rpt. *AIChE Journal, 41*(2), 439-443.

Larachi, F., Kennedy, G., & Chaouki, J. (1994). A γ-ray detection system for 3-D particle tracking in multiphase reactors. *Nuclear Instruments and Methods in Physics Research Section A: Accelerators, Spectrometers, Detectors and Associated Equipment, 338*(2), 568-576.

Lee, J., & Herrmann, H. J. (1993). Angle of repose and angle of marginal stability: molecular dynamics of granular particles. *Journal of Physics A: Mathematical and General, 26*(2), 373.

Lee, K.-S. (1996). Hidden nature of the high-temperature phase transitions in crystals of KH 2 PO 4-type: is it a physical change? *Journal of Physics and Chemistry of Solids, 57*(3), 333-342.

Lee, K.-S., Ko, J.-H., Moon, J., Lee, S., & Jeon, M. (2008a). Raman spectroscopic study of. *Solid State Communications, 145*(9), 487-492.

Lee, K.-S., Ko, J.-H., Moon, J., Lee, S., & Jeon, M. (2008b). Raman spectroscopic study of LiH2PO4. *Solid State Communications, 145*(9-10), 487-492.

Lee, K.-S., Moon, J., Lee, J., & Jeon, M. (2008). High-temperature phase transformations in LiH 2 PO 4 and possible solid-state polymerization. *Solid State Communications, 147*(1), 74-77.

Lee, K.-S., Oh, I.-H., Kweon, J. J., Lee, C. E., & Ahn, S.-H. (2012). Crystal growth and morphology of LiH 2 PO 4. *Materials Chemistry and Physics, 136*(2), 802-808.

Lemieux, M., Bertrand, F., Chaouki, J., & Gosselin, P. (2007). Comparative study of the mixing of free-flowing particles in a V-blender and a bin-blender. *Chemical Engineering Science, 62*(6), 1783-1802.

Lemieux, M., Léonard, G., Doucet, J., Leclaire, L.-A., Viens, F., Chaouki, J., & Bertrand, F. (2008). Large-scale numerical investigation of solids mixing in a V-blender using the discrete element method. *Powder Technology, 181*(2), 205-216.

Levitan, B. (1998). Segregation and coarsening of granular mixture in a rotating tube. *Physica A: Statistical Mechanics and its Applications, 249*(1-4), 386-390.

Li, Y., Xu, Y., & Thornton, C. (2005). A comparison of discrete element simulations and experiments for 'sandpiles' composed of spherical particles. *Powder Technology, 160*(3), 219-228.

Lide, D. R. (1995). *CRC handbook of chemistry and physics: a ready-reference book of chemical and physical data*: CRC press.

Liu, X., Wu, Z., Stoliarov, S. I., Denlinger, M., Masias, A., & Snyder, K. (2016). Heat release during thermally-induced failure of a lithium ion battery: impact of cathode composition. *Fire Safety Journal, 85*, 10-22.

Liu, X., Zhang, C., & Zhan, J. (2015). Quantitative comparison of image analysis methods for particle mixing in rotary drums. *Powder Technology, 282*, 32-36.

Longo, S., & Lamberti, A. (2002). Grain shear flow in a rotating drum. *Experiments in fluids, 32*(3), 313-325.

Maciejewski, M. (2000). Computational aspects of kinetic analysis.: Part B: The ICTAC Kinetics Project—the decomposition kinetics of calcium carbonate revisited, or some tips on survival in the kinetic minefield. *Thermochimica Acta, 355*(1), 145-154.

MacNeil, D., Devigne, L., Michot, C., Rodrigues, I., Liang, G., & Gauthier, M. (2010). Melt Casting LiFePO4 II. Particle Size Reduction and Electrochemical Evaluation. *Journal of the Electrochemical Society, 157*(4), A463-A468.

Mankosa, M., Adel, G., & Yoon, R. (1989). Effect of operating parameters in stirred ball mill grinding of coal. *Powder Technology, 59*(4), 255-260.

Marigo, M., Davies, M., Leadbeater, T., Cairns, D., Ingram, A., & Stitt, E. (2013). Application of Positron Emission Particle Tracking (PEPT) to validate a Discrete Element Method (DEM) model of granular flow and mixing in the Turbula mixer. *International Journal of Pharmaceutics, 446*(1-2), 46-58.

Martin, T., Seville, J., & Parker, D. (2007). A general method for quantifying dispersion in multiscale systems using trajectory analysis. *Chemical Engineering Science, 62*(13), 3419-3428.

Martinez, H., Botez, C., Tackett, R., & Chianelli, R. (2009). *High Temperature Phase Transitions in RbH2PO4.* Paper presented at the APS Texas Sections Spring Meeting Abstracts.

McCormick, P. (1995). Application of mechanical alloying to chemical refining (overview). *materials Transactions, JIM, 36*(2), 161-169.

Mehrotra, A., & Muzzio, F. J. (2009). Comparing mixing performance of uniaxial and biaxial bin blenders. *Powder Technology, 196*(1), 1-7.

Meier, S. W., Lueptow, R. M., & Ottino, J. M. (2007). A dynamical systems approach to mixing and segregation of granular materials in tumblers. *Advances in Physics, 56*(5), 757-827.

Melin, H. E., & Ledung, G. (2019). State-of-the-art in reuse and recycling of lithium-ion batteries–A research review. Retrieved from http://www.energimyndigheten.se/globalassets/forskning--innovation/overgripande/state-of-the-art-in-reuse-and-recycling-of-lithium-ion-batteries-2019.pdf

Mendez, A. S., de Carli, G., & Garcia, C. V. (2010). Evaluation of powder mixing operation during batch production: application to operational qualification procedure in the pharmaceutical industry. *Powder Technology, 198*(2), 310-313.

Metcalfe, G., Graham, L., Zhou, J., & Liffman, K. (1999). Measurement of particle motions within tumbling granular flows. *Chaos: An Interdisciplinary Journal of Nonlinear Science, 9*(3), 581-593.

Metcalfe, G., & Shattuck, M. (1996). Pattern formation during mixing and segregation of flowing granular materials. *Physica A: Statistical Mechanics and its Applications, 233*(3-4), 709-717.

Mindlin, R. (2013). Compliance of elastic bodies in contact. *Journal of Applied Mechanics, 16*.

Mindlin, R., & Deresiewicz, H. (1954). Thickness-Shear and Flexural Vibrations of a Circular Disk. *Journal of Applied Physics, 25*(10), 1329-1332.

Mizushima, K., Jones, P., Wiseman, P., & Goodenough, J. (1980). LixCoO2 (0< x<-1): A new cathode material for batteries of high energy density. *Materials Research Bulletin, 15*(6), 783-789.

Mizushima, K., Jones, P. C., Wiseman, P. J., & Goodenough, J. B. (1980). LixCoO2 (0<x<-1): A new cathode material for batteries of high energy density. *Materials Research Bulletin, 15*(6), 783-789. doi:https://doi.org/10.1016/0025-5408(80)90012-4

Moakher, M., Shinbrot, T., & Muzzio, F. J. (2000). Experimentally validated computations of flow, mixing and segregation of non-cohesive grains in 3D tumbling blenders. *Powder Technology, 109*(1), 58-71.

Money, B. K., & Hariharan, K. (2007). Lithium ion conduction in lithium metaphosphate based systems. *Applied Physics A, 88*(4), 647-652. doi:10.1007/s00339-007-4020-y

Monov, V., Sokolov, B., & Stoenchev, S. (2012). Grinding in ball mills: modeling and process control. *Cybernetics and information technologies, 12*(2), 51-68.

Muñoz-Senovilla, L., & Muñoz, F. (2014). Behaviour of viscosity in metaphosphate glasses. *Journal of Non-Crystalline Solids, 385*, 9-16.

Muñoz, F., Durán, A., Pascual, L., Montagne, L., Revel, B., & Rodrigues, A. C. M. (2008). Increased electrical conductivity of LiPON glasses produced by ammonolysis. *Solid State Ionics, 179*(15-16), 574-579.

Murashova, E., & Chudinova, N. (2001). Synthesis and crystal structures of lithium polyphosphates, LiPO 3, Li 4 H (PO 3) 5, and LiMn (PO 3) 3. *Crystallography Reports, 46*(6), 942-947.

Muzzio, F., Goodridge, C., Alexander, A., Arratia, P., Yang, H., Sudah, O., & Mergen, G. (2003). Sampling and characterization of pharmaceutical powders and granular blends. *International Journal of Pharmaceutics, 250*(1), 51-64.

Muzzio, F. J., Robinson, P., Wightman, C., & Brone, D. (1997). Sampling practices in powder blending. *International Journal of Pharmaceutics, 155*(2), 153-178.

Nakagawa, M. (1994). Axial segregation of granular flows in a horizontal rotating cylinder. *Chemical Engineering Science, 49*(15), 2540-2544.

Nakagawa, M., Altobelli, S., Caprihan, A., Fukushima, E., & Jeong, E.-K. (1993). Non-invasive measurements of granular flows by magnetic resonance imaging. *Experiments in fluids, 16*(1), 54-60.

Nan, C., Lu, J., Chen, C., Peng, Q., & Li, Y. (2011). Solvothermal synthesis of lithium iron phosphate nanoplates. *Journal of Materials Chemistry, 21*(27), 9994-9996.

Nguyễn, T. T., Sederman, A. J., Mantle, M. D., & Gladden, L. F. (2011). Segregation in horizontal rotating cylinders using magnetic resonance imaging. *Physical Review E, 84*(1), 011304.

Nielsen, S. F., Peters, D., & Axelsson, O. (2000). The Suzuki reaction under solvent-free conditions. *Synthetic Communications, 30*(19), 3501-3509.

Nityanand, N., Manley, B., & Henein, H. (1986). An analysis of radial segregation for different sized spherical solids in rotary cylinders. *Metallurgical transactions B, 17*(2), 247-257.

Njeng, A. S. B., Vitu, S., Clausse, M., Dirion, J.-L., & Debacq, M. (2018). Wall-to-solid heat transfer coefficient in flighted rotary kilns: experimental determination and modeling. *Experimental Thermal and Fluid Science, 91*, 197-213.

Osterheld, R., & Markowitz, M. (1956). Polymerization and depolymerization phenomena in phosphate–metaphosphate systems at higher temperatures. IV. Condensation reactions of alkali metal hydrogen phosphates. *The Journal of Physical Chemistry, 60*(7), 863-867.

Ottino, J., & Khakhar, D. (2000). Mixing and segregation of granular materials. *Annual Review of Fluid Mechanics, 32*(1), 55-91.

Ozawa, T. (1965). A new method of analyzing thermogravimetric data. *Bulletin of the chemical society of Japan, 38*(11), 1881-1886.

Pacala, S., & Socolow, R. (2004). Stabilization wedges: Solving the climate problem for the next 50 years with current technologies. *Science, 305*(5686), 968-972. doi:10.1126/science.1100103

Padhi, A. K., Nanjundaswamy, K., & Goodenough, J. (1997). Phospho-olivines as positive-electrode materials for rechargeable lithium batteries. *Journal of the electrochemical society, 144*(4), 1188-1194.

Padhi, A. K., Nanjundaswamy, K. S., & Goodenough, J. B. (1997). Phospho-olivines as positive-electrode materials for rechargeable lithium batteries. *Journal of the electrochemical society, 144*(4), 1188-1194.

Park, J.-H., Lee, K.-S., & Choi, B.-C. (2001). High-temperature transformation in KH2PO4 and RbH2PO4 crystals. *Journal of Physics: Condensed Matter, 13*(42), 9411.

Parker, D., Broadbent, C., Fowles, P., Hawkesworth, M., & McNeil, P. (1993). Positron emission particle tracking-a technique for studying flow within engineering equipment. *Nuclear Instruments and Methods in Physics Research Section A: Accelerators, Spectrometers, Detectors and Associated Equipment, 326*(3), 592-607.

Paul, E. L., Atiemo-Obeng, V. A., & Kresta, S. M. (2004). *Handbook of industrial mixing: science and practice*: John Wiley & Sons.

Pechkovskii, V. V., Shchegrov, L. N., Mel'nikova, R. Y., Shul'man, A. S., & Gusev, S. S. (1968). Use of infrared spectroscopy to study the thermal dehydration of monosubstituted phosphates of magnesium and calcium. *Vestsi Akad. Navuk Belarus. SSR, Ser. Fiz.-Tekh. Navuk*(1), 36-40.

Pelegov, D., & Pontes, J. (2018). Main Drivers of Battery Industry Changes: Electric Vehicles—A Market Overview. *Batteries, 4*(4), 65.

Peng, Y. B., & Day, D. E. (1991). High thermal expansion phosphate glasses. Part 1. *Glass Technology, 32*(5), 8.

Peray, K. E., & Waddell, J. J. (1986). *The rotary cement kiln*: Edward Arnold.

Perry, R. H., & Green, D. Perry's Chemical Engineering Handbook, 1997: McGraw-Hill.

Pillot, C. (2012). The worldwide battery market 2011-2025: Batteries.

Pollard, B., & Henein, H. (1989). Kinetics of radial segregation of different sized irregular particles in rotary cylinders. *Canadian Metallurgical Quarterly, 28*(1), 29-40.

Portillo, P. M., Vanarase, A. U., Ingram, A., Seville, J. K., Ierapetritou, M. G., & Muzzio, F. J. (2010). Investigation of the effect of impeller rotation rate, powder flow rate, and cohesion on powder flow behavior in a continuous blender using PEPT. *Chemical Engineering Science, 65*(21), 5658-5668.

Prakash, S., Tuli, G. D., Basu, S. K., & Madan, R. D. (2000). *Advanced Inorganic Chemistry, Volume 1; 17th Edition*: S. Chand & Co. Ltd.

Puri, S., & Hayakawa, H. (1999). Dynamical behaviour of rotated granular mixtures. *Physica A: Statistical Mechanics and its Applications, 270*(1-2), 115-124.

Radeke, C. A., Glasser, B. J., & Khinast, J. G. (2010). Large-scale powder mixer simulations using massively parallel GPUarchitectures. *Chemical Engineering Science, 65*(24), 6435-6442.

Rafiee, M., Simmons, M. J., Ingram, A., & Stitt, E. H. (2013). Development of positron emission particle tracking for studying laminar mixing in Kenics static mixer. *Chemical Engineering Research and Design, 91*(11), 2106-2113.

Rait J. S. (1960). GB 832011.

Rapaport, D. (2007). Radial and axial segregation of granular matter in a rotating cylinder: A simulation study. *Physical Review E, 75*(3), 031301.

Raskovalov A. A., A. O. L., Malkov V. B. (2011). Effect of LiPO3 glass crystallization. *Non-crystalline solids, 357*, 3153-3158.

Rasouli, M., Bertrand, F., & Chaouki, J. (2015). A multiple radioactive particle tracking technique to investigate particulate flows. *AIChE Journal, 61*(2), 384-394.

Rasouli, M., Dubé, O., Bertrand, F., & Chaouki, J. (2016). Investigating the dynamics of cylindrical particles in a rotating drum using multiple radioactive particle tracking. *AIChE Journal, 62*(8), 2622-2634.

Ravaine, D. (1980). Glasses as solid electrolytes. *Journal of Non-Crystalline Solids, 38*, 353-358.

Rhodes, M. J. (2008). *Introduction to particle technology*: John Wiley & Sons.

Ristow, G. H., & Nakagawa, M. (1999). Shape dynamics of interfacial front in rotating cylinders. *Physical Review E, 59*(2), 2044.

Rodríguez, B., Rantanen, T., & Bolm, C. (2006). Solvent-Free Asymmetric Organocatalysis in a Ball Mill. *Angewandte Chemie, 118*(41), 7078-7080.

Rogers, A., & Clements, J. (1972). The examination of segregation of granular materials in a tumbling mixer. *Powder Technology, 5*(3), 167-178.

Rosato, A., Prinz, F., Standburg, K., & Swendsen, R. (1986). Monte Carlo simulation of particulate matter segregation. *Powder Technology, 49*(1), 59-69.

Rosato, A., Strandburg, K. J., Prinz, F., & Swendsen, R. H. (1987). Why the Brazil nuts are on top: Size segregation of particulate matter by shaking. *Physical review letters, 58*(10), 1038.

Sadd, M. H., Tai, Q., & Shukla, A. (1993). Contact law effects on wave propagation in particulate materials using distinct element modeling. *International Journal of Non-Linear Mechanics, 28*(2), 251-265.

Santomaso, A., Olivi, M., & Canu, P. (2004). Mechanisms of mixing of granular materials in drum mixers under rolling regime. *Chemical Engineering Science, 59*(16), 3269-3280.

Sathiya S., P. G. D., Tuli S. K., Basu S. and Radan R. D. (1998).

Satyavani, T., Kumar, A. S., & Rao, P. S. (2015). Methods of synthesis and performance improvement of lithium iron phosphate for high rate Li-ion batteries: A review. *Engineering Science and Technology, an International Journal*.

Savage, S., & Lun, C. (1988). Particle size segregation in inclined chute flow of dry cohesionless granular solids. *Journal of Fluid Mechanics, 189*, 311-335.

Savage, S. B. (1983). Granular flows down rough inclines-review and extension *Studies in Applied Mechanics* (Vol. 7, pp. 261-282): Elsevier.

Scheibelhofer, O., Balak, N., Koller, D., & Khinast, J. (2013). Spatially resolved monitoring of powder mixing processes via multiple NIR-probes. *Powder Technology, 243*, 161-170.

Schneider, F., Stolle, A., Ondruschka, B., & Hopf, H. (2008). The Suzuki− Miyaura Reaction under Mechanochemical Conditions §. *Organic Process Research & Development, 13*(1), 44-48.

Schulze, D. (2007). *Powders and bulk solids: behavior, characterization, storage and flow*: Springer Science & Business Media.

Sekulic, S. S., Wakeman, J., Doherty, P., & Hailey, P. A. (1998). Automated system for the on-line monitoring of powder blending processes using near-infrared spectroscopy: Part II. Qualitative approaches to blend evaluation. *Journal of Pharmaceutical and Biomedical Analysis, 17*(8), 1285-1309.

Sherritt, R. G., Chaouki, J., Mehrotra, A. K., & Behie, L. A. (2003). Axial dispersion in the three-dimensional mixing of particles in a rotating drum reactor. *Chemical Engineering Science, 58*(2), 401-415.

Shi, F. (2004). Comparison of grinding media—Cylpebs versus balls. *Minerals Engineering, 17*(11), 1259-1268.

Shyu, L.-J. (1989). High viscosity potassium metaphosphate. *EP 0306205 A1*.

Starink, M. (2003). The determination of activation energy from linear heating rate experiments: a comparison of the accuracy of isoconversion methods. *Thermochimica Acta, 404*(1), 163-176.

Stewart, R. J. (1965). Lithium metaphosphate. *GB 1012410 A*.

Suryanarayana, C. (2001). Mechanical alloying and milling. *Progress in materials science, 46*(1-2), 1-184.

Susana, L., Canu, P., & Santomaso, A. (2011). Development and characterization of a new thief sampling device for cohesive powders. *International Journal of Pharmaceutics, 416*(1), 260-267.

Swietoslawski, M. (2014). Novel co-precipitation synthesis of $LiFePO_4$ in an anhydrous environment. *OREBA 1.0, International Conference on Olivines for Rechargeable Batteries, Book of Abstracts*, 1.

Taberlet, N., Newey, M., Richard, P., & Losert, W. (2006). On axial segregation in a tumbler: an experimental and numerical study. *Journal of Statistical Mechanics: Theory and Experiment, 2006*(07), P07013.

Talebi-Esfandarani, M., Rousselot, S., Gauthier, M., Sauriol, P., Liang, G., & Dollé, M. (2015). The Use of Reduced Cost and Purity Precursors in the Melt Preparation of LiFePO4. *Meeting Abstracts*(6), 492-492.

Talebi-Esfandarani, M., Rousselot, S., Gauthier, M., Sauriol, P., Liang, G., & Dollé, M. (2016). LiFePO4 synthesized via melt synthesis using low-cost iron precursors. *Journal of Solid State Electrochemistry, 20*(7), 1821-1829.

Tarascon, J. M., & Armand, M. (2001). Issues and challenges facing rechargeable lithium batteries. *Nature, 414*(6861), 359-367. doi:10.1038/35104644

Thilo, E., & Grunze, H. (1955). Zur Chemie der kondensierten Phosphate und Arsenate. XIII. Der Entwässerungsverlauf der Dihydrogenmonophosphate des Lić, Nać, Kć und NH. *Zeitschrift für anorganische und allgemeine Chemie, 281*(5-6), 262-283.

Thomas, N. (2000). Reverse and intermediate segregation of large beads in dry granular media. *Physical Review E, 62*(1), 961.

Thornton, C. (1997). Coefficient of restitution for collinear collisions of elastic-perfectly plastic spheres. *Journal of Applied Mechanics, 64*(2), 383-386.

Thornton, C., Cummins, S. J., & Cleary, P. W. (2013). An investigation of the comparative behaviour of alternative contact force models during inelastic collisions. *Powder Technology, 233*, 30-46.

Thornton, C., & Ning, Z. (1998). A theoretical model for the stick/bounce behaviour of adhesive, elastic-plastic spheres. *Powder Technology, 99*(2), 154-162.

Tian, M., Li, X., Shao, Z., & Shen, F. (2018). Influence of Temperature on the Performance of LiNi1/3Co1/3Mn1/3O2 Prepared by High-Temperature Ball-Milling Method. *Advances in Materials Science and Engineering, 2018*, 6. doi:10.1155/2018/6842694

Tscheng, S. H. (1978). *Convective heat transfer in a rotary kiln.* University of British Columbia.

Tsuji, Y., Tanaka, T., & Ishida, T. (1992). Lagrangian numerical simulation of plug flow of cohesionless particles in a horizontal pipe. *Powder Technology, 71*(3), 239-250.

Tyler, G. A. (1984). Lifter for rotary kiln: Google Patents.

Ufret, C., & Morris, K. (2001). Modeling of powder blending using on-line near-infrared measurements. *Drug Development and Industrial Pharmacy, 27*(7), 719-729.

Van Puyvelde, D. R. Modelling the hold up of lifters in rotary dryers. *Chemical Engineering Research and Design, 87*(2), 226-232. doi:10.1016/j.cherd.2008.08.018

Van Puyvelde, D. R. (2009). Modelling the hold up of lifters in rotary dryers. *Chemical Engineering Research and Design, 87*(2), 226-232.

Vanarase, A. U., Alcalà, M., Rozo, J. I. J., Muzzio, F. J., & Romañach, R. J. (2010). Real-time monitoring of drug concentration in a continuous powder mixing process using NIR spectroscopy. *Chemical Engineering Science, 65*(21), 5728-5733.

Vanarase, A. U., Järvinen, M., Paaso, J., & Muzzio, F. J. (2013). Development of a methodology to estimate error in the on-line measurements of blend uniformity in a continuous powder mixing process. *Powder Technology, 241*, 263-271.

Vanarase, A. U., Osorio, J. G., & Muzzio, F. J. (2013). Effects of powder flow properties and shear environment on the performance of continuous mixing of pharmaceutical powders. *Powder Technology, 246*, 63-72.

Vyazovkin, S. (2000). Computational aspects of kinetic analysis.: Part C. The ICTAC Kinetics Project—the light at the end of the tunnel? *Thermochimica Acta, 355*(1), 155-163.

Vyazovkin, S., Burnham, A. K., Criado, J. M., Pérez-Maqueda, L. A., Popescu, C., & Sbirrazzuoli, N. (2011). ICTAC Kinetics Committee recommendations for performing kinetic computations on thermal analysis data. *Thermochimica Acta, 520*(1), 1-19.

Vyazovkin, S., Chrissafis, K., Di Lorenzo, M. L., Koga, N., Pijolat, M., Roduit, B., . . . Suñol, J. J. (2014). ICTAC Kinetics Committee recommendations for collecting experimental thermal analysis data for kinetic computations. *Thermochimica Acta, 590*, 1-23.

Vyazovkin, S., & Dollimore, D. (1996). Linear and nonlinear procedures in isoconversional computations of the activation energy of nonisothermal reactions in solids. *Journal of chemical information and computer sciences, 36*(1), 42-45.

Wachters, L. H. J. a. K., H. (1964.). The calcining of sodium bicarbonate in a rotary kiln. *Proceedings of 3rd European*

Symposium Chemical Reaction Engineering, 77.

Walton, O. R. (1984). Application of molecular dynamics to macroscopic particles. *International Journal of Engineering Science, 22*(8), 1097-1107.

Walton, O. R., & Braun, R. L. (1986). Viscosity, granular-temperature, and stress calculations for shearing assemblies of inelastic, frictional disks. *Journal of Rheology (1978-present), 30*(5), 949-980.

Wang, G.-W., Dong, Y.-W., Wu, P., Yuan, T.-T., & Shen, Y.-B. (2008). Unexpected solvent-free cycloadditions of 1, 3-cyclohexanediones to 1-(pyridin-2-yl)-enones mediated by manganese (III) acetate in a ball mill. *The Journal of organic chemistry, 73*(18), 7088-7095.

Wang, L., Zhang, Z., Liang, G., Ou, X., & Xu, Y. (2012). Synthesis and electrochemical performance of Li4Ti5O12/C composite by a starch sol assisted method. *Powder technology, 215*, 79-84.

Wang, S., He, Y., Wei, H., & Xie, W. (2017). Separation Process of Fine Coals by Ultrasonic Vibration Gas-Solid Fluidized Bed. *International Journal of Analytical Chemistry, 2017*.

Wei, T. Y., Hu, Y., & Hwa, L. G. (2001). Structure and elastic properties of low-temperature sealing phosphate glasses. *Journal of Non-Crystalline Solids, 288*(1), 140-147. doi:https://doi.org/10.1016/S0022-3093(01)00612-3

Wes, G., Drinkenburg, A. A., & Stemerding, S. (1976). Heat transfer in a horizontal rotary drum reactor. *Powder Technology, 13*(2), 185-192.

Wes, G. W. J., Drinkenburg, A. A. H., & Stemerding, S. (1976). Heat transfer in a horizontal rotary drum reactor. *Powder Technol., 13*(2), 185-192. doi:10.1016/0032-5910(76)85003-6

Wightman, C., Mort, P. R., Muzzio, F. J., Riman, R. E., & Gleason, E. K. (1995). The structure of mixtures of particles generated by time-dependent flows. *Powder Technology, 84*(3), 231-240.

Wightman, C., & Muzzio, F. J. (1998a). Mixing of granular material in a drum mixer undergoing rotational and rocking motions I. Uniform particles. *Powder Technology, 98*(2), 113-124.

Wightman, C., & Muzzio, F. J. (1998b). Mixing of granular material in a drum mixer undergoing rotational and rocking motions II. Segregating particles. *Powder Technology, 98*(2), 125-134.

Wightman, C., Muzzio, F. J., & Wilder, J. (1996). A quantitative image analysis method for characterizing mixtures of granular materials. *Powder Technology, 89*(2), 165-176.

Wills, B. A. (2011). *Wills' Mineral Processing Technology: An Introduction to the Practical Aspects of Ore Treatment and Mineral Recovery*: Elsevier Science.

Workman, D. (2019). Lithium Ion Batteries Exports by Country. *http://www.worldstopexports.com/lithium-ion-batteries-exports-by-country/*.

Wunderlich, B. (1968). Crystallization during polymerization *Fortschritte der Hochpolymeren-Forschung* (pp. 568-619): Springer.

Wunderlich, B. (1990). *Thermal Analysis*. USA: Academic Press Inc.

Xu, C., Lee, J., & Teja, A. S. (2008). Continuous hydrothermal synthesis of lithium iron phosphate particles in subcritical and supercritical water. *The Journal of Supercritical Fluids, 44*(1), 92-97.

Xu, J., Qi, H., Fang, X., Lu, L., Ge, W., Wang, X., . . . Li, J. (2011). Quasi-real-time simulation of rotating drum using discrete element method with parallel GPU computing. *Particuology, 9*(4), 446-450.

Yang, S., Zavalij, P. Y., & Whittingham, M. S. (2001). Hydrothermal synthesis of lithium iron phosphate cathodes. *Electrochemistry Communications, 3*(9), 505-508.

Yang, Z., Parker, D., Fryer, P., Bakalis, S., & Fan, X. (2006). Multiple-particle tracking—an improvement for positron particle tracking. *Nuclear Instruments and Methods in Physics Research Section A: Accelerators, Spectrometers, Detectors and Associated Equipment, 564*(1), 332-338.

Yari, B., Sauriol, P., & Chaouki, J. (2019). Kinetics of the Dehydration of Lithium Dihydrogenphosphate. *The Canadian Journal of Chemical Engineering*.

Zhang, W., Wang, C., Yang, W., & Wang, C.-H. (2014). Application of electrical capacitance tomography in particulate process measurement–A review. *Advanced Powder Technology, 25*(1), 174-188.

Zik, O., Levine, D., Lipson, S., Shtrikman, S., & Stavans, J. (1994). Rotationally induced segregation of granular materials. *Physical review letters, 73*(5), 644.

Zoz, H., Reichardt, R., & Kim, J. (2002). *Application and Design of Drummills.* Paper presented at the Proceedings of the World Congress on Powder Metallurgy & Particulate Materials.

APPENDIX A THE EFFECT OF THE ROTATION RATE AND THE FLOW OF THE CARRIER GAS, ON THE TEMPERATURE OF THE CARRIER GAS AT THE EXIT POINT OF THE BAMROK

First, the evolution of the temperature of the carrier gas (N_2) with different flows at the exit point was monitored for the empty rotary kiln, after reaching steady-state condition. In a second experiment, the same procedure was performed with the rotary kiln filled to 35 % of its volume with stainless steel balls. In this case, the effect of rotation rate on the temperature of the carrier gas was also studied by varying the rotation rate in a constant carrier gas flow rate.

The experiments with empty rotary kiln were carried out to compare the results with the experiments with the stainless-steel balls and have an analogy of the effect of the balls on the heat transfer and the equilibrium temperature inside the rotary kiln. The temperature of the outer surface of the cylinder reached 450 °C in 70 min, with constant carrier gas flow rate of 5 and cylinder outer surface heating rate of 6 °C/min and kept constant afterwards. During the constant-rate heating of the outer surface, the carrier gas temperature at the exit point increased linearly and afterwards it arrived at a plateau of 380 °C in 90 min. In the following steps, five different carrier gas flows were applied in ascending and descending orders (Figure A1a). The parts of the graph in figure A1a indicated as 1 to 9 correspond to the gas flow rates of 5, 4, 3, 2, 1, 2, 3, 4, 5, respectively. From section 1 to 4, the steady-state temperature of the carrier gas at the exit point linearly depends on the negative of the carrier gas flow (Figure A2a). There is a discrepancy of 0.5–2 °C between the temperatures corresponding to the same carrier gas flow rates in ascending and descending orders because in the ascending case it takes more time to decrease the temperature to the equilibrium temperature.

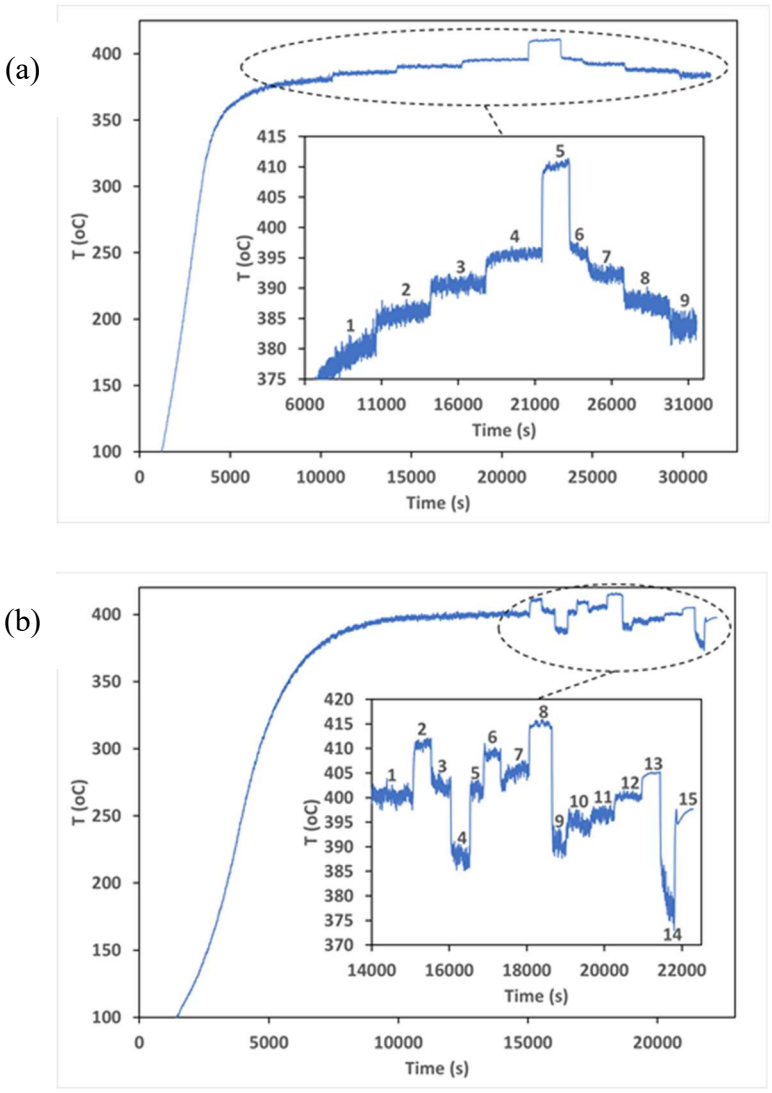

Figure A.1 Carrier gas temperature at the exit point of the rotary kiln with outer shell temperature set to 450 °C (a) empty kiln with different carrier gas flows, (b) with 400 stainless steel balls of 2.5 cm diameter (20% v/v), at different carrier gas flows and different rotation rates (Table A.1)

(a)

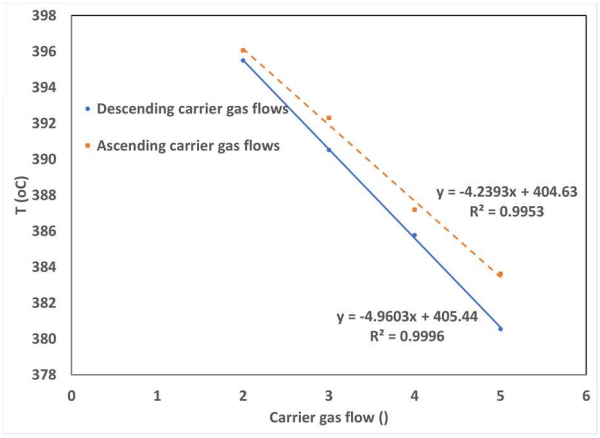

(b)

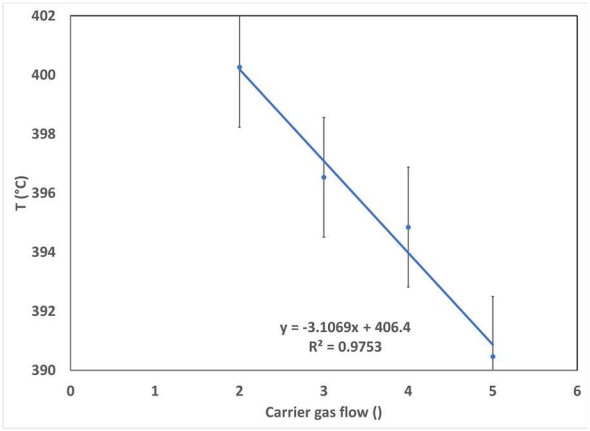

(c)

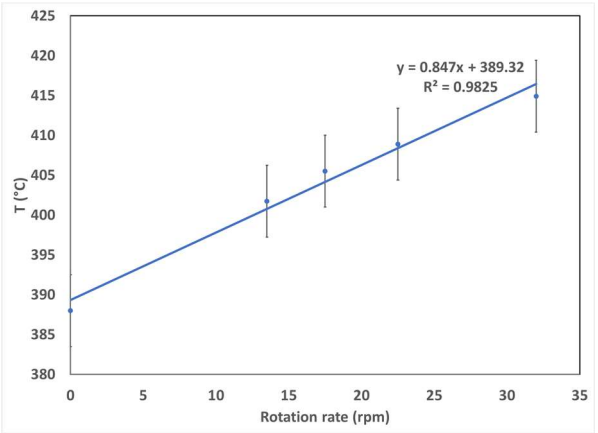

Figure A.2 Dependence of the Carrier gas temperature at the exit point of the rotary kiln on the gas flow rate and rotation rate, with outer shell temperature set to 450 °C (a) in the empty rotary kiln (b) in the rotary kiln filled with 400 stainless steel balls of 2.5 cm diameter (20% v/v) at constant rotation rate of 13 rpm and (c) in the rotary kiln filled with 400 stainless steel balls of 2.5 cm diameter (20% v/v) at constant carrier gas flow rate of 5

Table 8 Carrier gas flow and rotation rate of the rotary kiln in different zones of Figure A.1b

Zone number	Carrier gas flow (slpm)	Rotation rate (rpm)	Zone number	Carrier gas flow (slpm)	Rotation rate (rpm)	Zone number	Carrier gas flow (slpm)	Rotation rate (rpm)
1	5	13.5	6	50	22.5	11	30	0
2	3	13.5	7	50	17.5	12	20	0
3	50	13.5	8	50	32	13	10	0
4	50	0	9	50	0	14	100	0
5	50	13.5	10	40	0	15	0	0

In the case where the rotary kiln was filled with 400 stainless-steel balls of 2.5 cm diameter (20% v/v), same rotation rate, carrier gas flow rate and outer surface heating rate as the empty cylinder case, (ie. 13 rpm, 5 and 6 °C/min) were applied. The outer surface reached 450 °C in 70 min and kept constant afterwards. However, it took longer time (100 min) for the temperature of the carrier gas at the exit point to nonlinearly reach a steady-state temperature of 400 °C that was 20 °C more than the empty-kiln case. At this steady-state, the carrier gas flow rate and the rotation rate were varied independently to evaluate their effect on the gas temperature at the exit point (Table A.1). The parts of the graph in figure A1b indicated as 4 to 8 correspond to the experiment where we studied the effect of the rotation rate on the carrier gas temperature at the exit point with constant flow rate. Plotting the temperatures versus rotation rate in figure A2b shows a linear dependence of the carrier gas temperature at the exit point on the rotation rate that is because of a higher total heat transfer coefficient due to better contact between the gas and the stainless-steel balls. By better contact, we mean balls with higher surface temperature are more frequently exposed to the gas on the active layer of the tumbling bed of the balls.

The parts in figure A1b indicated as 9 to 12 correspond to the experiment where we studied the effect of carrier gas flow rate (in descending order) on its temperature at exit point in the rotary kiln filled with 400 stainless-steel balls of 2.5 cm diameter (20% v/v), without rotating the kiln. Here we measured higher steady-state temperatures (by 5–10 °C) of the carrier gas at exit point than the empty kiln case in equivalent gas flow rates, although the residence time of the gas was decreased because of 30% volume decrease that was occupied by the balls. Figure A2c shows the linear interpolation of the data in four flow rates which in comparison with the empty kiln case, the absolute value of the slope is less, meaning the carrier gas temperature is less sensitive to the flow rate because of shorter residence time.